

DISSERTATION

Improving our Understanding of the Atmospheric Weak-wind Boundary Layer using Spatially Explicit Observations near the Ground Surface

Author:

Lena PFISTER

born in Aschaffenburg

Supervisor:

Prof. Dr. Christoph K. THOMAS

*A thesis submitted in fulfillment of the requirements
for the degree of*

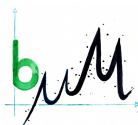
Dr. rer. nat.

from the

UNIVERSITY OF BAYREUTH

Faculty of Biology, Chemistry, and Earth Sciences

Micrometeorology



UNIVERSITÄT
BAYREUTH

Bayreuth, 2020

This doctoral thesis was prepared at the department of Micrometeorology at the University of Bayreuth from 03/2016 until 09/2020 and was supervised by Prof. Dr. Christoph K. Thomas.

This is a full reprint of the thesis submitted to obtain the academic degree of Doctor of Natural Sciences (Dr. rer. nat.) and approved by the Faculty of Biology, Chemistry and Geosciences of the University of Bayreuth.

Date of submission: 05.10.2020

Date of defence: 21.12.2020

Acting dean: Prof. Dr. Matthias Breuning

Doctoral committee:

Prof. Dr. Christoph K. Thomas (reviewer)
Prof. Dr. Ivana Stiperski (reviewer)
Prof. Dr. Stefan Peiffer (chairman)
Prof. Dr. Cyrus Samimi

Improving our Understanding of the Atmospheric Weak-wind Boundary Layer using Spatially Explicit Observations near the Ground Surface

Lena PFISTER

Supervised by
Prof. Dr. Christoph K. THOMAS

This doctoral thesis was done within the DarkMix project of Prof. Dr. Christoph Thomas (Micrometeorology) which received funding from the European Research Council (ERC) under the European Union's Horizon 2020 research and innovation programme under grant agreement No 724629.

For this doctoral thesis the data set from the Shallow Cold Pool experiment was analyzed which received support from awards AGS-1115011, AGS-1614345, and AGS-0955444 by the National Science Foundation and contracts W911NF-10-1-0361 and W911NF-09-1-0271 by the Army Research Office, and the Earth Observing Laboratory of the National Center for Atmospheric Research which collected the sonic anemometer measurements.

Contents

List of Publications	vii
Conferences and Workshops	ix
Acknowledgements	xi
Summary	xiii
Zusammenfassung	xv
1 Introduction	1
1.1 The atmospheric weak-wind boundary layer	1
1.2 Spatially explicit observations	2
1.3 Classification of the boundary layer into regimes	3
1.4 Impact of submeso-scale motions on the boundary layer	4
1.5 Objectives of the doctoral thesis	5
2 Methods and Field site of the Shallow Cold Pool Experiment	7
3 Main Results	11
3.1 Classifying the Nocturnal Boundary Layer into Temperature and Flow regimes	11
3.1.1 Night classification scheme	11
3.1.2 Derived night classes	12
3.2 Small-Scale Variability in the Nocturnal Boundary Layer	14
3.3 Thermal Submeso-Fronts	17
3.3.1 Detection and Analysis of Thermal Submeso-Fronts	17
3.3.2 Horizontal and vertical structure of Thermal Submeso-Fronts	19
3.3.3 TSFs forcings and implications for the boundary layer	21
3.3.4 Recommendations and Thoughts for further Studies	24
4 Conclusion	25
References	35
Individual Contributions to the joint Publications	37
A Classifying the Nocturnal Boundary Layer	39
B Small-Scale Variability in the Nocturnal Boundary Layer	61
C Thermal Submeso-Front - Part 1: Detection & Mean Statistics	81
D Thermal Submeso-Front - Part 2: Generating Mechanisms & Implications	99
Eidesstattliche Erklärung	125

List of Publications

This is the list of all my publications. Not all were used for this dissertation as they were based on my master thesis or my contribution was rather minor. A detailed description of the individual contributions to the joint publications can be found on page 37.

^{DT}publication for dissertation

*corresponding author(s)

in preparation Zeller M.*, Huss J.*, **Pfister L.**, Schulz A., Thomas, C.K., NYTEFOX - Ny-Ålesund Turbulence Fiber Optic Experiment, Svalbard, Norway, *Earth System Science Data*

^{DT}under review **Pfister L.***, Lapo K., Mahrt L., Thomas, C.K., Thermal submeso-scale motions in the nocturnal stable boundary layer - Part 2: Generating mechanisms & implications, *Boundary-Layer Meteorology*

^{DT}provisionally accepted **Pfister L.***, Lapo K., Mahrt L., Thomas, C.K., Thermal submeso-scale motions in the nocturnal stable boundary layer - Part 1: Detection & mean statistics, *Boundary-Layer Meteorology*

2020 Lapo, K.*, Freundorfer, A., **Pfister, L.**, Schneider, J., Selker, J., Thomas, C., Distributed observations of wind direction using microstructures attached to actively heated fiber-optic cables, *Atmospheric Measurement Techniques*, DOI: 10.5194/amt-13-1563-2020

^{DT}2020 Mahrt L.*, **Pfister L.**, Thomas C.K., Small-Scale Variability in the Nocturnal Boundary Layer, *Boundary-Layer Meteorology*, DOI: 10.1007/s10546-019-00476-x

^{DT}2019 **Pfister L.***, Lapo K., Sayde C., Selker J., Mahrt L. and Thomas C.K., Classifying the Nocturnal Atmospheric Boundary Layer into Temperature and Flow Regimes, *Quarterly Journal of the Royal Meteorological Society*, DOI: 10.1002/qj.3508

2017 **Pfister L.***, Sigmund A., Olesch J. and Thomas C.K., Nocturnal Near-Surface Temperature, but not Flow Dynamics, can be Predicted by Microtopography in a Mid-Range Mountain Valley, *Boundary-Layer Meteorology*, DOI: 10.1007/s10546-017-0281-y

2017 Sigmund A.*, **Pfister L.**, Sayde C. and Thomas C.K., Quantitative analysis of the radiation error for aerial coiled-fiber-optic distributed temperature sensing deployments using reinforcing fabric as support structure, *Atmospheric Measurement Techniques*, DOI: 10.5194/amt-10-2149-2017

Conferences and Workshops

- 12/2019 **Pfister L.**, Lapo E. K., Mahrt L., Thomas C.K., Gentle topography induces thermal submeso-scale motions within the stable boundary layer, *American Geophysical Union Fall Meeting 2020*, San Francisco, CA, USA, [AGU2020-A13N-3145](#). (Poster)
- 04/2019 **Pfister L.**, Mahrt L., Lapo K., Sayde C. and Thomas C.K., Investigating thermal micro-fronts near the surface in the nocturnal boundary layer over gentle terrain through spatially explicit observations from fiber-optic distributed sensing, *European Geosciences Union General Assembly 2019*, Vienna, Austria, [EGU2019-10171](#). (Presentation)
- 04/2018 **Pfister L.**, Sayde C., Selker J., Mahrt L. and Thomas C.K., A classification scheme for nocturnal atmospheric boundary layers, *European Geosciences Union General Assembly 2018*, Vienna, Austria, [EGU2018-9113](#). (Presentation)
- 10/2017 **Pfister L.**, Mahrt L., Selker J. and Thomas C.K., Formation of Thermal Micro-fronts in Gentle Terrain, *BayCEER Workshop 2017*, Bayreuth, Germany. (Poster)
- 03/2017 **Pfister L.**, Mahrt L. and Thomas C.K., Classifying nocturnal Boundary Layer Regimes, *3rd Decennial Workshop "Turbulence in Stably Stratified Planetary Boundary Layers"*, Delft, Netherlands. (Poster)
2. Award: Outstanding Student Poster
- 04/2016 **Pfister L.**, Sigmund A., Olesch J. and Thomas C.K., Novel insights into the dynamics of cold-air drainage and pooling on a gentle slope from fiber-optic distributed temperature sensing, *European Geosciences Union General Assembly 2016*, Vienna, Austria, [EGU2016-4984](#). (Presentation)

Acknowledgements

I thank all people who supported me and contributed to this thesis in some way. Personal thanks go to

- my supervisor Prof. Dr. Christoph Thomas for offering me this thesis. Through his help I was able to gain more knowledge about the atmospheric boundary layer and learned a new measurement technique. This technique is not only challenging in applying, it is also opening new insights into the boundary layer through specific analysis which I learned with his help. He guided me nicely through the progress of my dissertation. I also want to thank him for giving me so many opportunities to grow as a scientist, to network and to present myself in many national and international workshops and conferences. I could build my own network and feel like I found a place in the atmospheric boundary layer community through his help.
- Prof. Dr. John Selker and Prof. Dr. Chadi Sayde to host me in 2016 and to introduce me to the data set of my dissertation.
- Prof. Dr. Larry Mahrt for so many nice discussions during lunch breaks when I was in the USA and within emails. He shared his time and contributed to all my publications.
- in common to all my co-authors for their important contributions to the manuscripts which are part of the thesis. Their helpful comments and contributions were essential for the successful completion of the manuscripts.
- my colleagues at the Department of Micrometeorology, University of Bayreuth, Anita Freundorfer, Karl Lapo, and Wolfgang Babel. I appreciated your thoughts during discussions as well as your support. Thank you, Anita, for being a good office roomie, having a sympathetic ear for me, sharing great new publications, and giving me your thoughts on my plots. Thank you, Karl, for providing a lot of coffee, great discussions on my plots, and helping me in training writing. Thank you Wolfgang, for your help in teaching and keeping R alive. I also want to mention Johannes Olesch, Johann Schneider and Barbara Jakob. Thank you for giving me the help I needed every time I approached you.
- Christian, Eva, and Andi, and all my Baybees for mental support during the last years.
- my parents for always supporting me.

Summary

Within the atmospheric boundary layer energy and matter are most effectively exchanged with the earth's surface by turbulence. Turbulence is the irregular almost random fluctuation in velocity, temperature, and scalars. Research accordingly focuses on turbulent exchange processes. While those processes are mostly understood during the day, we need to improve our understanding of the nocturnal boundary layer especially during calm winds. Correspondingly, this doctoral thesis investigated turbulence within the nocturnal boundary layer using spatially explicit observations near the ground surface. The observations were taken during the Shallow Cold Pool experiment (SCP) in Colorado, USA, in 2012. The data set had a unique combination of different techniques also featuring fiber-optic distributed sensing (FODS) with spatial continuous measurements. The gentle terrain of the field site was chosen as it commonly is assumed to have a rather small impact on the nocturnal boundary layer and represents most of the earth's surface.

For investigating turbulence, we developed a nighttime classification scheme based on a surface energy balance which determined static stability, wind regime, and longwave radiative forcing as the three forcing parameter. Not only each forcing parameter had a specific impact on turbulence but also the three selected night classes determined by the combination of them, hence, they were further investigated. The first night class represented conditions with strong dynamic forcing elevating near-surface temperature by topographically induced mixing at the North shoulder of the valley. The second night class was a concurrence of topographically induced mixing and cold air at the bottom of the valley due to strong radiative cooling. The third night class was characteristic of weak winds eroding the impact of mechanical mixing but enhancing the impact of cold air within the valley. Consequently, the proposed classification scheme is successful in sorting the experimental data into physically meaningful temperature and flow regimes representing turbulence within the boundary layer.

The classification scheme, however, was not successful in detecting submeso-scales motions which also impact turbulence within the weak-wind boundary layer significantly. A follow up study showed that at three different field site including SCP the variability of temperature is significantly increased during the submeso scale and usually is larger than the nocturnal temperature trend. Accordingly, a case study of the SCP data featuring a submeso-scale motion was investigated in detail. During weak winds a transient cold-air pool developed within the valley which was displaced uphill towards the North shoulder by a South-Westerly flow. At the North shoulder temperatures were usually elevated due to turbulent mixing. Consequently, the two air masses created a sharp boundary which we refer to as thermal submeso-front (TSF) in the following studies. We anticipate that these interactions are globally common. Further investigations are necessary to fully understand the relation between temperature variability, wind speed and direction, the topography, and TSFs.

Correspondingly, for the last two studies a detection algorithm was developed which accurately determined the TSF location. This was the first study being able to continuously track a submeso-scale motion. TSFs were frequently occurring within the

nocturnal boundary emphasizing their relevance. TSFs consist of two layers which push against each other forcing the TSF up and down the valley side wall in a wave like motion. The warm-air layer is mechanically generated by topographically induced mixing at the plateau-edge, while the cold-air layer is thermo-dynamically driven by topographically induced cold-air drainage. TSFs vanish during strong wind speed and spatially homogeneous wind direction which most likely erodes any cold air. The key to these insights was FODS as we could conditionally average parameters depending on the occurrence and location of TSFs. TSFs impact the boundary layer significantly. During TSFs ergodicity assumptions are invalid as their advective velocity is an order of magnitude lower than the mean wind speed. The mean difference of the sensible heat flux between the air layers of TSFs is 30 Wm^{-2} , hence, the impact on turbulence is strong. At the valley bottom the air layers of TSFs are stacked which increases static stability beyond the capability of radiative forcing. Here, the decoupled cold-air layer also invalidates flux-gradient similarity theory. Unfortunately, no distinct forcing for TSFs nor a relation to a wind or thermal regime could be determined.

FODS outperformed point observations as even the dense network of the SCP experiment missed TSFs most of the time. So far many submeso scale motions are detected, but their relation, interaction, and needed forcing is not well understood. We need to change from classification schemes using vertical forcing mechanism and focus on the relation between motions on multiple scales. Further, classification schemes and modeling studies need to incorporate the impacts of topography as well as horizontal advection to improve our understanding of the nocturnal boundary layer.

Zusammenfassung

Innerhalb der atmosphärischen Grenzschicht werden Energie und Materie mit der Erdoberfläche am effektivsten durch Turbulenzen ausgetauscht. Turbulenz ist die unregelmäßige, fast zufällige Fluktuation von Geschwindigkeit, Temperatur und Skalaren. Die Forschung konzentriert sich dementsprechend auf turbulente Austauschprozesse. Während diese Prozesse während des Tages gut verstanden sind, müssen wir unser Verständnis der nächtlichen Grenzschicht vor allem bei schwachen Winden verbessern. Dementsprechend untersuchte diese Doktorarbeit die Turbulenz innerhalb der nächtlichen Grenzschicht anhand räumlich expliziter Beobachtungen nahe der Bodenoberfläche. Die Beobachtungen wurden während des Shallow Cold Pool Experiments (SCP) in Colorado, USA, im Jahr 2012 gemacht. Der Datensatz wies eine einzigartige Kombination verschiedener Techniken auf, die auch räumlich kontinuierliche Messungen mittels der Glasfasertechnik (fiber-optic distributed sensing - FODS) beinhaltete. Das sanfte Gelände des Feldstandortes wurde gewählt, da allgemein davon ausgegangen wird, dass es einen eher geringen Einfluss auf die nächtliche Grenzschicht hat und den größten Teil der Erdoberfläche darstellt.

Für die Untersuchung von Turbulenzen entwickelten wir ein nächtliches Klassifikationsschema auf der Grundlage einer Oberflächenenergiebilanz, die die statische Stabilität, das Windregime und den langwelligen Strahlungsantrieb als die drei Antriebsparameter bestimmte. Nicht nur jeder Antriebsparameter hatte einen spezifischen Einfluss auf die Turbulenz, sondern auch die drei ausgewählten Nachtklassen, die durch die Kombination dieser Parameter bestimmt wurden. Entsprechend wurden die Nachtklassen weiter untersucht. Die erste Nachtklasse repräsentierte Bedingungen mit starkem dynamischem Antrieb, der die oberflächennahe Temperatur durch topographisch induzierte Vermischung an der Nordschulter des Tals erhöhte. Die zweite Nachtklasse war ein Zusammentreffen von topographisch induzierter Durchmischung und kalter Luft am Talboden aufgrund starker Strahlungskühlung. Die dritte Nachtklasse war charakteristisch für schwache Winde, die den Einfluss der mechanischen Durchmischung untergruben, aber den Einfluss der kalten Luft innerhalb des Tals verstärkten. Folglich ist das vorgeschlagene Klassifikationsschema erfolgreich bei der Sortierung der experimentellen Daten in physikalisch aussagekräftige Temperatur- und Strömungsregime, die charakteristisch für Turbulenzen innerhalb der Grenzschicht sind.

Das Klassifizierungsschema war jedoch nicht erfolgreich bei der Erkennung von submeso-skaligen Bewegungen, die sich ebenfalls signifikant auf die Turbulenz gerade innerhalb der Schwachwindgrenzschicht auswirken. Eine Folgestudie zeigte, dass an drei verschiedenen Feldstandorten, einschließlich SCP, die Variabilität der Temperatur während der Submeso-Skala signifikant erhöht ist und gewöhnlich größer ist als der nächtliche Temperaturtrend. Dementsprechend wurde eine Fallstudie der SCP Daten mit einer submeso-skaligen Strömungen im Detail untersucht. Bei schwachen Winden entwickelte sich innerhalb des Tals ein transienter Kaltluftsee, der durch eine südwestliche Strömung bergauf zur Nordschulter hin verschoben wurde. An der Nordschulter waren die Temperaturen aufgrund der turbulenten Durchmischung meist erhöht. Dementsprechend schufen die beiden Luftmassen

eine scharfe Grenze, die wir in der folgenden Studie als thermische Submesofront (TSF) bezeichnen. Wir gehen davon aus, dass diese Wechselwirkungen allgemein in seichtem Gelände üblich sind. Weitere Untersuchungen sind notwendig, um die Beziehung zwischen Temperaturvariabilität, Windgeschwindigkeit und -richtung, der Topographie und den TSFs vollständig zu verstehen.

Dementsprechend wurde für die letzten beiden Studien ein Detektionsalgorithmus entwickelt, der die TSF-Lage genau bestimmt. Dies war die erste Studie, die in der Lage war, eine submeso-skalige Strömung kontinuierlich zu verfolgen. TSFs traten häufig innerhalb der nächtlichen Grenzschicht auf, was ihre Relevanz unterstreicht. TSFs bestehen aus zwei Schichten, die gegeneinanderdrücken und die TSF in einer wellenartigen Bewegung an der Talseitenwand auf und ab zwingen. Die Warmluftschicht wird mechanisch durch topographisch induzierte Durchmischung an der Plateaukante erzeugt, während die Kaltluftschicht thermodynamisch durch topographisch induzierte Kaltluftabfluss angetrieben wird. TSFs verschwinden bei starker Windgeschwindigkeit und räumlich homogener Windrichtung, was höchstwahrscheinlich zur Erosion der Kaltluft führt. Der Schlüssel zu diesen Erkenntnissen war FODS, da wir die Parameter in Abhängigkeit vom Vorkommen und der Lage von TSF mitteln und analysieren konnten. TSFs beeinflussen die atmosphärische Grenzschicht signifikant. Ergodizitätsannahmen sind während TSFs ungültig, da ihre advective Geschwindigkeit eine Größenordnung niedriger ist als die mittlere Windgeschwindigkeit. Die mittlere Differenz des fühlbaren Wärmestroms zwischen den Luftschichten von TSFs beträgt 30 W m^{-2} , daher ist der Einfluss auf die Turbulenz stark. In der Talsohle sind die Luftschichten von TSFs gestapelt, was die statische Stabilität über die Fähigkeit des Strahlungsantriebs hinaus erhöht. Hier entkräftet die entkoppelte Kaltluftschicht auch die Flussgradienten-Ähnlichkeitstheorie. Leider konnte weder ein eindeutiger Antriebsparameter für TSFs noch eine Beziehung zu einem Wind- oder thermischen Regime festgestellt werden.

FODS übertraf die Punktbeobachtungen, da selbst das dichte Netzwerk des SCP-Experiments die TSFs die meiste Zeit nicht erkannte. Bisher sind viele submeso-skalige Strukturen entdeckt, aber ihre Beziehung, Wechselwirkung und der erforderliche Antrieb sind noch nicht gut verstanden. Wir müssen uns von Klassifizierungsschemata mittels vertikaler Antriebsmechanismen lösen und uns auf die Beziehung zwischen Bewegungen auf mehreren Skalen konzentrieren. Darüber hinaus müssen Klassifikationsschemata und Modellierungsstudien die Auswirkungen der Topographie sowie horizontale Advektion berücksichtigen, um unser Verständnis der nächtlichen Grenzschicht zu verbessern.

1 Introduction

1.1 The atmospheric weak-wind boundary layer

The atmospheric boundary layer (ABL) is the layer of the atmosphere which is in contact and influenced by the earth's surface. Within the ABL the most important exchange processes of energy and matter take place leading to for example fog formation (Müller et al., 2010; Izett et al., 2018) or the urban heat island (Oke, 1982; Kuttler et al., 1996; Luo and Asproudi, 2015) which directly impact human life. Exchange processes most effectively take place due to turbulence and corresponding mixing which is omnipresent in the ABL. Turbulence is among other things responsible for efficiently dispersing the pollutants that accompany modern life (Wallace and Hobbs, 2006). Consequently, one main subject of research is turbulence within the ABL. Historically, turbulence is commonly investigated in time and vertically by tower measurements (Baas et al., 2009; Mortarini et al., 2017; Acevedo et al., 2019), but the number of spatial investigation of turbulence is increasing with new measurement techniques (Thomas et al., 2012; Sayde et al., 2015; Grudzielanek and Cermak, 2018).

During the day the main driver for turbulence is radiation and the wind speed shear and their relation is well understood (Kaimal et al., 1976; Caughey and Palmer, 1979; Lenschow and Stankov, 1986) and is successfully implemented in models (Holtslag et al., 1995; Siebesma et al., 2007). During the night on the other hand, when inversions and the stable boundary layer (SBL) build up, the relation between turbulence, radiation, and wind speed is not fully understood yet. Usually turbulence decreases with decreasing wind speed (Sun et al., 2012) due to decreasing wind speed shear and with increasing inversion strength (Mahrt et al., 2013) which restricts vertical exchange and thus turbulence. Accordingly, for the SBL the buoyant suppression of turbulence and shear generation of turbulence is important. The ratio of the buoyancy term to the shear term is the dimensionless Richardson number, Ri (definition of gradient Ri in Sect. 2), representing the dynamic stability of the boundary layer. In literature, for the flux Ri a threshold of 0.25 is used to differentiate between the dynamically unstable and turbulent boundary layer for values below this threshold, and the dynamically stable boundary layer with a flow reaching a laminar state for values above this threshold. The exact value of the critical flux Richardson number is still under discussion (Galperin et al., 2007; Freire et al., 2019). Nevertheless, especially for the flux $Ri \gg 0.25$ the buoyancy can be so strong that the boundary layer next to the surface detaches from the layers above leading to further cooling which is called decoupling. The in theory established decoupling, however, leads to so-called runaway cooling in models as the inversion within the decoupled layer grows irrespective of above wind speeds (Louis, 1979; Derbyshire, 1999; Steeneveld et al., 2006; Basu et al., 2008; Lapo et al., 2019). But observations show that even within the decoupled layer and corresponding weak winds turbulence is sustained. As Ri is only taking vertical exchange processes into account, the horizontal generation as well as transport of turbulence is not taken into account (Freire et al., 2019) which highlights the necessity to incorporate horizontal transport processes in theory and models. So far neither experiments nor models could explain this ABL behavior completely which remains a longstanding challenge for experimentalists

and modelers (Holtslag et al., 2013).

Further investigations on motions at different temporal and spatial scales is necessary to better understand turbulence within SBLs. So far many motions could be detected within the SBL impacting exchange processes as well as turbulence like cold-air pools (Banta et al., 1997; Clements et al., 2003; Goulden et al., 2006; Bodine et al., 2009; Lareau et al., 2013; Mahrt et al., 2013), submeso-scale motions (Mahrt, 2009; Thomas, 2011; Acevedo et al., 2014; Cava et al., 2019a; Vercauteren et al., 2019; Mahrt, 2020), microfronts (Mahrt, 2019), gravity waves (Hoover et al., 2015; Sun et al., 2015), or meandering (Anfossi et al., 2005; Mahrt, 2007; Mortarini et al., 2016; Stefanello et al., 2020). Most of these represent submeso-scale motions which seem to have a big impact on the turbulence structure of the SBL. Nevertheless, even though detected, their relation to and interaction with each other is not fully understood yet. Consequently, the efforts of my doctoral thesis focused on investigating turbulence within the weak-wind boundary layer in space and time with spatially explicit observations to better understand different turbulent structures and the impact of submeso-scale motions.

1.2 Spatially explicit observations

For investigating the weak-wind boundary layer in detail a measurement technique needs to be used which offers high spatial resolution of temperature measurements like the fibre-optic distributed sensing (FODS) technique. Every few centimetre along a fibre-optic cable spatially-distributed air temperature and wind speed can be measured up to a frequency of 1 Hz. For wind speed measurement the fiber-optic cable needs to be actively heated to function like a hotwire anemometer (Sayde et al., 2015). FODS can be applied in the atmospheric boundary layer (Keller et al., 2011; Thomas et al., 2012; Sigmund et al., 2017) leading to unique results like the tomography of a cold-air current (Zeeman et al., 2015), the determination of flow regimes (Pfister et al., 2017), and testing the validity of Taylor’s hypothesis in the atmospheric surface layer (Cheng et al., 2017). Due to the spatial continuous measurements we argue that FODS is capable of detecting submeso-scale motions, however, it does not provide flux measurements like ultrasonic anemometer stations. In order to overcome this, the two measurements techniques were combined (cf. Section 3.3.1)

The data set used for my doctoral thesis was the Shallow Cold Pool experiment (SCP) which was conducted within gentle terrain in the Colorado plains, CO, USA in 2012 (Sect. 2). This experiment not only featured a transect with FODS, but also an extensive sensor network with 19 ultrasonic anemometer station at 1 m above ground level distributed within a valley featuring gentle terrain (cf. Fig. 1), a 20-m tower with ultrasonic anemometer and hygrothermometers at 8 levels, and a wind profiler. This network by itself already led to new insights into stably stratified flow (Mahrt et al., 2014b; Mahrt, 2017c), the structure of the nocturnal boundary layer (Geiss and Mahrt, 2015; Mahrt and Heald, 2015; Mahrt, 2017b), and the response of the boundary layer to shear (Mahrt et al., 2014a; Mahrt, 2017a). Further, the relation between horizontal wind speed, turbulence characteristics, and stratification was investigated in detail (Mahrt and Thomas, 2016). In some of these publications transient modes or microfronts are mentioned which cause intermittently increased turbulence during cold-air drainage and pooling. Accordingly, this raises further questions on how those are formed and how they interact with the stable boundary layer. This is to some extent investigated in Mahrt (2017b), however, could yet not

be answered completely. We argue that this is possible when using FODS in combination with the network.

Another novelty is the investigation of the spatial variability of the bulk Richardson number, Ri_b , by analysing the FODS transect with three levels of spatial continuous measurements of the wind speed and temperature. This is especially interesting for modelling studies which commonly use a spatially homogeneous Ri_b to parameterize turbulence near the surface (Lapo et al., 2019). Besides, Ri_b is used in stability functions for deriving the sensible heat flux (Brotzge and Crawford, 2000), hence, we investigated Ri_b during different temperature and flow regimes (Sect. 3.1) as well as the relation between Ri_b and the sensible heat flux, Q_H (Sect. 3.3).

1.3 Classification of the boundary layer into regimes

Commonly the boundary layer is classified into different regimes which represent a specific characteristic which changes the boundary layer behavior or represent conditions for which different boundary layer concepts need to be applied. Several approaches for defining regimes have been proposed using local or internal boundary-layer parameters. Holtslag and Nieuwstadt (1986) proposed different scaling regimes for the SBL assuming the validity of the Monin-Obukhov similarity theory. Each scaling regime is determined by z/h and h/L with h being the mixing height, L the Obukhov length, z the reference height. However, the definition of a mixing height during very stable conditions is controversial and ambiguous as increasing stability limits vertical fluxes and eddies may become disconnected from the surface (e.g. Derbyshire 1999, Sun et al. 2012).

The most commonly used concept to determine physically meaningful boundary layer regimes was developed by Mahrt (1998). The boundary layer is also defined by the local parameter z/L , but regimes are determined by the relation between z/L and the sensible heat flux, classifying the atmosphere into a weakly stable boundary layer (wSBL), a transition regime, and the very stable boundary (vSBL). However, z/L is site dependent, hence, no universal threshold value can be given. Further, z/L is a local stability parameter and thus does not contain information about the global state of the larger-scale boundary layer. Especially in the stable boundary layer, a single non-dimensional combination, such as z/L or also the bulk Richardson number Ri_b , is insufficient to determine boundary layer regimes. For example, during cold-air drainage surface-layer similarity theory is violated, invalidating the use of z/L and Ri_b (e.g. Mahrt et al. 2014a, Mahrt et al. 2014b, Mahrt and Heald 2015, Mahrt 2017c).

One more recent and also commonly used classification are wind regimes which separate the boundary layer into the weak-wind and strong-wind regime by an objectively determined threshold (Sun et al., 2012, 2016). As assumptions necessary for similarity theory are violated during the vSBL and during the weak-wind regime, the weak-wind regime and vSBL became synonyms for classifications as also shown in the conceptual diagram of Sun et al. (2020). However, this is actually only true under the assumption of homogeneous terrain, no influence of synoptic flow, and absence of advection.

Besides stability and wind regimes, other studies such as Edwards (2009) reveal the importance of radiative forcings for the boundary layer, hence, we argue that radiative forcing should be incorporated in a classification scheme. For example, the turbulent temperature scale is related to cloud cover (Holtslag and De Bruin, 1988),

and cloud cover in concert with the geostrophic wind speed impacts the boundary layer (Monahan et al., 2015). Radiative forcing is also important for wind regimes as wind speed threshold changes depending on radiative forcing (Sun et al., 2020) and stability (Mahrt and Heald, 2015) which is also influenced by radiative forcing.

To separate a decoupled from a coupled SBL, Acevedo et al. (2016) determined a threshold wind speed at which the average vertical gradient of the turbulent kinetic energy switches sign at all observational levels. For wind speeds higher than this threshold a coupled SBL is expected. Accordingly, the threshold wind speed of Sun et al. (2012) determines locally if the eddies communicate with the surface, while the threshold wind speed of Acevedo et al. (2016) is an indication for the vertical communication of exchange across the entire surface layer. However, the method of Acevedo et al. (2016) requires turbulence observations at multiple levels to capture the complete surface layer, which are not available for most field campaigns.

Others have attempted to use parameters external to the boundary layer, i.e. those not affected by the surface, to determine boundary layer regimes. Van de Wiel et al. (2012) proposed using a minimum geostrophic wind speed needed to sustain near-surface turbulence. In their study, geostrophic wind speed was determined by surface pressure observations from eight synoptic stations in a radius of 75 km around a tower. Similarly, van Hooijdonk et al. (2015) used the wSBL and vSBL concept and showed that both regimes are well characterized by the so-called shear capacity defined as the critical wind speed necessary to sustain enough turbulence to balance the radiative cooling. van der Linden et al. (2017) refined this approach and proposed using bin averages of the ambient geostrophic wind determined by horizontal pressure gradients. For their observations ensemble-averages of the net radiation, friction velocity and turbulent heat flux organized surprisingly well when binned by this approach. This scheme was also used by Baas et al. (2018) leading to good model results when modeling the stable boundary layer. However, measurements of the geostrophic wind speed are not easily obtained for most campaigns and the communication of eddies across the tower layer remains difficult to determine.

Consequently, we want to develop a simple, but effective and generally applicable night classification scheme based upon the three forcing variables static stability, wind regime, and longwave radiative forcing.

1.4 Impact of submeso-scale motions on the boundary layer

Even though most of the above mentioned classifications are stratifying the nocturnal boundary layer into different regimes with a specific relation between stability and turbulence, none of them were commonly applicable without specific assumptions or required not commonly used measurements like the geostrophic wind speed. The study of Monahan et al. (2015) even states that traditional stability parameters alone are inadequate for partitioning the SBL.

The variability of turbulence within the SBL is not fully understood and it remains uncertain if the variability of turbulence can be defined by forcings. However, turbulence is also significantly altered by motions within the boundary layer like submeso-scale motions (Acevedo et al., 2014; Cava et al., 2019b; Mortarini et al., 2017), meandering (Lang et al., 2018; Mortarini et al., 2016, 2019), and internal gravity waves (Sun et al., 2015). These motions also change the local flow (e.g., Monti et al. (2002); Sun et al. (2015); Vercauteren et al. (2016); Cava et al. (2019a)). Besides, intermittent bursts of turbulence were observed within the SBL (Nappo, 1991). This so-called

intermittent turbulence is also in the focus of research as it significantly impacts the nocturnal boundary, but the mechanisms or motions creating it are not clear yet. So far studies mostly connected intermittent turbulence to entrainment of larger scale flows or gravity waves into the SBL (Sun et al., 2012, 2016), but even observations like done by Cava et al. (2019a,b) could not clarify the origin of intermittent turbulence. At the same time turbulence is usually very weak during the occurrence of cold air masses (Zeeman et al., 2015; Kang et al., 2015; Mahrt and Heald, 2015; Grudzielanek and Cermak, 2018).

Further, within the nocturnal boundary layer the above mentioned motions on different scales also interact with and modulate each other, hence, turbulence is not only connected to specific motions, but also to their interaction (Mortarini et al., 2017). Similar results are presented by Cava et al. (2019b) showing that a low-level jet forms after the collapse of turbulence, but then generates mixing below the wind maximum. Also the topography plays an important role for the formation of such motions as even the modest topography influences the process of formation for example for cold-air drainage and pooling (Pfister et al., 2017; Mahrt, 2017c).

Correspondingly, we argue that the investigation of such motions, air masses, and their relation offers an alternative to understand turbulence within the nocturnal boundary layer.

1.5 Objectives of the doctoral thesis

Objective 1: The influence of different forcings on the boundary layer especially in context of near-surface turbulence and stability has been investigated by many studies (Sect. 1.3). So the first objective is the development of a classification scheme by simply combining the wind regimes of Sun et al. (2012) with other forcing parameter (Appendix A: Pfister et al. (2019)). Correspondingly, we want to investigate if the combination of those wind regimes with buoyancy and radiative forcing is successful in determining different temperature and flow regimes representing turbulence within the nocturnal boundary layer (Sect. 3.1). As a novelty turbulence is investigated with the FODS technique (Sect. 2) by analysing perturbations of temperature in space and time which should also reveal if the classification scheme was successful. Besides, the relationship between topography and the spatial variability should be investigated in this context.

Objective 2: Near-surface turbulence and stability are significantly altered by for example submeso-scale motions as described in Section 1.4. Accordingly, the second objective was to determine on which scale the variability within the nocturnal boundary is influenced the most and to further investigate this scale of motion with a case study (Appendix B: Mahrt et al. (2020)). The case study should reveal the relation between different air masses and flows and their impact on spatio-temporal temperature and wind speed perturbations and thus turbulence (Sect. 3.2).

Objective 3: The above described case study showed that spatio-temporal perturbations of the temperature and wind speed were the strongest during a specific submeso-scale motions. Further on, we refer to this submeso-scale motion as thermal submeso-front (TSF). Accordingly, the third objective was to use the same data set as Objective 1 and 2 and develop a detection algorithm using FODS to investigate TSFs and determine their main characteristics (Appendix C: provisionally accepted). This would be the first study detecting a submeso-scale motion spatially continuously on a high temporal resolution. The detection algorithm should objectively

determine the location of TSFs which could be utilized to investigate the horizontal and vertical structure of TSFs within the topography of the field site (Sect. 3.3).

Objective 4: This objective is related to Objective 3 as it further investigates the forcings for the formation of TSFs, the relation between TSFs and different classification schemes, and the impact TSFs on the nocturnal boundary layer (Appendix D: under review). We wanted to determine if spatio-temporal perturbations within the nocturnal boundary layer are better described by regimes or by the occurrence of TSFs. If the forcings and thus occurrence of TSFs align with a specific regime we can assume that classification schemes are capable of explaining turbulence by vertical forcing mechanisms. Otherwise further investigation of submeso-scale motions like TSFs are needed to better understand turbulence within the nocturnal boundary layer (Sect. 3.3).

2 Methods and Field site of the Shallow Cold Pool Experiment

A detailed description of parameter used for analysis can be found in Appendix A & C, here we give a brief introduction. The spatial and temporal perturbation of any parameter was determined by Reynold decomposition. The temporal scale was 60 s, while the spatial scale was chosen depending on investigated area and measurement technique. If conditional averaging was applied to an arbitrary parameter, ϕ , it was marked by angular brackets, $[\phi]$. The meteorologic sign convention is used with negative sign representing a flux towards the surface, while positive sign indicates a flux away from the surface.

As turbulence statistics we chose the friction velocity, $u_* = \left(\overline{u'_s w'^2_s} + \overline{v'_s w'^2_s} \right)^{0.25}$, and sensible heat flux, $Q_H = \rho c_p \overline{w'_s T'}$, which were computed from the measurements of the ultrasonic anemometer stations with u_s , v_s and w_s being the west-, south- and vertical-component of the wind, T the temperature as measured by each ultrasonic anemometer station, ρ the air density and c_p is the specific heat capacity. For determining wind regimes (Sect. 3.1.1) the relation between u_* and the horizontal wind speed, V , was used.

As stability parameter we chose static stability, $\Delta_z \theta$, being computed by the temperature difference between two levels, the Obukhov length, L , being defined as $L = -u_*^3 \left(\kappa \overline{w'_s T'} g T^{-1} \right)^{-1}$ with κ being the von Karman constant and g the gravitational acceleration, and the bulk Richardson number, $Ri_b = \frac{g}{\bar{\theta}} \frac{\Delta \theta \Delta z^{-1}}{(\Delta u \Delta z^{-1})^2}$, with $\bar{\theta}$ being the mean layer temperature and $\Delta \theta \Delta z^{-1}$ and $\Delta u \Delta z^{-1}$ being the vertical potential temperature and wind speed gradients. A conditional average of the bulk Richardson number, $[Ri_b]$, was calculated by the averages of $[\bar{\theta}]$, $[\Delta \theta \Delta z^{-1}]$, and $[\Delta u \Delta z^{-1}]$ instead of averaging Ri_b .

To analyze the vertical exchange of turbulence, the third order moment (*TOM*) of the vertical wind, $\overline{w'^3}$, and the sensible heat flux, $\overline{w' T' w'}$, as well as their corresponding second order moment (*SOM*) were investigated. *TOM* and *SOM* were computed with the same perturbation time scale of 60 s. The unrotated values of w_s were used for *TOM* and *SOM* to assure height consistency and being able to compare all heights on a tower.

The data of the Shallow Cold Pool Experiment (SCP) was used for my doctoral thesis and corresponding publications. A more detailed introduction is given in Appendix A. SCP was conducted in northeast Colorado, USA, over semiarid grassland at approximately 1660 m above mean sea level from 01 October to 01 December 2012 (https://www.eol.ucar.edu/field_projects/scp). Measurements with fiber-optic distributed sensing (FODS) makes it a unique study in addition to a network of 19 ultrasonic anemometer, a 20-m tower with 8 ultrasonic anemometer, and a wind profiler. FODS measurements were only conducted from 16 November until 27 November. This study analyzed the nine nights with FODS data without observational gaps from 1900 LT (local time = UTC - 7 h) until 0500 LT. An topographical overview with the instrumentation is shown in Figure 1.

SCP was also chosen due to its gentle and simple geometry which is representing

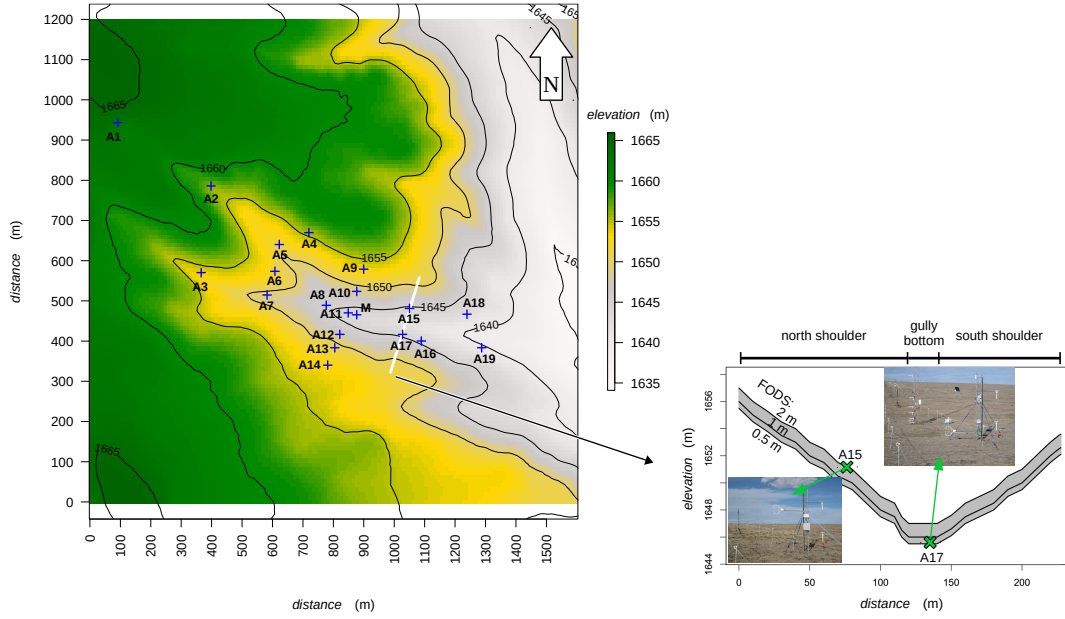


FIGURE 1: Left: Topographical overview of field site with all ultrasonic anemometer stations (A1–A19), the 20 m high main tower (M), and the fibre-optic distributed sensing transect (white line). Right: Cross-valley view of the fiber-optic transect showing its length and elevation.

most of the terrestrial earth surface (Meybeck et al., 2001). The experimental side consisted of a valley with a height difference of ≈ 27 m along a distance from roughly North-West to South-East of ≈ 1.2 km resulting in an inclination of 1.4° (https://www.eol.ucar.edu/system/files/files/field_project/SCP/SCP-RIC.kmz). The valley was asymmetric with a steeper inclination on the North shoulder ($\approx 6.0^\circ$ for a distance of 110 m) than on the South shoulder ($\approx 5.3^\circ$ for a distance of 130 m) and the valley bottom was roughly 5 m wide. Further, the North shoulder was preceded by a plateau followed by the relatively sharp elevation change (Fig. 1, left).

The FODS transect was set up as a cross-transect of the valley, however, not reaching the top of each shoulder and being located further down the valley than most instruments. This resulted in slightly different inclinations at the FODS transect with 4.4° and 3.9° , respectively (Fig. 1, right). Inclination and heights were determined by a hand-held GPS device. Right next to the FODS transect two ultrasonic anemometer stations were mounted at 0.5 m (A17) and 2 m (A15) above ground level (a.g.l.). Due to their location and in discussion with the results from the FODS we refer to those stations as measurements at the valley bottom and North shoulder, respectively.

The ultrasonic anemometer stations A1–A19 (Model CSAT3, Campbell Scientific, Logan, UT, USA) were installed at 1 m in addition to a 20 m tall main tower with eight ultrasonic anemometer (0.5 m, 1–5 m, 10 m, 20 m). At the main tower ventilated hygrometers from National Center for Atmospheric Research (https://www.eol.ucar.edu/rtrf/facilities/isff/sensors/ncar_trh.pdf) were installed at a height of 0.5 m and 15 m. Radiation measurements were from a four-component net radiometer (Model CNR4, Kipp & Zonen, Delft, Netherlands) at 2 m height about 40 m west of the FODS transect. Potential temperatures were referenced to the 1-m height of the main tower in meter above mean sea level.

The instrument for FODS (Ultima SR, Silixa, London, UK) was deployed as a 240 m cross-valley transect using an unheated optical glass fiber (FO) cable with an outer

diameter (OD) of 0.9 mm to measure temperatures and an actively heated stainless-steel FO cable (1.3 mm OD) for measurements of the wind speed orthogonal to the FO cable. Each FO cable was installed at 0.5 m, 1 m and 2 m above ground level (Fig. 1, right). The temporal and spatial resolution of the FODS measurements were 5 s and 0.25 m, respectively.

One main driver for A_h is the topography besides the static stability. We decided

to not include the topography as a parameter for the classification scheme, because defining the relevant parameter describing a three-dimensional structure would only be possible through further investigation of turbulence within different landscapes, hence, was beyond the scope of this study (Appendix A). Nevertheless, results were discussed in context of the topography.

The averaging time scale of all parameter for the night classification scheme was 5 min as this was the temporal resolution of $L \downarrow$. The combination of static stability, wind regime, and dLRF resulted in 36 different boundary-layer regimes (Fig. 2). However, some boundary-layer regimes are redundant, as for example a neutral stratification stands for a well-mixed boundary independent of dLRF or wind regime, hence, all boundary-layer regimes with neutral stratification were combined.

All forcing parameter impacted spatio-temporal temperature perturbations and thus turbulence in a unique fashion, hence, the combination of them should determine specifically different boundary layer regimes. More details on the forcing parameter as well as their impact on spatio-temporal temperature perturbations and Ri_b are given in Sections 4.1-4.3 in Appendix A.

3.1.2 Derived night classes

The three most abundant night classes with the most different combination of forcing parameter were compared to each other to verify that the classification scheme was successful. They all had statically stable conditions and the following wind regimes and dLRF classes:

- NC 1: strong-wind regime & dLRF class III (intermediate $L \downarrow$ and low fluctuation of $L \downarrow$)
- NC 3: strong-wind regime & dLRF class V (low $L \downarrow$ and low fluctuation of $L \downarrow$)
- NC 4: weak-wind regime & dLRF class IV (intermediate $L \downarrow$ and high fluctuation of $L \downarrow$)

The night classes showed different mean vertical profiles of the wind speed as well as Q_H (cf. Fig. 10 in Appendix A). The profiles overlapped, but the mean values were different even though NC 1 and NC 3 had the same wind regime. This was already the first sign that the classification scheme was successful.

In the following the spatio-temporal temperature perturbations, and bulk Richardson number, Ri_b , of the night classes were compared to each other (Fig. 3). Further, case studies for each night classes were analyzed to characterize and compare the flow and temperature regimes of each night class. Therefore, the multiresolution decomposition technique (MRD) in combination with a two-point correlation coefficient was used to investigate how spatially homogeneous the temperature evolution was on different time scales (cf. Sect. 2.1 and Fig. 13 in Appendix A). With this technique also the extent of a cold-air pool could be determined when analyzing longer time scales (≥ 16 min) assuming a spatially homogeneous low temperature within a cold-air pool.

The most abundant night class NC 1 had the strongest spatio-temporal temperature perturbations (Fig. 3 a & b) being elevated on the North shoulder, decreasing towards the valley bottom, and being low on the South shoulder. Especially the high temporal temperature perturbation on the North indicated topographically induced mixing which was supported by high friction velocities, u_* , and simultaneously elevated temperatures at station A15 on the North shoulder. Further, the MRD revealed a drop in the correlation coefficient on the North shoulder indicating that

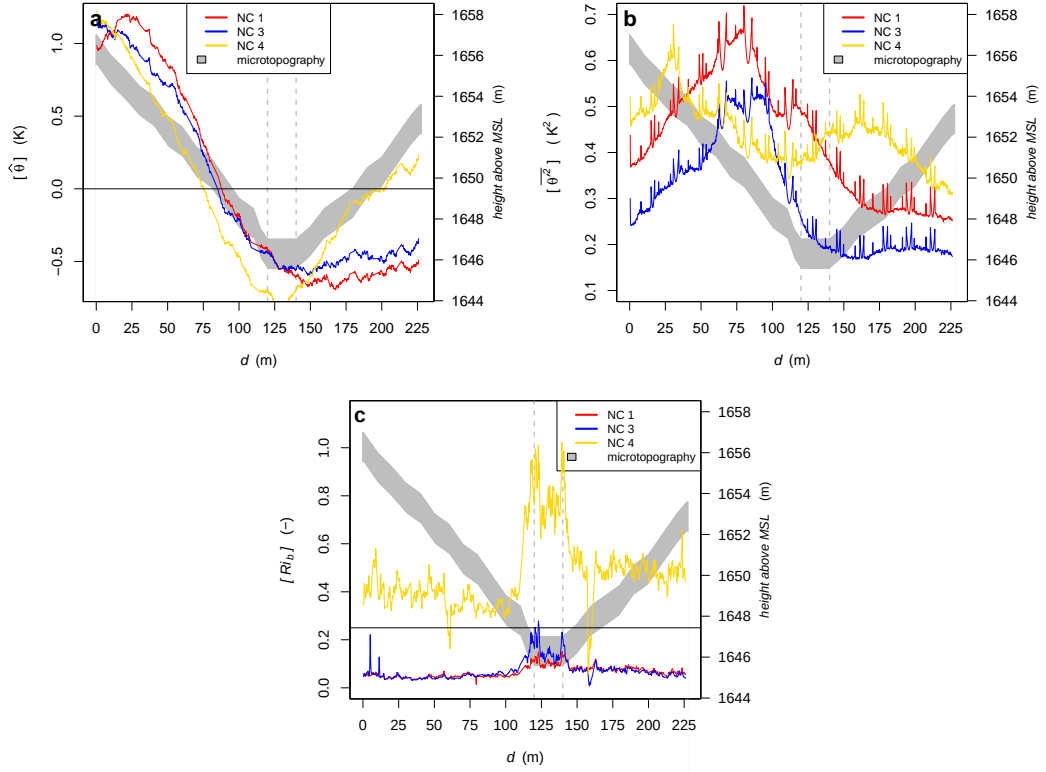


FIGURE 3: (a) Spatial, $[\hat{\theta}]$, and (b) temporal, $[\hat{\theta}^2]$, temperature perturbation, and bulk Richardson number, $[Ri_b]$, conditionally averaged for each night class (cf. legend) and plotted against their distance, d , from the start of the fiber-optic transect on the North shoulder.

two different processes changed the temperature (Fig. 13a & b in Appendix A). We conclude and suspect that the two processes are cold-air drainage or pooling at the valley bottom and turbulent mixing elevating temperatures on the North shoulder. On the North shoulder a relatively sharp elevation change took place (Sect. 2) which could induce the mixing. The radiative forcing was rather weak, but the MRD as well as Ri_b (Fig. 3c) revealed that there was a cold-air layer being at least 1 m thick and roughly 30 m wide above the valley bottom. Consequently, the boundary layer of NC 1 is mainly mechanically forced by topographically induced turbulent mixing on the North shoulder during rather strong winds and only some cold-air accumulation at the valley bottom due to strong enough radiative forcing.

The night class NC 3 was similar to NC 1 as it also featured topographically induced mixing, but it had stronger cold-air formation due to stronger radiative forcing. Also Ri_b were higher (Fig. 3 c) at the valley bottom, while u_* and wind speeds were a bit lower during NC 3. This resulted in a thicker the cold-air layer above the valley bottom with a horizontal extent of roughly 50 m. Consequently, the boundary layer of NC 3 is the concurrence of mechanical and radiative forcing due to weaker topographically induced mixing on the North shoulder and stronger cold-air drainage and pooling at the valley bottom than NC 1.

The night class NC 4 supported cold-air formation more than NC 1 & 3 due to the weak-wind regime and rather conducive radiative forcing. Spatial temperature perturbations followed the topography with the lowest values at the valley bottom and higher values on the shoulder (Fig. 3a). Surprisingly, the net radiation, ΔL , of NC 4

had the lowest mean value of all night classes which would have indicated less spatial temperature perturbations due to the weak radiative forcing. This emphasizes that the choice of dLRF over ΔL is justified. Further, due to the weak winds inversions were stronger while the vertical wind speed shear was lower resulting in Ri_b being > 0.25 all along the transect and even with values up to 1 at the valley bottom (Fig. 3c). This indicates a transition to a laminar flow. We conclude that cold-air drainage took place all along the transect during NC 4. But there was most likely still some topographically induced mixing as the temporal temperature perturbation was elevated at the North shoulder (Fig. 3b), however, it was less pronounced compared to NC 1 & 3. Consequently, during NC 4 the weak-wind regime predominantly forced the boundary layer resulting in cold-air drainage and less topographically induced mixing.

Apart from the classification scheme, Ri_b was spatially very heterogeneous independent of temperature or flow regime. This makes the assumption of a spatial homogeneous Ri_b as done by modellers questionable. Further, for observations and classification schemes the measurement location of Ri_b is important as one location can not represent the dynamic stability of the boundary layer. Consequently, for the insight into the turbulence structure of the nocturnal boundary layer FODS is an essential tool revealing how spatial heterogeneous parameter like Ri_b can be which was not investigated in such detail by other studies.

In summary, the night classification scheme determines three different temperature and flow regimes with distinctive different turbulence as shown by the spatio-temporal perturbations of temperature and Ri_b , and thus was successful. Topography induces spatio-temporal perturbations especially on the North shoulder. We suggest to further investigate the influence of topography on turbulence at other field sites with similar as well as different topography. Maybe a useful forcing parameter reflecting topography can be added. We also recommend to further investigate the connection between the night classes and flows on different time scales like gravity waves, meandering, or submeso-scale motions to proof the usefulness of this classification scheme.

3.2 Small-Scale Variability in the Nocturnal Boundary Layer

Turbulence within the nocturnal boundary layer is significantly influenced by motions on different scales (Sect. 1.4). So the variability in the nocturnal boundary layer on different temporal scales was investigated to determine on which scale the variability is impacted the most. The nocturnal variability of temperature and wind speed was investigated and compared with each other at three different field sites with gentle topography (Appendix B). Especially the small-scale variability was investigated as those are usually caused by submeso-scale motions which change the relation between turbulence and stability parameter.

The magnitude of variability was the strongest for time scales from 10 min to 1 hour and usually exceeded the nocturnal trend of cooling. This variability could be related to wave-like motions or more complex modes (cf. Sect. 3 in Appendix B). Accordingly, a case study featuring such a motion was analyzed at the SCP field site because it had the most extensive network and had spatially explicit observations through FODS (Sect. 2).

The case study could be separated into three different events: A near-surface South-Westerly flow, followed by the formation of a transient cold-air pool being advected

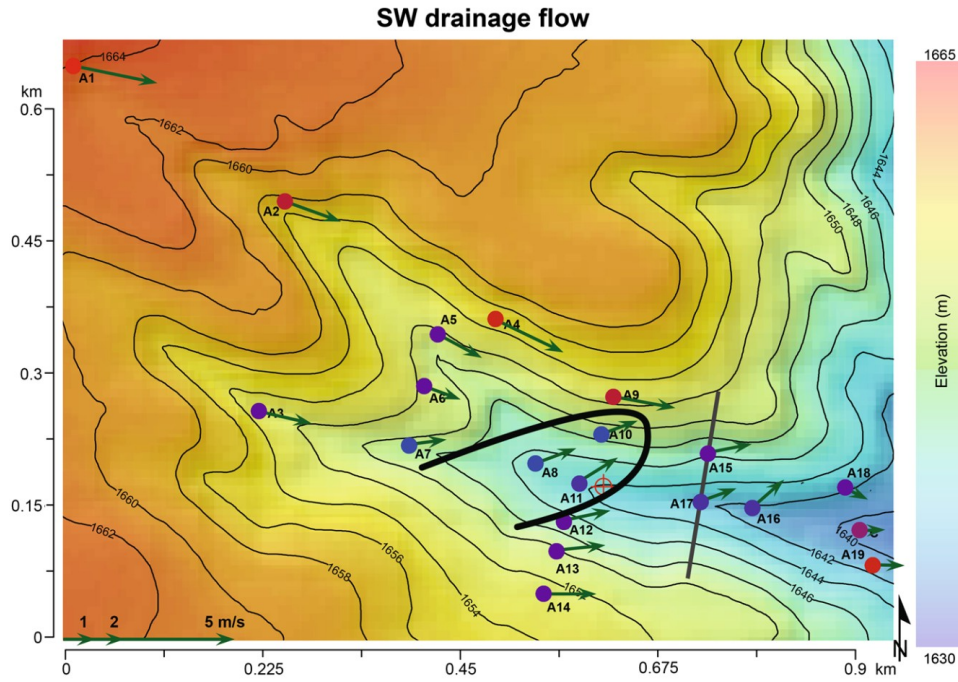


FIGURE 4: The spatial distribution of the temperature and wind averaged over the 5-min period ending at 2000 local time. The temperature ranges from 1°C (blue circles) to 6°C (red circles). The solid black line roughly outlines the core of the south-west drainage flow. The thin grey line through stations A15 and A17 is the fiber-optic transect. The red + marks the tower location.

upslope the North shoulder, and then the erosion of South-Westerly flow and cold-air pool air by a warm microfront (Fig. 6 in Appendix B).

The South-Westerly flow was mainly observed by stations on the South shoulder and within the valley (Fig. 4) during low wind speeds above the valley. All other stations showed higher wind speeds and were following the regional flow from West-North-West. Accordingly, wind speed and direction was spatially heterogeneous during the South-Westerly flow which usually only occurred intermittently. It was most likely caused by cold-air drainage down the south-westerly slope of the valley and was a main, frequently occurring feature of the SCP experiment.

During the low wind speeds above the valley a transient cold-air pool could form. The episode of the cold-air pool was characterized by especially low turbulence and wind velocities at station A11 at the valley bottom. Accordingly, we concluded that even though the topography is gentle it probably provided enough shelter for the cold-air pool formation. Due to the simultaneous South-Westerly flow the cold-air pool was displaced uphill towards the North shoulder and thus the coldest temperatures were found uphill instead of at the valley bottom (Fig. 4, black line). The displacement created a sharp boundary between the displaced cold air and the warm air on the North shoulder. On the North shoulder the topography influenced near-surface temperatures by inducing additional mixing elevating temperatures (Mahrt, 2017b). Accordingly, the temperature difference between the cold-air and adjacent warm air was usually several Kelvin and could be observed most nights. The two different air layers are also shown in Figure 5.

As soon as wind speeds pick up the wind direction of the whole network had spatially homogeneous wind directions and spatial perturbations of the temperature

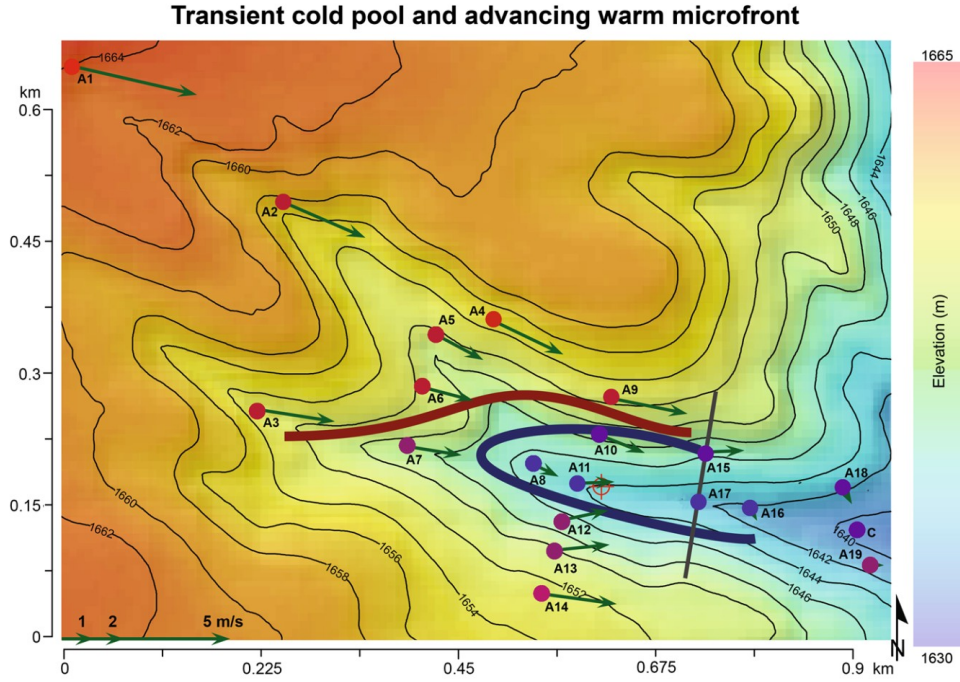


FIGURE 5: The spatial distribution of the temperature and wind averaged over the 5-min period ending at 2000 local time. The temperature ranges from 1°C (blue circles) to 6°C (red circles). A plausible sketch of the warm microfront (thick red line), which propagates from the north-north-west in contrast to the surface wind, which is more from the west-north-west. Based on the tower observations, warm air passes over the transient cold pool (thick blue line) and then mixes downward to the valley floor. The thin grey line through stations A15 and A17 is the fiber-optic DTS transect. The red + marks the tower location

vanished, hence, the transient cold-air pool as well as the cold-air drainage generating the South-Westerly flow were eroded. The erosion of cold air took place within 5 min. As most stations on the North shoulder showed elevated temperatures even during the South-Westerly flow, we conclude that a warm microfront can induce enough mixing and advect warm air to erode any cold air. When wind speeds are strong enough the warm microfront descends and erodes any cold air within the valley.

In summary, small-scale variability of the nocturnal boundary layer is influenced the most by submeso-scale motions. This was further investigated in a case study which showed that the topography and radiative cooling created two competing air masses. The radiative cooling formed a transient cold-air pool which was advected uphill by a cold-air current from South-West. In this case the topography induced the cold-air drainage from outside the valley but also provided shelter for the cold-air pool within the valley. Simultaneously, on the North shoulder near-surface temperatures were elevated due to topographically induced mixing creating a warm microfront. This warm microfront created a sharp boundary with the displaced cold-air pool. When wind speeds pick up the warm microfront can propagate into the valley and erode cold air and thus spatial temperature as well as wind speed perturbations vanish. Consequently, the air masses significantly impact the small-scale variability of temperature, wind speed, and turbulence for stations within the valley, but their forcings and relation to the non-turbulent flow or even regimes needs to be further investigated beyond a case study.

3.3 Thermal Submeso-Fronts

Within the fiber-optic transect the above described air masses were detected with warm air on the North shoulder and adjacent cold air creating a sharp boundary. However, this sharp boundary was not stationary nor limited to a few incidents. It was found almost every night lasting between several tens of seconds up to an hour and was systematically moving up and down the northern valley side wall. Accordingly, we investigated this motion which we refer to thermal submeso-front (TSF) in a broader analysis (Appendix C & D) than the case study presented in Section 3.2. An example of an episode with TSFs is shown in Figure 6 and a video can be downloaded visualizing TSFs with the FODS data under this [link](#).

3.3.1 Detection and Analysis of Thermal Submeso-Fronts

A detection algorithm was developed to objectively determine the TSF boundary within the fiber-optic transect. Therefore, the sharp boundary between warm and cold air was utilized by finding the maximum horizontal temperature difference, $\Delta_x\theta$. This was a three-step process to objectively determine the TSF boundary:

1. optimal separation distance for $\Delta_x\theta$:
 $\Delta_x\theta$ was the temperature difference between two bins of the FODS measurement with a fixed separation distance. All bin-pairs of the fiber-optic transect were computed and the maximum $\Delta_x\theta$ determined for each time step and each level of the transect. The location of the maximum $\Delta_x\theta$ was the center between the bins. After visually analysing the results of separation distances ranging from 0.5 m up to 16 m, a separation distance of 4 m was considered optimal.
2. threshold for $\Delta_x\theta$:
 The threshold determined whether a TSF occurred or not, hence, whether FODS indicated spatial heterogeneous or homogeneous temperature perturbations which was determined by the uncertainty of the measurements. Therefore, the uncertainty of temperature differences, δ_T , was determined by $\delta_T = \sqrt{2\sigma_{FODS}^2}$ with σ_{FODS} being the root mean error of the temperature difference between a reference probe and the FODS temperature measurements within a temperature controlled calibration bath. The threshold for $\Delta_x\theta$ was 0.73 K.
3. minimum duration of TSF:
 TSFs had to last continuously for at least 40 s to be considered.
4. remove unphysical TSF movement:
 As the advective velocity was usually an order of magnitude lower than the mean wind speed, we decided to discard a TSF boundary if the advective velocity was bigger than the maximum wind speed during the analyzed nights.

The detection algorithm was successful in determining the TSF boundary as shown in Figure 6 by a solid black line.

The unique feature of the studies in Appendix C & D is conditional averaging using the information about the occurrence as well as the actual location of TSFs. Therefore, a relative distance to the TSF boundary for each measurement location of an arbitrary parameter, ϕ , was determined. A negative sign of the relative distance indicated that ϕ was measured within the warm air, while a positive sign indicated cold air (cf. Fig 6b). Conditional averaging depending on the relative distance to the

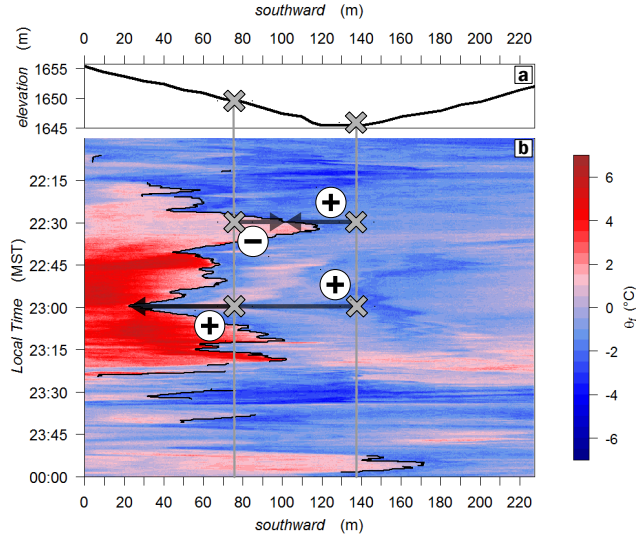


FIGURE 6: (a) Length of fiber-optic transect and elevation in metres showing the cross-valley topography. (b) Potential fibre-optic temperatures θ_f (colour bar) within the valley in a space–time–diagram. Two examples are given how the distance to the thermal submeso front was assigned for both ultrasonic anemometer stations (grey crosses and vertical lines) with the help of black arrows and +/− signs reflecting the sign for the distance.

TSF boundary was only possible for the ultrasonic anemometer stations A15 and A17 of the sensor network (Fig. 1 & Fig. 6a) as they were set up next to the fiber-optic transect. All other stations including the wind profiler data were conditionally averaged depending on the occurrence and absence of TSFs.

As shown above, FODS was intrinsic for the determination of TSFs. There are some other techniques using point observations to detect TSFs. A frequently passing TSF can cause meandering (cf. Sect. 4.1 in Appendix D), hence, for example Eulerian auto-correlation functions could be utilized to determine the occurrence of TSFs by combining wind directional change with scalars or temperature (Mortarini et al., 2019; Stefanello et al., 2020). As a passing TSF also enhances other turbulence statistic like $\overline{w'w'}$ (not shown), also a clustering method as developed by Vercauteren and Klein (2015) could be used to determine if a TSF had passed. Or a cross-correlation function method on rather long time scales (20 min) could be used as done by Lang et al. (2018) to study the propagation of structures between stations. However, even if the described methods are successful in determining TSFs, the location of the observations within the topography is important. For the SCP experiment not all station were passed by TSFs like stations on the South shoulder, while other station like the ones at the valley bottom and the main tower were passed only a few times compared to stations on the Norther shoulder. The station A15 and A17 together were within the transition area of TSFs for 16.1% of all occurrences with TSFs. As only a passing TSF can be detected by a station the actual detection of TSFs by each point observation is even lower. TSFs were most of the time between towers and thus TSFs were mostly invisible even when using all point observations within the dense network of the SCP experiment.

Consequently, only FODS can detect TSFs continuously as even a dense network of ultrasonic anemometer miss the slow moving TSFs most of the time and thus can not determine their propagation and advective velocity accurately.

3.3.2 Horizontal and vertical structure of Thermal Submeso-Fronts

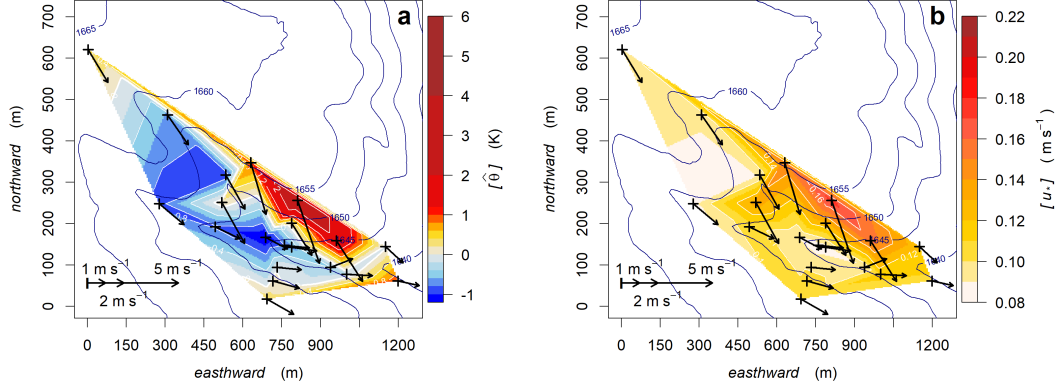


FIGURE 7: Overview of field site with elevation shown by contour lines (dark blue). (a) The mean spatial temperature perturbation, $[\hat{\theta}]$, and (b) the mean friction velocity, $[u_*]$, during the occurrence of TSFs added as filled contour lines.

For the first time the mean advective velocity of a submeso-scale motion (0.2 ms^{-1}) and its structure could be investigated in detail. The horizontal structure of TSFs was investigated using the complete network and conditional averaging spatial perturbations within the nocturnal boundary layer depending on the occurrence of TSFs (Fig. 7). Due to this averaging the parameter reflect the mean location of TSFs within the valley. The warm air spans a horizontal scales of 200-300 m along the North shoulder, while the cold air is mainly found at the valley bottom (Fig. 7a). TSFs lasted between 40 s and 1 hour, hence, the temporal and spatial scale of TSFs is characteristic for submeso-scale motions. TSF usually occurred during a weak regional flow (Sect. 3.1 in Appendix C). The main characteristic of the warm air is elevated temperatures and friction velocities at the North shoulder with the flow following the regional flow, while the cold air lower friction velocities with a flow following the topography (Fig. 7b). Accordingly, also the flow strength and direction was very different between the air masses highlighting their competing characteristics. Above the valley bottom these air masses were stacked above each other (Sect. 3.2 in Appendix C), hence, in the following we refer to warm-air and cold-air layer as they were seen as such at the 20 m high main tower or other studies using vertical observations above the valley bottom.

The competing characteristics of the warm-air and cold-air layer were also observed when conditionally averaging other parameter depending on their distance to the TSF boundary (Fig. 8). The mean temperature difference between warm and cold air was 3.4 K , while the wind speed dropped by $\approx 1.5 \text{ ms}^{-1}$. Similarly, the friction velocity dropped by $\approx 0.10 \text{ ms}^{-1}$ and the strength of sensible heat flux by $\approx 30 \text{ Wm}^{-2}$. Dynamic stability as expressed by Ri_b was similar between the air layer, but showed peak values within the transition area where the air layers merge. Further, within the transition area of TSFs the warm-air layer is forced upwards as the dense cold-air layer acts like a barrier resulting in a positive w_s at the TSF boundary (Sect. 3.4 in Appendix C). Consequently, the impact of TSFs on spatio-temporal temperature perturbation and turbulence within the nocturnal boundary layer is significant. Especially if the TSF is passing a station frequently turbulence statistics or wind direction can change intermittently within minutes causing intermittent turbulence and meandering.

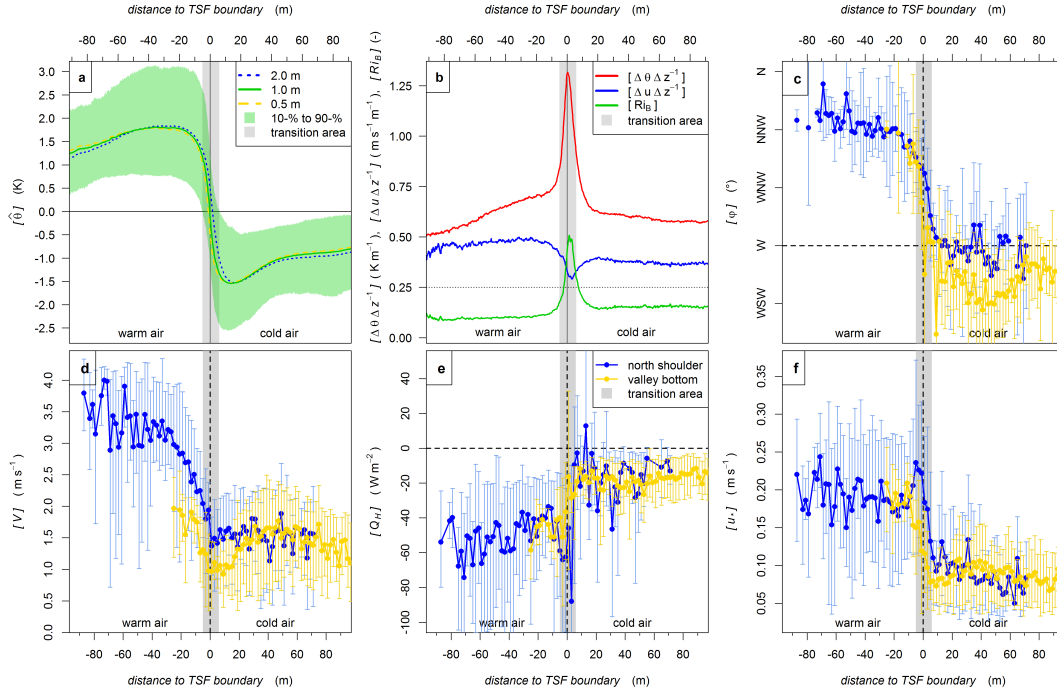


FIGURE 8: Most important parameter describing thermal submeso fronts (1-min averages) which were conditionally averaged depending on their distance to the boundary of the fronts: fiber-optic measurements of (a) spatial temperature perturbation, $[\hat{\theta}]$, and (b) the bulk Richardson number, $[Ri_B]$, derived from the ratio of buoyancy, $[\Delta\theta \Delta z^{-1}]$, to shear, $[\Delta u \Delta z^{-1}]$, as well as ultrasonic anemometer measurements showing (c) the mean wind direction, $[\varphi]$, (d) mean wind speed, $[V]$, (e) sensible heat flux, $[Q_H]$, and (f) friction velocity $[u_*]$.

The vertical turbulent transport was investigated to derive the vertical structure of TSFs. The vertical turbulent transport was determined by the third and second order moment of the vertical wind speed as well as sensible heat flux (Sect. 2 & Sect. 4.2 in Appendix D). During TSFs the cold-air layer was decoupled from the warm-air layer as no vertical transport was evident. Further, the 20-m station was in equilibrium with the regional flow while the 10-m station with a higher variance of the third and second order moment was still adjusting to it. During the absence of TSFs an effective downward transport to the lowest levels was observed, hence, cold-air layers were most likely eroded. This scenario is also described during the case study of Section 3.2 when the described warm microfront descends into the valley.

The insights gained from this and further analysis (Appendix C) was summarized in a conceptual diagram of TSFs in Figure 9. As discussed in Appendix C the cold-air layer most likely originates from non-local cold-air advection and has enough momentum to move uphill the North shoulder of the valley where the cold-air layer forms the TSF together with the warm-air layer. This is also described in the case study of Section 3.2 by the (non-local) South-Westerly flow displacing the transient cold-air pool. The warm-air layer itself is formed by topographically induced mixing due to the relatively rapid elevation change at the North shoulder elevating near-surface temperatures. Consequently, the topography plays an important role in the formation of TSFs as the topography induced non-local cold-air advection, provided shelter for the formation of a transient cold-air pool, and induced turbulent mixing forming the warm-air layer.

In summary, we can determine TSFs locations accurately and objectively using the developed detection algorithm and FODS data. Through the detection algorithm and conditional averaging we were able to investigate the horizontal and vertical structure of TSFs and could investigate turbulence statistics within the air layers and at the TSF boundary in detail. FODS is essential for characterizing a submeso-scale motion. Further, the topography even though it was gentle plays a major role in forming TSFs and should not be underestimated.

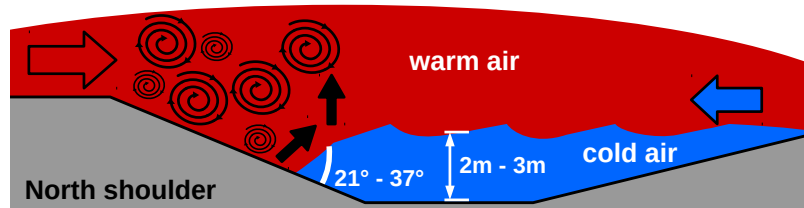


FIGURE 9: Conceptual drawing of a thermal submeso front (not to scale) within the valley (grey areas) consisting of a warm-air layer (red) and a cold-air layer (blue). Coloured arrows indicate the different flow direction of the air layers, while black swirls indicate the topographically induced mixing. At the transition area, where the air layers merge, the warm-air layer is pushed upwards (black arrow) as the cold-air layer is like a barrier.

3.3.3 TSFs forcings and implications for the boundary layer

Parameter and flows forcing TSFs were investigated in detail, however, no simple threshold or combination of parameter could be determined indicating the formation of TSFs (Sect. 4.3 in Appendix D). Nevertheless, we can summarize that static stability is elevated during TSFs due to the stacked air layers, TSFs occur irrespective of radiative forcing, TSFs occur during rather low wind speeds, but the maximum wind speed during which TSFs occur differed from the wind speed threshold of the wind regime, the TSFs location is related to a change of the wind speed, but TSFs do not move with the wind, and no specific synoptic flow like a low level jet determines the occurrence of TSFs.

Correspondingly, the classification scheme of the nocturnal boundary layer as described in Section 3.1 failed in detecting TSFs. All three night classes had TSFs occurring for roughly 40% of the time. Further, the elevated spatio-temporal temperature perturbations were aligned with the TSF location, hence, the mean statistics of the night classes are rather a sub-sample of different TSF locations. We summarized four possible reasons why the night classification failed in detecting TSFs. Firstly, the air layers of TSFs form independent from each other as each layer can exist without the other still forming a strong enough temperature difference to find a TSF boundary. The cold-air layer can form during strong enough radiative forcing especially during mostly calm conditions. In this case the TSF boundary would be the top of a formed cold-air pool. Vice versa topographically induced mixing elevates near-surface temperatures as soon as wind speeds are strong enough. Secondly, the detection of a cold-air or warm-air layer is still possible during low radiative forcing or low wind speeds as each layer can persist for a certain amount of time without the needed external forcing. Thirdly, a point observation within the network only shows the characteristics of one layer. Accordingly, the occurrence of TSFs consisting of two distinct air layers by one point observation can not be successful. Fourthly, in the mentioned studies no adjustment time scale between the change in bulk forcing to a change in

turbulence was taken into account (Mahrt and Thomas, 2016). Maybe a more clear relation between forcing mechanisms and submeso-scale motions emerges when accounting for an adjustment time scale.

Following the objectives, we also investigated the relation between TSFs and other classification schemes. As described in Section 1.3, one commonly used approach to classify the boundary layer are wind regimes as introduced by Sun et al. (2012). However, the TSFs were not related to a specific wind regime, because the wind speed range during which TSF occurred (Appendix C & D) did not match with the wind speed threshold of the SCP field campaign. Nevertheless, we had the hypothesis that the cold-air layer with low wind speeds and turbulence statistics could represent the weak-wind regime, while the warm-air layer could represent the strong-wind regime. If this hypothesis is true, even the location of TSFs within the whole network could be roughly determined by analyzing the wind regime at each station.

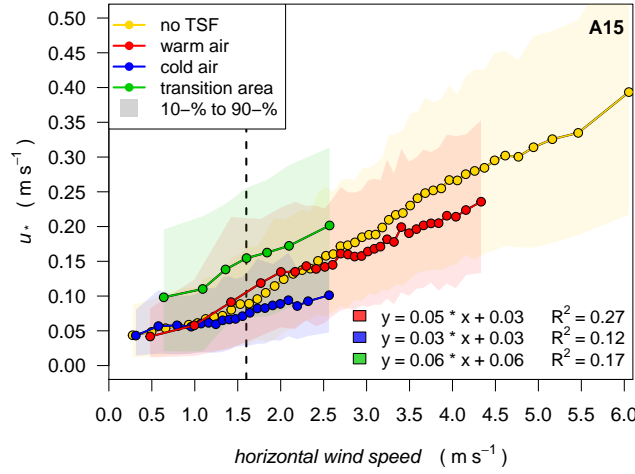


FIGURE 10: Relation of horizontal wind speed to friction velocity, u_* , for each air layer and the transition area of TSFs (cf. legend). vertical line: threshold value separating weak-wind and strong-wind regime following the work of Sun et al. (2012); points: equally sized bin-averages.

The wind speed threshold for the station A15 (2 m above ground level) was 1.6 ms^{-1} irrespective of the occurrence of TSFs. In Figure 10 the relation between the horizontal wind speed, V , and friction velocity, u_* , for each air layer is plotted and illustrated by equally sized bin-averages. Each air layer showed a specific relation between V and u_* , but neither of them was confined to one wind regime. The warm-air layer had most data within the strong-wind regime (91%), but the cold-air layer also had almost half of its data (47%) within the same regime. We conclude that the wind speed range of the air layers overlap, hence, can not be separated by a simple threshold.

Note that for the transition area of TSFs the relation between V and u_* is similar to the one of the warm-air layer but with elevated u_* . This relationship reflects intermittent turbulence which usually is assumed to be generated by a down-burst of turbulence (Sun et al., 2012, 2016), however, here we show the opposite (cf. Sect. 4.4 in Appendix D). Consequently, we conclude that intermittent turbulence is caused by TSFs and is a bottom-up process.

The different relation between V and u_* underline the different dynamics of each

air layer. We speculate that within the decoupled cold-air layer the mechanical generation of turbulence is superseded by thermo-dynamics and thus u_* only slowly increased with V , while within the well-coupled warm-air layer even during wind speeds lower than the threshold the strong relation between V and u_* persisted.

We admit that the above wind regime does not account for any specific thermal regime. Van de Wiel et al. (2017) and Maroneze et al. (2019) reported that the minimum needed wind speed to sustain near-surface turbulence depends on thermal regime which is similar to the wind speed threshold of Sun et al. (2012). The most recent study of Sun et al. (2020) also report a change in wind speed threshold for different thermal regimes. Nevertheless, at the SCP field site we could not find a change in the wind speed threshold even when separating the boundary layer into stronger and weaker static stability (Section 4.4.2 in Appendix D).

Another very commonly used classification of the boundary layer is the weakly and very stable regimes as established by Mahrt (1998). The thermal is determined by relation of the Obukhov length, z/L , to the kinematic heat flux, $\overline{w'T'}$. During TSFs we assumed that the very stable regime dominantly would occur within the cold-air layer while the weakly stable regime would be connected to the warm-air layer. If each layer falls into one thermal regime and this accordingly adjusts the wind speed threshold, the air layers could be successfully separated by one threshold or by simply a thermal regime (Fig. 11).

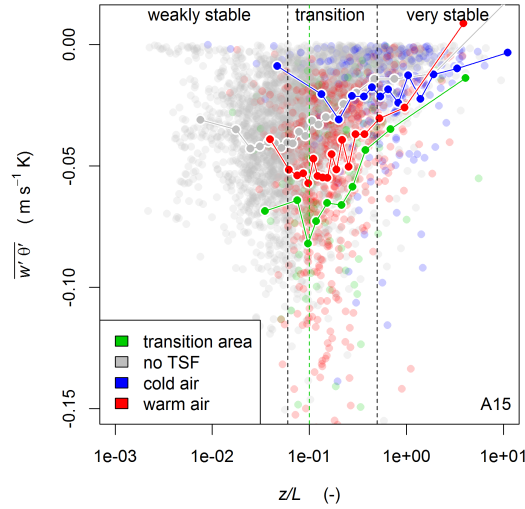


FIGURE 11: Thermal regimes as defined by Mahrt (1998) separating the boundary layer into the weakly and very stable regime by using the Obukhov length, z/L , and kinematic sensible heat flux, $\overline{w'T'}$. Equally-sized bin averages (dotted lines) were computed for the different air layers of thermal submeso fronts (cf. legend).

Vertical lines and text indicate the regime change from weak to very stable.

The air layers of TSFs did not represent one thermal regime and they significantly overlapped. Substantial scatter around the bin averages were observed which was most likely caused by differences in radiative or non-local forcings like the regional flow or varying and unknown adjustment time scales to that. Nevertheless, no clear relation could be determined. So we conclude that also the thermal regime does not indicate the air layers of TSFs. Further, even if the wind speed threshold change with thermal regime, the air layers of TSFs can not be represented by a regime change as

determined by z/L or static stability as many confounding and interdependent factors are at work creating substantial scatter around mean values.

In summary, even though TSFs significantly impact turbulence within the nocturnal boundary layer no classification or boundary layer regime indicate their occurrence. The air layers are inducing strong spatial perturbations and any local measurement will usually only capture one air layer and not the occurrence of TSFs. Also external or larger scale forcing can not determine the occurrence of TSFs as we could not determine a clear threshold for any parameter. Consequently, classification of the nocturnal boundary layer by vertical forcing mechanisms does not capture small-scale variability of the boundary layer as well as the detection of submeso-scale motions. But the physics of submeso-scale motions are not yet fully understood and need to be further investigated preferably by combining FODS with other measurement techniques.

3.3.4 Recommendations and Thoughts for further Studies

Stations outside the valley would have been conducive to determine the source of cold-air advection during TSFs while at the same time not all stations within the valley would have been necessary. For future studies and deployments we recommend the following:

- Topographical features influencing the boundary layer need to be determined before the start of a bigger field campaign. This should also determine where spatial continuous data like FODS (if possible) should be deployed for maximum outcome. We also recommend FODS in the vertical to better investigate distinct layers and corresponding turbulence within the nocturnal boundary layer.
- Nested networks should be used which have an instrumentation density gradient from high density along the main topographical features under study (e.g. cross-valley, down-valley, vertical above valley bottom) to low density outside the valley (towards higher and lower elevation in all directions). For clarifying synoptic forcing a wind profiler and tower data (as high as possible) is important. This should achieve the best possible three-dimensional observation within a valley and also clarify non-local advection.
- The combination of sonic anemometer measurements and FODS gave new insights into the nocturnal boundary layer and submeso-scale motions as shown within this work, hence, we highly recommend doing this.
- Even though FODS is a strong tool, the application is still limited. The maximum length a FODS device can evaluate is 5-10 km. A three-dimensional setup can be done for tracking cold-air currents in fine detail like in [Zeeman et al. \(2015\)](#), however, the origin of cold air remains unknown if the ancillary network does not capture this. Accordingly, when trying to deploy FODS in the field its strength as well as limitation needs to be kept in mind.
- Another study focusing on the evolution of submeso-scale motions should be beneficial for experimentalists and modelers.
- Modeling studies and new classification schemes need to incorporate the impact of topography and horizontal advection to investigate turbulence within the nocturnal boundary layer.

4 Conclusion

My doctoral thesis was based on the data from the Shallow Cold Pool experiment (SCP) featuring a unique combination of different measurement techniques: ultrasonic anemometer network with 19 stations within the valley and 8 stations on a 20-m tower, wind profiler, standard meteorologic measurements like temperature and radiation, and fiber-optic distributed sensing (FODS) along a cross-valley transect. The gentle terrain of the field site was chosen as commonly it is assumed to have a rather small impact on the nocturnal boundary layer and represents most of the earth's surface. With this setup we were able to test a new classification scheme of the nocturnal boundary layer and investigate a submeso-scale motion in detail. We could give insights into the relation between this submeso-scale motion and commonly used classification schemes and could give recommendations for further field studies.

The new classification scheme was developed using wind regimes in combination with static stability and downwelling longwave radiative forcing. The three most abundant and most different night classes being derived by the combination of those forcing parameter showed significantly different perturbations of the temperature in space and time as well as different temperature and flow regimes. NC 1 was mostly dynamically forced and had only a limited degree of cold-air formation. NC 3 showed an interplay between cold-air drainage and pooling within the valley and topographically induced mixing. NC 4 was similar to NC 3, but showed stronger cold-air formation and a weaker influence of topographically induced mixing. Consequently, the presented classification scheme is successful in sorting data into different regimes representing turbulence within the boundary layer. Besides, due to FODS we could give unique insights into the spatial perturbations of the bulk Richardson number, Ri_b , which is especially relevant for modelling studies. Ri_b showed a strong spatial heterogeneity and varied within the topography with the highest value at the valley bottom. Accordingly, the use of Ri_b at a single location to determine dynamic stability of the boundary layer is questionable. Even though the topography of the field site was gentle it impacted all three night classes significantly by forming cold-air drainage and pooling by inducing mixing on the North shoulder.

The relevant scale during which the variability of the temperature of the nocturnal boundary is increased the most is the submeso scale. Here the variability of temperature is usually larger than the nocturnal temperature trend. Correspondingly, a case study for the SCP data set was determined which investigated submeso-scale motions in detail. During SCP when wind speeds were low, a South-Westerly flow as well as transient cold-air pool developed, however, during higher-speed periods those were eroded by a warm microfront. The South-Westerly flow was strong enough to displace the cold-air pool uphill the North shoulder. At the North shoulder temperatures were usually elevated due to turbulent mixing at the elevation change. Accordingly, the two air masses created a sharp boundary which we refer to as thermal submeso-front (TSF). Topography plays an important role by providing shelter for the formation of the transient cold-air pool, by inducing the South-Westerly flow, and by inducing mixing at the North shoulder even within this gentle

topography. Cold air and thus the South-Westerly flow and transient cold-air pool were eroded within 5 min when the warm microfront descended into the valley. We anticipate that these interactions and corresponding submeso-scale motions are globally common. Further investigations are necessary to fully understand the relation between temperature variability, wind speed and direction, the formation of such motions, and the topography.

Consequently, a detection algorithm was developed to objectively determine the TSF location. This study was the first one being able to continuously track a submeso-scale motion. With this detection algorithm we were able to determine the main characteristics of TSFs. They were frequently occurring within the stable boundary emphasizing their relevance for the nocturnal boundary layer. TSFs consist of a warm-air and an adjacent cold-air layer non-stationary moving up- and downhill the valley side wall in a wave like motion. The coldest air was usually found uphill on the North shoulder instead of the valley bottom, hence, a non-local advection providing enough momentum to keep the cold-air uphill against buoyancy force is most likely. The non-local advection was most likely represented by the South-Westerly flow during the case study. As can be expected, the warm-air layer showed strong wind speeds and turbulence statistics as indicated by u_* and Q_H , while the cold-air layer had a weak flow and corresponding weak turbulence. We concluded that the warm-air layer is mechanically generated by topographically induced turbulence consistently elevating near-surface temperatures at the plateau-edge, while the cold-air layer is thermo-dynamically driven by topographically induced cold-air drainage and pooling with low near-surface temperatures. Accordingly, even in this gentle terrain, the impact of topography is bigger than usually anticipated. Besides, through FODS also new insights could be given into the interaction between the air layers at the TSF boundary and into the vertical structure of TSFs. TSFs vanished during strong wind speed and spatially homogeneous wind direction which most likely erodes any cold air which was described a descending warm microfront in the case study. FODS proved to give insights into the boundary layer beyond the capability of point observations as even the dense network of the SCP experiment missed a passing TSFs and thus its occurrence most of the time. Consequently, the key to these insights was the use of FODS to determine the occurrence of TSFs and their location and to combine this knowledge by conditionally averaging different parameter. We conclude that turbulence within the nocturnal boundary layer as induced by submeso-scale motions can only be accurately investigated when using FODS.

TSFs and thus submeso-scale motions impact the nocturnal boundary layer, as spatio-temporal perturbations were elevated everywhere a TSF was located. Also the night classes of the first study all had occurrences of TSFs ($\approx 40\%$ of the data). The spatio-temporal perturbations were different between the night classes, but most likely only because of a different subset of TSF locations. Accordingly, TSFs impact the nocturnal boundary layer significantly, while the relevance of night classes is questionable due to the occurrence of TSFs during all of them. Besides, we could determine further implications of TSFs on the boundary layer emphasizing that the detection of TSFs is more relevant than external forcings. During TSFs ergodicity assumptions are invalid as the advective velocity of TSFs is an order of magnitude lower than the mean wind speed. The decoupled cold-air layer also invalidates flux-gradient similarity theory above the valley bottom. Intermittent turbulence is related to TSFs and thus is a bottom-up process at least during TSFs. As the air layers of TSFs lay

above each other within the valley, static stability as is commonly measured at the valley bottom is increased beyond the capability of radiative forcing. Unfortunately, no distinct forcing for TSFs nor a relation to a wind or thermal regime could be determined. We conclude that the occurrence of TSFs is more relevant to understand turbulence within the nocturnal boundary layer than classification schemes based on external forcings or vertical forcing mechanisms.

The boundary layer is usually classified in a top-down or bottom-up approach by using larger-scale flow conditions (e.g. LLJ or geostrophic winds), local thermal regimes, radiative forcing, or a combination of these and usually only at one location within the field. But simply the horizontal and vertical structure of TSFs makes this concept questionable, especially as these concepts do not account for advection. In other words, the local as well as non-local topography outside the investigated valley needs to be taken into account as even gentle topography induce submeso-scale motions. Any point observations should be put into the context of their surrounding topography and potentially induced motions instead of only accounting for vertical forcings. So far many submeso scale motions were detected, but their relation, interaction, and needed forcing is not well understood. Therefore, we recommend nested networks and FODS to further investigate submeso-scale motions vertically as well as horizontally as described in Section 3.3.4. Similarly, classification schemes and modeling studies at least need to incorporate the impacts of topography as well as horizontal advection. We finally conclude that we actually need to change from classification schemes using vertical forcing mechanism and focus on the relation between motions on multiple scales to understand turbulence within the nocturnal boundary layer.

References

- Acevedo OC, Costa FD, Oliveira PES, Puhales FS, Degrazia GA, Roberti DR (2014) The Influence of Submeso Processes on Stable Boundary Layer Similarity Relationships. *Journal of the Atmospheric Sciences* 71(1):207–225, DOI 10.1175/JAS-D-13-0131.1
- Acevedo OC, Mahrt L, Puhales FS, Costa FD, Medeiros LE, Degrazia GA (2016) Contrasting structures between the decoupled and coupled states of the stable boundary layer. *Quarterly Journal of the Royal Meteorological Society* 142(695):693–702, DOI 10.1002/qj.2693
- Acevedo OC, Maroneze R, Costa FD, Puhales FS, Degrazia GA, Nogueira Martins LG, Soares de Oliveira PE, Mortarini L (2019) The nocturnal boundary layer transition from weakly to very stable. Part I: Observations. *Quarterly Journal of the Royal Meteorological Society* 145(725):3577–3592, DOI 10.1002/qj.3642
- Anfossi D, Oetl D, Degrazia G, Goulart A (2005) An Analysis Of Sonic Anemometer Observations In Low Wind Speed Conditions. *Boundary-Layer Meteorology* 114(1):179–203, DOI 10.1007/s10546-004-1984-4
- Baas P, Bosveld FC, Baltink HK, Holtslag AAM (2009) A climatology of nocturnal low-level jets at Cabauw. *Journal of Applied Meteorology and Climatology* 48(8):1627–1642, DOI 10.1175/2009JAMC1965.1
- Baas P, van de Wiel BJH, van der Linden SJA, Bosveld FC (2018) From Near-Neutral to Strongly Stratified: Adequately Modelling the Clear-Sky Nocturnal Boundary Layer at Cabauw. *Boundary-Layer Meteorology* 166(2):217–238, DOI 10.1007/s10546-017-0304-8
- Banta RM, Shepson PB, Bottenheim J, Anlauf KG, Wiebe H, Gallant A, Biesenthal T, Olivier LD, Zhu CJ, McKendry IG, Steyn DG (1997) Nocturnal cleansing flows in a tributary valley. *Atmospheric Environment* 31(14):2147–2162, DOI 10.1016/S1352-2310(96)00359-7
- Basu S, Holtslag AAM, Van De Wiel BJH, Moene AF, Steeneveld GJJ, Wiel BJ, Moene AF, Steeneveld GJJ (2008) An inconvenient “truth” about using sensible heat flux as a surface boundary condition in models under stably stratified regimes. *Acta Geophysica* 56(1):88–99, DOI 10.2478/s11600-007-0038-y
- Bodine D, Klein PM, Arms SC, Shapiro A (2009) Variability of Surface Air Temperature over Gently Sloped Terrain. *Journal of Applied Meteorology and Climatology* 48(6):1117–1141, DOI 10.1175/2009JAMC1933.1
- Brotzge JA, Crawford KC (2000) Estimating Sensible Heat Flux from the Oklahoma Mesonet. *Journal of Applied Meteorology* 39(1):102–116, DOI 10.1175/1520-0450(2000)039<0102:ESHFFT>2.0.CO;2
- Caughey SJ, Palmer SG (1979) Some aspects of turbulence structure through the depth of the convective boundary layer. *Quarterly Journal of the Royal Meteorological Society* 105(446):811–827, DOI 10.1002/qj.49710544606

- Cava D, Mortarini L, Anfossi D, Giostra U (2019a) Interaction of Submeso Motions in the Antarctic Stable Boundary Layer. *Boundary-Layer Meteorology* 171(2):151–173, DOI 10.1007/s10546-019-00426-7
- Cava D, Mortarini L, Giostra U, Acevedo O, Katul G (2019b) Submeso Motions and Intermittent Turbulence Across a Nocturnal Low-Level Jet: A Self-Organized Criticality Analogy. *Boundary-Layer Meteorology* 172(1):17–43, DOI 10.1007/s10546-019-00441-8
- Cheng Y, Sayde C, Li Q, Basara J, Selker J, Tanner E, Gentine P (2017) Failure of Taylor’s hypothesis in the atmospheric surface layer and its correction for eddy-covariance measurements. *Geophysical Research Letters* 44(9):4287–4295, DOI 10.1002/2017GL073499
- Clements CB, Whiteman CD, Horel JD (2003) Cold-air-pool structure and evolution in a mountain basin : Peter Sinks , Utah. *J Appl Meteorol* 42(6):752–768
- Derbyshire SH (1999) Stable Boundary-Layer Modelling: Established Approaches and Beyond. *Boundary-Layer Meteorology* 90(3):423–446, DOI 10.1023/A:1001749007836
- Edwards JM (2009) Radiative Processes in the Stable Boundary Layer: Part II. The Development of the Nocturnal Boundary Layer. *Boundary-Layer Meteorology* 131(2):127–146, DOI 10.1007/s10546-009-9363-9
- Foken T (2017) Flux-Gradient Similarity. In: Foken T (ed) *Micrometeorology*, second edn, Springer Berlin Heidelberg, Berlin, Heidelberg, chap 2.3, pp 46–64, DOI 10.1007/978-3-642-25440-6
- Freire LS, Chamecki M, Bou-Zeid E, Dias NL (2019) Critical flux Richardson number for Kolmogorov turbulence enabled by TKE transport. *Quarterly Journal of the Royal Meteorological Society* 145(721):1551–1558, DOI 10.1002/qj.3511
- Galperin B, Sukoriansky S, Anderson PS (2007) On the critical Richardson number in stably stratified turbulence. *Atmospheric Science Letters* 8(3):65–69, DOI 10.1002/asl.153
- Geiss A, Mahrt L (2015) Decomposition of Spatial Structure of Nocturnal Flow over Gentle Terrain. *Boundary-Layer Meteorology* 156(3):337–347, DOI 10.1007/s10546-015-0043-7
- Goulden ML, Miller SD, da Rocha HR (2006) Nocturnal cold air drainage and pooling in a tropical forest. *J Geophys Res Atmos* 111(8):1–14, DOI 10.1029/2005JD006037
- Grudzielanek AM, Cermak J (2018) Temporal Patterns and Vertical Temperature Gradients in Micro-Scale Drainage Flow Observed Using Thermal Imaging. *Atmosphere* 9(12):498, DOI 10.3390/atmos9120498
- Holtslag AA, Svensson G, Baas P, Basu S, Beare B, Beljaars AC, Bosveld FC, Cuxart J, Lindvall J, Steeneveld GJ, Tjernström M, Van De Wiel BJ (2013) Stable atmospheric boundary layers and diurnal cycles: Challenges for weather and climate models. *Bulletin of the American Meteorological Society* 94(11):1691–1706, DOI 10.1175/BAMS-D-11-00187.1

- Holtzlag AAM, De Bruin HAR (1988) Applied Modeling of the Nighttime Surface Energy Balance over Land. *Journal of Applied Meteorology* 27(6):689–704, DOI 10.1175/1520-0450(1988)027<0689:AMOTNS>2.0.CO;2
- Holtzlag AAM, Nieuwstadt FTM (1986) Scaling the atmospheric boundary layer. *Boundary-Layer Meteorology* 36(1-2):201–209, DOI 10.1007/BF00117468
- Holtzlag AAM, Van Meijgaard E, De Rooy WC (1995) A comparison of boundary layer diffusion schemes in unstable conditions over land. *Boundary-Layer Meteorology* 76(1-2):69–95, DOI 10.1007/BF00710891
- van Hooijdonk IGS, Donda JMM, Clercx HJH, Bosveld FC, van de Wiel BJH (2015) Shear Capacity as Prognostic for Nocturnal Boundary Layer Regimes. *Journal of the Atmospheric Sciences* 72(4):1518–1532, DOI 10.1175/JAS-D-14-0140.1
- Hoover JD, Stauffer DR, Richardson SJ, Mahrt L, Gaudet BJ, Suarez A (2015) Sub-meso motions within the stable boundary layer and their relationships to local indicators and synoptic regime in moderately complex terrain. *Journal of Applied Meteorology and Climatology* 54(2):352–369, DOI 10.1175/JAMC-D-14-0128.1
- Izett JG, van de Wiel BJ, Baas P, Bosveld FC (2018) Understanding and Reducing False Alarms in Observational Fog Prediction. *Boundary-Layer Meteorology* 169(2):347–372, DOI 10.1007/s10546-018-0374-2
- Kaimal JC, Wyngaard JC, Haugen DA, Coté OR, Izumi Y, Caughey SJ, Readings CJ (1976) Turbulence Structure in the Convective Boundary Layer. *Journal of the Atmospheric Sciences* 33(11):2152–2169, DOI 10.1175/1520-0469(1976)033<2152:TSITCB>2.0.CO;2
- Kang Y, Belušić D, Smith-Miles K (2015) Classes of structures in the stable atmospheric boundary layer. *Quarterly Journal of the Royal Meteorological Society* 141(691):2057–2069, DOI 10.1002/qj.2501
- Keller CA, Huwald H, Vollmer MK, Wenger A, Hill M, Parlange MB, Reimann S (2011) Fiber optic distributed temperature sensing for the determination of the nocturnal atmospheric boundary layer height. *Atmospheric Measurement Techniques* 4(2):143–149, DOI 10.5194/amt-4-143-2011
- Kuttler W, Barlag AB, Roßmann F (1996) Study of the thermal structure of a town in a narrow valley. *Atmos Environ* 30(3):365–378
- Lang F, Belušić D, Siems S (2018) Observations of Wind-Direction Variability in the Nocturnal Boundary Layer. *Boundary-Layer Meteorology* 166(1):51–68, DOI 10.1007/s10546-017-0296-4
- Lapo K, Nijssen B, Lundquist JD (2019) Evaluation of Turbulence Stability Schemes of Land Models for Stable Conditions. *Journal of Geophysical Research: Atmospheres* 124(6):3072–3089, DOI 10.1029/2018JD028970
- Lareau NP, Crosman E, Whiteman CD, Horel JD, Hoch SW, Brown WOJ, Horst TW (2013) The persistent cold-air pool study. *Bull Am Meteorol Soc* 94(1):51–63, DOI 10.1175/BAMS-D-11-00255.1
- Lenschow DH, Stankov BB (1986) Length Scales in the Convective Boundary Layer. *Journal of the Atmospheric Sciences* 43(12):1198–1209, DOI 10.1175/1520-0469(1986)043<1198:LSITCB>2.0.CO;2

- van der Linden SJA, Baas P, Antoon van Hooft J, van Hooijdonk IGS, Bosveld FC, van de Wiel BJH (2017) Local Characteristics of the Nocturnal Boundary Layer in Response to External Pressure Forcing. *Journal of Applied Meteorology and Climatology* 56(11):3035–3047, DOI 10.1175/JAMC-D-17-0011.1
- Louis JF (1979) A parametric model of vertical eddy fluxes in the atmosphere. *Boundary-Layer Meteorology* 17(2):187–202, DOI 10.1007/BF00117978
- Luo Z, Asproudi C (2015) Subsurface urban heat island and its effects on horizontal ground-source heat pump potential under climate change. *Appl Therm Eng* 90:530–537, DOI 10.1016/j.applthermaleng.2015.07.025
- Mahrt L (1998) Nocturnal Boundary-Layer Regimes. *Boundary-Layer Meteorology* 88(2):255–278, DOI 10.1023/A:1001171313493
- Mahrt L (2007) Weak-wind mesoscale meandering in the nocturnal boundary layer. *Environmental Fluid Mechanics* 7(4):331–347, DOI 10.1007/s10652-007-9024-9
- Mahrt L (2009) Variability and maintenance of turbulence in the very stable boundary layer. *Boundary-Layer Meteorol* 135(1):1–18, DOI 10.1007/s10546-009-9463-6
- Mahrt L (2017a) Directional Shear in the Nocturnal Atmospheric Surface Layer. *Boundary-Layer Meteorology* 165(1):1–7, DOI 10.1007/s10546-017-0270-1
- Mahrt L (2017b) Lee Mixing and Nocturnal Structure over Gentle Topography. *Journal of the Atmospheric Sciences* 74(6):1989–1999, DOI 10.1175/JAS-D-16-0338.1
- Mahrt L (2017c) Stably Stratified Flow in a Shallow Valley. *Boundary-Layer Meteorology* 162(1):1–20, DOI 10.1007/s10546-016-0191-4
- Mahrt L (2019) Microfronts in the nocturnal boundary layer. *Quarterly Journal of the Royal Meteorological Society* 145(719):546–562, DOI 10.1002/qj.3451
- Mahrt L (2020) Time–space variations of temperature in the nocturnal boundary layer. *Quarterly Journal of the Royal Meteorological Society* 146(731):2756–2767, DOI 10.1002/qj.3815
- Mahrt L, Heald R (2015) Common Marginal Cold Pools. *Journal of Applied Meteorology and Climatology* 54(2):339–351, DOI 10.1175/JAMC-D-14-0204.1
- Mahrt L, Thomas CK (2016) Surface Stress with Non-stationary Weak Winds and Stable Stratification. *Boundary-Layer Meteorology* 159(1):3–21, DOI 10.1007/s10546-015-0111-z
- Mahrt L, Thomas C, Richardson S, Seaman N, Stauffer D, Zeeman M (2013) Non-stationary Generation of Weak Turbulence for Very Stable and Weak-Wind Conditions. *Boundary-Layer Meteorology* 147(2):179–199, DOI 10.1007/s10546-012-9782-x
- Mahrt L, Richardson S, Stauffer D, Seaman N (2014a) Nocturnal wind-directional shear in complex terrain. *Quarterly Journal of the Royal Meteorological Society* 140(685):2393–2400, DOI 10.1002/qj.2369
- Mahrt L, Sun J, Oncley SP, Horst TW (2014b) Transient Cold Air Drainage down a Shallow Valley. *Journal of the Atmospheric Sciences* 71(7):2534–2544, DOI 10.1175/JAS-D-14-0010.1

- Mahrt L, Pfister L, Thomas CK (2020) Small-Scale Variability in the Nocturnal Boundary Layer. *Boundary-Layer Meteorology* 174(1):81–98, DOI 10.1007/s10546-019-00476-x
- Maroneze R, Acevedo OC, Costa FD, Puhales FS, Demarco G, Mortarini L (2019) The nocturnal boundary layer transition from weakly to very stable. Part II: Numerical simulation with a second-order model. *Quarterly Journal of the Royal Meteorological Society* 145(725):3593–3608, DOI 10.1002/qj.3643
- Meybeck M, Green P, Vörösmarty C (2001) A New Typology for Mountains and Other Relief Classes. *Mountain Research and Development* 21(1):34–45, DOI 10.1659/0276-4741(2001)021[0034:ANTFMA]2.0.CO;2
- Monahan AH, Rees T, He Y, McFarlane N (2015) Multiple Regimes of Wind, Stratification, and Turbulence in the Stable Boundary Layer. *Journal of the Atmospheric Sciences* 72(8):3178–3198, DOI 10.1175/JAS-D-14-0311.1
- Monti P, Fernando HJS, Princevac M, Chan WC, Kowalewski TA, Pardyjak ER (2002) Observations of Flow and Turbulence in the Nocturnal Boundary Layer over a Slope. *Journal of the Atmospheric Sciences* 59(17):2513–2534, DOI 10.1175/1520-0469(2002)059<2513:OOFATI>2.0.CO;2
- Mortarini L, Stefanello M, Degrazia G, Roberti D, Trini S, Domenico C (2016) Characterization of Wind Meandering in Low-Wind-Speed Conditions. *Boundary-Layer Meteorology* 161(1):165–182, DOI 10.1007/s10546-016-0165-6
- Mortarini L, Cava D, Giostra U, Acevedo O, Nogueira Martins LG, Soares de Oliveira PE, Anfossi D (2017) Observations of submeso motions and intermittent turbulent mixing across a low level jet with a 132-m tower. *Quarterly Journal of the Royal Meteorological Society* 144(710):172–183
- Mortarini L, Cava D, Giostra U, Costa FD, Degrazia G, Anfossi D, Acevedo O (2019) Horizontal Meandering as a Distinctive Feature of the Stable Boundary Layer. *Journal of the Atmospheric Sciences* 76(10):3029–3046, DOI 10.1175/JAS-D-18-0280.1
- Müller MD, Masbou M, Bott A (2010) Three-dimensional fog forecasting in complex terrain. *Quarterly Journal of the Royal Meteorological Society* 136(653):2189–2202, DOI 10.1002/qj.705
- Nappo CJ (1991) Sporadic breakdowns of stability in the PBL over simple and complex terrain. *Boundary-Layer Meteorology* 54(1-2):69–87, DOI 10.1007/BF00119413
- Oke TR (1982) The energetic basis of the urban heat island. *Quarterly Journal of the Royal Meteorological Society* 108(455):1–24, DOI 10.1002/qj.49710845502
- Pfister L, Sigmund A, Olesch J, Thomas CK (2017) Nocturnal Near-Surface Temperature, but not Flow Dynamics, can be Predicted by Microtopography in a Mid-Range Mountain Valley. *Boundary-Layer Meteorology* 165(2):333–348, DOI 10.1007/s10546-017-0281-y
- Pfister L, Lapo K, Sayde C, Selker J, Mahrt L, Thomas CK (2019) Classifying the nocturnal atmospheric boundary layer into temperature and flow regimes. *Quarterly Journal of the Royal Meteorological Society* 145(721):1515–1534, DOI 10.1002/qj.3508

- Sayde C, Thomas CK, Wagner J, Selker J (2015) High-resolution wind speed measurements using actively heated fiber optics. *Geophys Res Lett* 42(22):10,064–10,073, DOI 10.1002/2015GL066729
- Siebesma AP, Soares PMM, Teixeira J (2007) A Combined Eddy-Diffusivity Mass-Flux Approach for the Convective Boundary Layer. *Journal of the Atmospheric Sciences* 64(4):1230–1248, DOI 10.1175/JAS3888.1
- Sigmund A, Pfister L, Sayde C, Thomas CK (2017) Quantitative analysis of the radiation error for aerial coiled-fiber-optic distributed temperature sensing deployments using reinforcing fabric as support structure. *Atmospheric Measurement Techniques* 10(6):2149–2162, DOI 10.5194/amt-10-2149-2017
- Steenefeld GJ, van de Wiel BJH, Holtslag AAM (2006) Modeling the Evolution of the Atmospheric Boundary Layer Coupled to the Land Surface for Three Contrasting Nights in CASES-99. *Journal of the Atmospheric Sciences* 63(3):920–935, DOI 10.1175/JAS3654.1
- Stefanello M, Cava D, Giostra U, Acevedo O, Degrazia G, Anfossi D, Mortarini L (2020) Influence of submeso motions on scalar oscillations and surface energy balance. *Quarterly Journal of the Royal Meteorological Society* 146(727):889–903, DOI 10.1002/qj.3714
- Sun J, Mahrt L, Banta RM, Pichugina YL (2012) Turbulence Regimes and Turbulence Intermittency in the Stable Boundary Layer during CASES-99. *Journal of the Atmospheric Sciences* 69(1):338–351, DOI 10.1175/JAS-D-11-082.1
- Sun J, Mahrt L, Nappo C, Lenschow DH (2015) Wind and Temperature Oscillations Generated by Wave–Turbulence Interactions in the Stably Stratified Boundary Layer. *Journal of the Atmospheric Sciences* 72(4):1484–1503, DOI 10.1175/JAS-D-14-0129.1
- Sun J, Lenschow DH, LeMone MA, Mahrt L (2016) The Role of Large-Coherent-Eddy Transport in the Atmospheric Surface Layer Based on CASES-99 Observations. *Boundary-Layer Meteorology* 160(1):83–111, DOI 10.1007/s10546-016-0134-0
- Sun J, Takle ES, Acevedo OC (2020) Understanding Physical Processes Represented by the Monin–Obukhov Bulk Formula for Momentum Transfer. *Boundary-Layer Meteorology* 177(1):69–95, DOI 10.1007/s10546-020-00546-5
- Thomas CK (2011) Variability of Sub-Canopy Flow, Temperature, and Horizontal Advection in Moderately Complex Terrain. *Boundary-Layer Meteorology* 139(1):61–81, DOI 10.1007/s10546-010-9578-9
- Thomas CK, Kennedy AM, Selker JS, Moretti A, Schroth MH, Smoot AR, Tufillaro NB, Zeeman MJ (2012) High-Resolution Fibre-Optic Temperature Sensing: A New Tool to Study the Two-Dimensional Structure of Atmospheric Surface-Layer Flow. *Boundary-Layer Meteorology* 142(2):177–192, DOI 10.1007/s10546-011-9672-7
- Van de Wiel BJH, Moene AF, Jonker HJJ, Baas P, Basu S, Donda JMM, Sun J, Holtslag AAM (2012) The Minimum Wind Speed for Sustainable Turbulence in the Nocturnal Boundary Layer. *Journal of the Atmospheric Sciences* 69(11):3116–3127, DOI 10.1175/JAS-D-12-0107.1

- Van de Wiel BJH, Vignon E, Baas P, van Hooijdonk IGS, van der Linden SJA, Antoon van Hooft J, Bosveld FC, de Roode SR, Moene AF, Genthon C (2017) Regime Transitions in Near-Surface Temperature Inversions: A Conceptual Model. *Journal of the Atmospheric Sciences* 74(4):1057–1073, DOI 10.1175/JAS-D-16-0180.1
- Vercauteren N, Klein R (2015) A Clustering Method to Characterize Intermittent Bursts of Turbulence and Interaction with Submesoscale Motions in the Stable Boundary Layer. *Journal of the Atmospheric Sciences* 72(4):1504–1517, DOI 10.1175/JAS-D-14-0115.1
- Vercauteren N, Mahrt L, Klein R (2016) Investigation of interactions between scales of motion in the stable boundary layer. *Quarterly Journal of the Royal Meteorological Society* 142(699):2424–2433, DOI 10.1002/qj.2835
- Vercauteren N, Boyko V, Faranda D, Stiperski I (2019) Scale interactions and anisotropy in stable boundary layers. *Quarterly Journal of the Royal Meteorological Society* 145(722):1799–1813, DOI 10.1002/qj.3524
- Wallace JM, Hobbs PV (2006) The Atmospheric Boundary Layer. In: *Atmospheric science: An introductory survey*, 2nd edn, Elsevier, chap 9, p 375ff
- Zeeman MJ, Selker JS, Thomas CK (2015) Near-Surface Motion in the Nocturnal, Stable Boundary Layer Observed with Fibre-Optic Distributed Temperature Sensing. *Boundary-Layer Meteorology* 154(2):189–205, DOI 10.1007/s10546-014-9972-9

Individual Contributions to the joint Publications

The publications of this cumulative thesis were composed in close cooperation with other researchers. Hence, many authors contributed to the publications listed in Appendices A to D in many different ways. This section specifies my own contributions to the individual manuscripts. First named author was always the corresponding author.

All publications used the data of the Shallow Cold Pool experiment (Sect. 2). This experiment was conducted before I started my PhD, hence, I did not contribute to the experiment itself. The experiment was mainly designed by Larry Mahrt, Christoph Thomas, John Selker, and Chadi Sayde, while the maintenance and data collection of fiber-optic distributed sensing (FODS) was mainly done by Christoph Thomas and Chadi Sayde. Data of the remaining network was collected by the Earth Observing Laboratory of the National Center for Atmospheric Research. For further information on the funding of the experiment and my doctoral thesis please refer to page iii. For data analysis of ultrasonic anemometer I used some tools developed by Christoph K. Thomas (CKT) and Chadi Sayde (CS): 1) FODS calibration and wind speed calculation (CS); 2) The bmmflux-software to computed fluxes, FFT spectra, third order, and second order moments (CKT); 3) The multiresolution decomposition tool for analysis in Appendix A (CKT). I reprocessed all FODS data with the tool from CS and adjusted it to compute the wind speed of each level of the fiber-optic transect automatically. I also adjusted the bmmflux-tool from CKT to process data of multiple stations by itself.

Appendix A: Classifying the nocturnal atmospheric boundary layer into temperature and flow regimes

Authors: Lena Pfister, Karl Lapo, Chadi Sayde, John Selker, Larry Mahrt, Christoph K. Thomas

Status: Accepted and published by the Quarterly Journal of the Royal Meteorological Society

Own contribution: processing data 100%, data analyses and figures 100%, discussion of results 65%, manuscript writing 70%

LP processed FODS and ultrasonic anemometer data and analyzed the data in close discussion with mostly CKT but also LM. CS and JS introduced me to the data set and helped with initial analysis of the FODS data. LP put special effort in the research of longwave radiative forcing, spatial evaluation of turbulence, and the analysis of the multiresolution decomposition (MRD). LP was introduced to and got help for the MRD by CKT especially in terms of interpreting MRDs. All figures and tables were created by LP. LP, CKT, LM, and KL interpreted and discussed results. KL was mostly involved in the discussion about radiative forcing. Revision and rewriting of the manuscript was done by LP and CKT.

Appendix B: Small-Scale Variability in the Nocturnal Boundary Layer

Authors: Larry Mahrt, Lena Pfister, Christoph K. Thomas

Status: Accepted and published by Boundary-Layer Meteorology

Own contribution: processing data 5%, data analyses and figures 5%, discussion of results 5%, manuscript writing 0%

LP processed FODS data and created several plots for LM upon request for further investigation. Figure 9 and 10 of this publication was created by LP, while all other figures were created by LM. LM, LP, and CKT interpreted and discussed results. LP was especially involved in the discussion of Section 5. Revision and writing of the manuscript was done by LM.

Appendix C: Thermal Submeso-Scale Motions in the Nocturnal Stable Boundary Layer - Part 1: Detection & Mean Statistics

Authors: Lena Pfister, Karl Lapo, Larry Mahrt, Christoph K. Thomas

Status: Provisionally accepted by Boundary-Layer Meteorology

Own contribution: processing data 100%, data analyses and figures 100%, discussion of results 80%, manuscript writing 95%

LP processed FODS and ultrasonic anemometer data and analyzed the data in discussion with mostly CKT and KL but also LM. LP developed the detection algorithm in discussion with CKT. The investigation of TSFs on field-site scale was the idea of LP which also did all corresponding analysis and design of the plots. CKT gave the idea of conditional averaging depending on a relative distance to the TSF boundary. Further analysis based on conditional averaging was initialized by LP and then discussed with all co-authors. All figures and tables were created by LP. LP, KL, CKT, and LM interpreted and discussed results. Revision and rewriting of the manuscript was done by LP and CKT.

Appendix D: Thermal Submeso-Scale Motions in the Nocturnal Stable Boundary Layer - Part 2: Generating Mechanisms & Implications

Authors: Lena Pfister, Karl Lapo, Larry Mahrt, Christoph K. Thomas

Status: Under review by Boundary-Layer Meteorology

Own contribution: processing data 100%, data analyses and figures 100%, discussion of results 90%, manuscript writing 95%

LP processed FODS and ultrasonic anemometer data and analyzed the data in discussion with mostly CKT and KL but also LM. CKT gave the idea of using third and second order moments to investigate the vertical structure. LP was introduced to this technique by CKT. All other analysis and interpretation was done by LP and then mainly discussed with KL and CKT but also LM. LP put special efforts to investigate the relation between TSFs and the wind regime as well as stability regimes. Revision and rewriting of the manuscript was done by LP and CKT.

A Classifying the Nocturnal Atmospheric Boundary Layer into Temperature and Flow Regimes







Received: 12 June 2018 | Revised: 14 February 2019 | Accepted: 16 February 2019 | Published on: 16 April 2019

DOI: 10.1002/qj.3508

RESEARCH ARTICLE

Quarterly Journal of the
Royal Meteorological Society 

Classifying the nocturnal atmospheric boundary layer into temperature and flow regimes

Lena Pfister¹  | Karl Lapo^{1,2}  | Chadi Sayde³  | John Selker⁴  | Larry Mahrt⁵  |
Christoph K. Thomas^{1,2} 

¹Micrometeorology Group, University of Bayreuth, Germany²Bayreuth Center of Ecology and Environmental Research, University of Bayreuth, Germany³Department of Biological and Agricultural Engineering, North Carolina State University, Raleigh, North Carolina, USA⁴Department of Biological and Ecological Engineering, Oregon State University, Corvallis, Oregon, USA⁵NorthWest Research Associates, Corvallis, Oregon, USA**Correspondence**

Lena Pfister, Micrometeorology, University of Bayreuth, 95440 Bayreuth, Germany.
Email: lena.pfister@uni-bayreuth.de

Funding information

Army Research Office (contracts W911NF-10-1-0361 and W911NF-09-1-0271) and the National Science Foundation (AGS-1115011, AGS-1614345 and AGS-0955444)

We propose a classification scheme for nocturnal atmospheric boundary layers and apply it to investigate the spatio-temporal structure of air temperature and wind speed in a shallow valley during the Shallow Cold Pool Experiment. This field campaign was the first to collect spatially continuous temperature and wind information at high resolution (1 s, 0.25 m) using the distributed temperature sensing technique across a 220 m long transect at three heights (0.5, 1.0, 2.0 m). The night-time classification scheme was motivated by a surface energy balance and used a combination of static stability, wind regime and longwave radiative forcing as quantities to determine physically meaningful boundary-layer regimes. Out of all potential combinations of these three quantities, 14 night-time classes contained observations, of which we selected three for detailed analysis and comparison.

The three classes represent a transition from mechanical to radiative forcing. The first night class represents conditions with strong dynamic forcing caused by locally induced lee turbulence dominating near-surface temperatures across the shallow valley. The second night class was a concurrence of enhanced dynamic mixing due to significant winds at the valley shoulders and cold-air pooling at the bottom of the shallow valley as a result of strong radiative cooling. The third night class was characteristic of weak winds eliminating the impact of mechanical mixing but emphasizing the formation and pooling of cold air at the valley bottom.

The proposed night-time classification scheme was found to sort the experimental data into physically meaningful regimes of surface flow and transport. It is suitable to stratify short- and long-term experimental data for ensemble averaging and to identify case studies.

KEYWORDS

classification, distributed temperature sensing, nocturnal near-surface temperatures, radiative forcing, stable boundary layer, topography, Taylor's hypothesis

1 | INTRODUCTION

The nocturnal boundary layer offers a variety of temperature and flow regimes, which are subject to motions of local and non-local origin. A nocturnal classification scheme based upon physically meaningful parameters for the formation of boundary layers can be a useful tool to stratify observations and model output in order to extract general features of the strength and mechanisms for atmospheric transport and mixing.

Several approaches for defining regimes have been proposed using local or internal boundary-layer parameters. Holtslag and Nieuwstadt (1986) proposed different scaling regimes for the unstable and the stable atmospheric boundary layer assuming the validity of the Monin–Obukhov similarity theory. Each scaling regime is determined by z/h and h/L with h being the mixing height, L the Obukhov length, z the reference height. However, the definition of a mixing height during very stable conditions is controversial and difficult as increasing stability limits vertical fluxes and eddies

may become disconnected from the surface (e.g. Derbyshire, 1999; Sun *et al.*, 2012).

The most commonly used concept to determine physically meaningful boundary layers was developed by Mahrt (1998). Here, the boundary layer is also defined by the local parameter z/L , but regimes are stratified into a weakly stable boundary layer (wSBL), a transition regime, and the very stable boundary (vSBL). However, z/L is height- and site-dependent, hence no universal threshold value can be given. Note that z/L is a local stability parameter and thus does not contain information about the global state of the larger-scale boundary layer. Especially in the stable boundary layer, a single non-dimensional combination such as z/L , or also the bulk Richardson number Ri_b , is insufficient to determine boundary-layer regimes. For example, during cold-air drainage, surface-layer similarity theory is violated, invalidating the use of z/L and Ri_b (e.g. Mahrt *et al.*, 2014a, 2014b, 2015, Mahrt, 2017b).

Another approach based upon an internal parameter is to use wind regimes separated by a threshold wind speed. Sun *et al.* (2012, 2015) developed the so-called ‘Hockey-Stick Transition’ wind speed for near-surface values. However, wind regimes only address mechanical forcing of the boundary layer and hence neglect radiative and buoyancy forcing.

Following the study of Sun *et al.* (2012), Mahrt *et al.* (2015) used the combination of wind regimes and stability classes. They found that the threshold value determining the wind regimes increases for increasing stability. Further, for vanishing wind speeds, the influence of static stability on turbulence vanishes since shear instability is the dominant mechanism generating turbulence under these conditions, while the buoyancy-driven destruction of turbulence responds on longer time-scales, which was also found by Sun *et al.* (2012).

To separate a decoupled from a coupled SBL, Acevedo *et al.* (2016) determined a threshold wind speed at which the average vertical gradient of the turbulent kinetic energy switches sign at all observational levels. For wind speeds higher than this threshold, a coupled SBL is expected. Accordingly, the threshold wind speed of Sun *et al.* (2012) determines locally if the eddies communicate with the surface, while the threshold wind speed of Acevedo *et al.* (2016) is an indication for the vertical communication of exchange across the entire surface layer. However, the method of Acevedo *et al.* (2016) requires turbulence observations at multiple levels to capture the complete surface layer, which are not available for most field campaigns.

Others have attempted to use parameters external to the boundary layer, i.e. those not affected by the surface, to determine boundary-layer regimes. Van de Wiel *et al.* (2012) proposed using a minimum geostrophic wind speed needed to sustain near-surface turbulence. In their study, geostrophic wind speed was determined by surface pressure observations from eight synoptic stations in a radius of 75 km around a tower. Similarly, van Hooijdonk *et al.* (2015) used the wSBL and vSBL concept and showed that both regimes are well

characterized by the so-called ‘shear capacity’ defined as the critical wind speed necessary to sustain enough turbulence to balance the radiative cooling. van der Linden *et al.* (2017) refined this approach and proposed using bin averages of the ambient geostrophic wind determined by horizontal pressure gradients. For their observations, ensemble averages of the net radiation, friction velocity and turbulent heat flux organized surprisingly well when binned using the geostrophic wind speed. This scheme was also used by Baas *et al.* (2018) leading to good model results when modelling the stable boundary layer. However, measurements of the geostrophic wind speed are not easily obtained for most campaigns and the communication of eddies across the tower layer remains difficult to determine.

Other studies such as Edwards (2009) reveal the importance of radiative forcings for the boundary layer. For example, the turbulent temperature scale is related to cloud cover (Holt-slag and De Bruin, 1988), and cloud cover in concert with the geostrophic wind speed impacts the boundary layer (Monahan *et al.*, 2015).

Here, we propose a classification scheme for the nocturnal boundary layer which combines the effects of buoyancy, mechanical and radiative forcing on surface turbulence and flow. Our goal was to develop a simple, but effective and generally applicable night classification scheme based upon the three forcing variables static stability, wind regime, and long-wave radiative forcing (cf. section 2.2).

Since most of the Earth’s surface is characterized by gentle, less structured terrain of small spatial scale (Meybeck *et al.*, 2001), we chose observations from the Shallow Cold Pool (SCP) experiment over a semi-arid grassland in the Great Plains in northeast Colorado, USA to test our classification scheme. As a novelty, SCP featured measurements from the actively heated distributed temperature sensing (DTS) technique to obtain near-surface temperatures and wind speeds at a high spatial (0.25 m) and temporal (5 s) resolution. The DTS technique is an excellent tool for studying the nocturnal boundary layer due to spatially continuous measurements (Thomas *et al.*, 2012; Sayde *et al.*, 2015; Zeeman *et al.*, 2015; Pfister *et al.*, 2017) complementing surface networks of classical eddy covariance stations. Near-surface observations were taken by DTS at three levels up to 2 m above ground level (agl). For the first time, the use of actively heated DTS yielding simultaneous wind speed and temperature observations allowed the investigation of the spatial variability of Ri_b and thus the representativeness of point observations from conventional sensors.

In the first part of the paper, the theoretical background of averaging operators and the definition of the night classification scheme are presented (section 2), followed by a description of the SCP field site (section 3.1). Input variables of our night classification scheme are listed in section 3.2 and their impact on spatio-temporal temperature perturbations and Ri_b are analyzed in sections 4.1–4.3. In the second part of the paper, we evaluate the night classification scheme for defining

a physically meaningful boundary layer by comparing three night classes (section 4.4) and discuss their impact on surface transport and flow as observed by the DTS technique and tower measurements (section 4.5).

2 | THEORETICAL BACKGROUND

2.1 | Averaging operators and basic variables

Reynolds decomposition was used to divide an arbitrary variable ϕ into a mean and a fluctuating component. For our study ϕ was the near-surface temperature θ and wind speed u . Unweighted averages were computed on a temporal scale of 5 min which includes all of the turbulent scales even for more windy conditions (Mahrt *et al.*, 2014b). There is a chance that perturbations at the 5 min scale are contaminated by non-turbulent motions for very stable stratification. However, similar to Mahrt *et al.* (2014b) we decided to not choose a stratification-dependent averaging time-scale, as 5 min averages suitably captured boundary-layer motions and 1 min averages did not create significant differences in the results. Additionally, the temporal resolution of the radiation data was 5 min, which limited the ability of this study to analyze dynamics at finer resolution. Spatial averages, $\langle \phi \rangle$, are computed over the horizontal scale of the full cross-valley transect (227.5 m for our field site) separately for each height. Hence, spatial perturbations represent spatial differences of ϕ within the chosen valley. Temporal perturbations are denoted by ϕ' and spatial perturbations by $\hat{\phi}$, whereas 5 min averages are denoted by $\bar{\phi}$:

$$\phi' = \phi - \bar{\phi}, \quad (1)$$

$$\hat{\phi} = \phi - \langle \phi \rangle. \quad (2)$$

The bulk Richardson number within our DTS transect was computed as

$$Ri_b = \frac{g}{\bar{\theta}} \frac{\Delta\theta/\Delta z}{(\Delta u/\Delta z)^2}, \quad (3)$$

with $\bar{\theta}$ being the mean temperature over the layer and $\Delta\theta/\Delta z$ and $\Delta u/\Delta z$ being the potential temperature and vertical wind speed gradients at each measurement point within the DTS transect. We decided to calculate bulk Ri_b instead of the gradient Ri_b as the DTS transect only consisted of three heights in the lowest 2 m of the boundary layer.

For comparing for example different wind regimes or night classes, we decided to compute the ensemble average $\langle \phi \rangle$ over all periods classified as the corresponding regime or class. $\langle Ri_b \rangle$ was calculated as the ensemble averages $\langle \bar{\theta} \rangle$, $\langle \Delta\theta/\Delta z \rangle$ and $\langle \Delta u/\Delta z \rangle$. Even though the concept of a critical Ri_b is questionable (Galperin *et al.*, 2007), we included a critical Ri_b of 0.25 in our analysis as a threshold between low and high turbulence in the boundary layer.

The spread of observations within each ensemble average will be presented by the standard error of the mean $SEM = \sigma_\phi/\sqrt{n}$, with σ_ϕ being the standard deviation of the

parameter ϕ and n the number of observations of ϕ . We chose the spatial mean of the SEM of each ensemble average to accurately compare ensemble averages with different numbers of flow observations to each other.

For discussing the validity of the night classification scheme, we analyzed the profiles of the wind speed and sensible heat flux (Q_H). We are using the commonly used sign convention with positive values showing an energy flux away from the surface and vice versa:

$$Q_H = c_p \rho \overline{w'T'}. \quad (4)$$

Multi-resolution decomposition (MRD) was performed for each case study to decompose the data into different dyadic time-scales (64 min, 32 min, 16 min, ..., 30 s), and the spatial two-point correlation coefficient $R_{\phi_{ij}}$ for each time-scale was computed as described in Thomas (2011) to evaluate spatial coherence of temperature and wind speed dynamics:

$$R_{\phi_{ij}}(d_{ij}) = \frac{\overline{\phi'_i \phi'_j}}{\sigma_{\phi_i} \sigma_{\phi_j}}, \quad (5)$$

where d_{ij} is the separation distance between a reference point i and a distant point j and σ was the standard deviation. $R_{\phi_{ij}}$ was computed for the temperature and wind speed DTS data at each time-scale. The southern end of the valley bottom was selected as reference point i . A negative d_{ij} indicated that the distant point j lay north of reference point i , while point j lay south for positive d_{ij} . This technique was introduced by Howell and Mahrt (1997) and later used e.g. by Mahrt *et al.* (2009) to determine the space-time structure of mesoscale motions in the stable boundary layer. $R_{\theta_{ij}}$ and $R_{u_{ij}}$ are measures for the spatial correlation of temperature and the wind directional shear does not refer to the spatial two-point correlation coefficients shear between two stations is given as the difference in direction of the two wind vectors.

2.2 | Night classification scheme

We assumed a simplified nocturnal surface energy balance only containing the most relevant budget components

$$-Q_s^* = Q_H + A_h \quad (6)$$

with Q_s^* being the net radiation balance, Q_H being the sensible heat flux and A_h being horizontal advection of heat by katabatic winds. The net radiation balance during the night is driven by the balance of the up- and downwelling long-wave radiation (L_\uparrow , L_\downarrow). However, L_\uparrow is a function of the surface temperature and thus may be regarded as near-surface response rather than a forcing. As a result, only downwelling long-wave radiative forcing (dLRF) was incorporated. The commonly used flux-gradient similarity theory (K-approach, e.g. Foken, 2017b) derives the sensible heat flux from the eddy diffusivity driven by the friction velocity and from the local temperature gradient. Accordingly, for our night classification scheme, the wind regime determined by friction velocity and wind speed is as important for the sensible

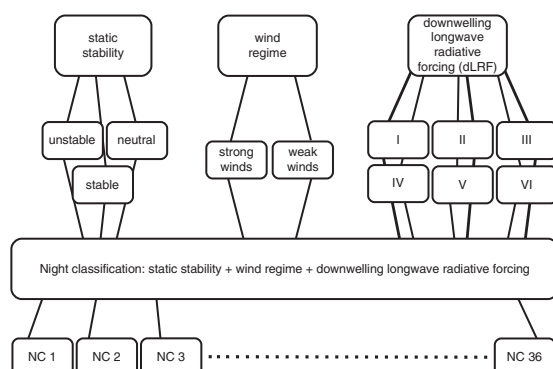


FIGURE 1 Flow chart of the night classification scheme

heat flux as the temperature gradient defining static stability. Finally, the topography of the field site is important as horizontal advection is driven by the horizontal temperature gradient and the katabatic wind, which is a function of the slope angle, the buoyancy and the cold-air layer temperature and height (Stull, 2000).

For our study we chose to neglect the latent heat flux, as the experiment was conducted above grassland during the winter with no snow cover during the period under investigation. To extend the night classification scheme to sites with frequent ground fog, a simple variable like dew point temperature or moisture classes could be added to our night classification scheme, which was not in the scope of this study.

The most important input variables for our night classification scheme are static stability (section 3.2.1), the wind regime (section 3.2.2) and the downwelling long-wave radiative forcing (section 3.2.3). The night classification scheme was derived by combining these input variables (Figure 1). We deliberately excluded topography from the list of input variables as topography cannot be described by a single universal parameter such as slope angle. Instead we discuss the

results in the context of the microtopography of the field site (Figures A1 and 2).

3 | MATERIAL AND METHODS

3.1 | Shallow Cold Pool experiment

The SCP experiment was conducted in northeast Colorado, USA, over semi-arid grassland at approximately 1,660 m above mean sea level from 1 October to 1 December 2012 (https://www.eol.ucar.edu/field_projects/scp; accessed 2 March 2019). Measurements with the distributed temperature sensing (DTS) technique (e.g. Selker *et al.*, 2006; Thomas *et al.*, 2012) were only conducted from 16 November until 27 November. For this study only nine nights without observational gaps from 1900 until 0500 the next day were analyzed, i.e. 1080 observations on a 5 min time-scale for each instrument (cf. Figure A2). A detailed description of the field site and all instrumentations can be found in Mahrt *et al.* (2014b).

The valley can be described as gentle terrain with a height difference of ≈ 27 m along a distance of ≈ 1.2 km resulting in an inclination of 1.4° (https://www.eol.ucar.edu/system/files/files/field_project/SCP/SCP-RIC.kmz). On average, the side slopes rise about 12 m over a horizontal distance of about 130 m. The width of the valley bottom averages about 5 m. A miniplateau on the north shoulder of the valley showed an inclination of $\approx 6.0^\circ$ for a distance of 110 m (cf. Figure A1). The provided link gives a full description of the microtopography of the field site. The DTS transect was set up as a cross-transect of the valley, which we refer to as a gully further on. The inclination of the north and south shoulder of the gully directly at the DTS transect got smoother with inclinations of 4.4° and 3.9° (Figure 2). Inclination and heights were determined by GPS measurements.

Nineteen stations (A1–A19) with at least one ultrasonic anemometer (Model CSAT3, Campbell Scientific, Logan,

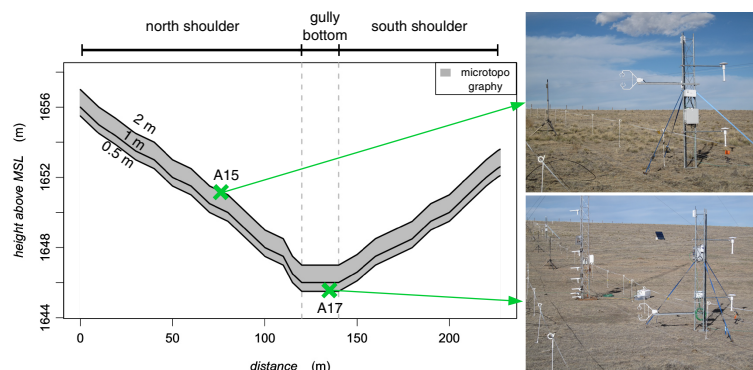


FIGURE 2 Cross-valley transect of DTS measurements during the SCP experiment. Topography is given as height above mean sea level (MSL) in metres and length of the DTS transect increasing from north to south. Black lines indicate DTS measurements, the green crosses ultrasonic anemometer stations A15 and A17, and grey shading the microtopography from GPS measurements. Source photos: https://www.eol.ucar.edu/field_projects/scp; accessed 2 March 2019 [Colour figure can be viewed at [wileyonlinelibrary.com](https://onlinelibrary.com)]

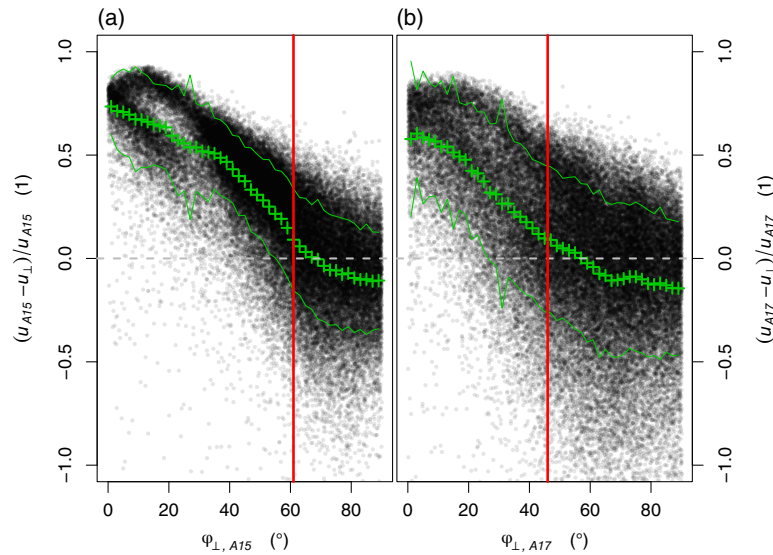


FIGURE 3 Validation of FO wind speed measurement by relative difference between ultrasonic anemometers and the nearest FO wind speed (a) $(u_{A15} - u_{\perp}) / u_{A15}$ and (b) $(u_{A17} - u_{\perp}) / u_{A17}$, in relation to the attack angle of the wind to the DTS transect φ_{\perp} . Bin averages over 2° (crosses) and standard deviations (lines) of the relative wind speed differences are added in green and the threshold values for attack angles in red [Colour figure can be viewed at wileyonlinelibrary.com]

UT, USA) at 1 m were installed at the experimental site in addition to a 20 m main tower with eight ultrasonic anemometers (0.5 m, 1–5 m, 10 m, 20 m). At the main tower, ventilated hygrothermometers from the National Center for Atmospheric Research (NCAR; <https://www.eol.ucar.edu/instruments/trh>; accessed 2 March 2019) were also installed at heights of 0.5 and 15 m. Radiation measurements were from a four-component net radiometer (Model CNR4, Kipp & Zonen, Delft, Netherlands) at 2 m height about 40 m west of the DTS transect. Potential temperatures were referenced to the 1 m height of the main tower in metres above mean sea level (MSL).

The transect for the DTS instrument (Ultima SR, Silixa, London, UK) was deployed along a 240 m cross-valley transect using an unheated optical glass fibre (FO) cable with an outer diameter (OD) of 0.9 mm to measure temperatures and an actively heated stainless-steel FO cable (1.3 mm OD) for measurements of the wind speed orthogonal to the FO cable. Each FO cable was installed at 0.5, 1 and 2 m agl (Figure 2). The temporal and spatial resolution of the DTS measurements were 5 s and 0.25 m, respectively. Artifacts from the fibre support causing additional heating or cooling of the fibre were removed and filled using linear interpolation spatially for each time step. The location of DTS measurement is given as southward increasing distance d in metres from the start point of the DTS transect at the north shoulder of the gully. Further, we assigned sections for the DTS transect: north shoulder (0–120 m), gully bottom (120–140 m) and south shoulder (140–225 m).

FO wind speed measurements were conducted as described by Sayde *et al.* (2015). The wind speed was quantified by

the convective energy transport from the heated cable to the moving air, which is a unique function of the wind speed and temperature difference between the actively heated and the unheated FO cable. However, this measurement technique is also dependent on the angle of attack (φ_{\perp}) between the moving air and the FO cable. We validated the dependency of FO wind speed on the attack angle by calculating the relative wind speed difference between the ultrasonic anemometer stations A15 (2 m agl) and A17 (0.5 m agl) situated directly at the DTS transect and the nearest FO wind speed measurement u_{\perp} (Figure 3).

The FO wind speed measurements underestimated the wind speed for attack angles lower than a threshold, while above the threshold the bin-averaged relative difference was smaller than ± 0.1 . The deviation from sonic anemometer measurements was higher for the 2 m height at A15 (Figure 3a) than for the 0.5 m height at A17 (Figure 3b). Accordingly, FO wind speed measurements for attack angles smaller 61° and 46° , respectively, were discarded, amounting to 59.9% for the 2 m and 1 m heights and 36.6% for the 0.5 m height.

3.2 | Definition of variables for night classification scheme

3.2.1 | Static stability classes

We used static stability instead of dynamic stability as the dependence of the nocturnal boundary layer on wind speed and friction velocity is already incorporated by adding the wind regime as an input variable into the night classification scheme.

Static stability $\Delta_z\theta$ was determined by the difference of the potential temperature of the hygrothermometers between 15 m and 0.5 m heights at the main tower. The study of Mahrt and Heald (2015) at the same field site defined near-neutral stratification for a magnitude of vertical temperature differences smaller than 0.1 K. So we decided to choose a range of $\Delta_z\theta$ between -0.1 and 0.1 K for statically neutral stratification with a well-mixed boundary layer during these conditions. $\Delta_z\theta > 0.1$ K represents statically stable conditions, while statically unstable conditions were defined by $\Delta_z\theta < -0.1$ K. For our data, 1.7% fell into statically neutral, 95.8% statically stable and 2.0% statically unstable conditions.

3.2.2 | Wind regime classes

We used two of the three wind regimes proposed in figure A1 of Sun *et al.* (2012) for the night classification scheme. Regime 1, the weak-wind regime, features wind speeds below a certain threshold value and is characterized by a weak correlation between the wind speed u and friction velocity u_* . We interpret this behaviour as a result of the turbulence responding to both local wind speed shear and vertical temperature gradient. Further, eddies generated by the local shear may not interact with the ground depending on measurement height. Regime 2, the strong-wind regime, shows a strong linear dependence of the friction velocity on wind speed, because the turbulence increases systematically with increasing wind speed. The transition between the two regimes is defined by a threshold wind speed.

The relationship between wind speed and friction velocity was analyzed for both wind regimes using the observations from all 19 stations at 1 m (A1–A19) with a temporal resolution of 5 min for the nocturnal data. Therefore, the best linear fit was computed iteratively for both wind regimes. As a start value for the linear fit function, an arbitrary wind speed threshold value of 1 m/s was chosen dividing the data into the

proposed weak-wind and strong-wind regime and the linear fit function calculated the linear correlation for both regimes. The threshold value was then shifted until the highest correlation coefficient R^2 below and above the threshold value was reached (Figure 4a). As expected for the weak-wind regime, the linear correlation was low, with a R^2 of 0.01, while the strong-wind regime had a very high correlation, with a R^2 of 0.83, a slope of 0.09 and intercept of -0.03 . The intersection of both lines was at a threshold wind speed of 1.2 m/s.

Similar thresholds between 1.0 and 1.8 m/s at heights of 0.5 and 1.5 m were determined by the study of Sun *et al.* (2012) in comparable terrain, consistent with our threshold of 1.2 m/s at the 1-m height. Hence, we chose the ultrasonic anemometer at 1-m height of the main tower to determine the wind regime, where also static stability and the dLRF classes were defined. The 1-m station at the main tower determined 25.2% of the nocturnal data as weak-wind regime and 74.8% as strong-wind regime.

3.2.3 | Downwelling long-wave radiative forcing classes

Some studies suggest that cloud cover is a driving factor in boundary-layer development by claiming that the net radiation balance is mainly dependent on the surface temperature, but is significantly altered by cloud cover (e.g. Paltridge, 1974; Foken, 2017a). We evaluated this assumption for our experiment. At our field site no direct cloud observations were made, however measurements of short- and long-wave radiation with a temporal resolution of 5 min were available. We tested the Automated Partial Cloud Amount Detection Algorithms (APCADA) to determine the cloud cover using the incoming long-wave radiation (e.g. Marty and Philipona, 2000; Dürr and Philipona, 2004). APCADA uses the downwelling long-wave radiation to compute a cloud-free index, which is the ratio of effective emissivity to theoretical clear-sky emissivity, and combines it with the fluctuation of the downwelling long-wave radiation to derive the cloud cover (in okta). We sorted the APCADA classes to our dLRF classes on the basis of table 3 of Dürr and Philipona (2004) (Figure A3). For our data we found that a classification based on fractional cloud cover gave less physically meaningful boundary layers than one based only on the downwelling long-wave radiation. APCADA classes showed a decrease in $-Q_s^*$ from APCADA 0/8 to 8/8, while each corresponding dLRF class showed a wider range of $-Q_s^*$, and boxplots of neighbouring dLRF classes overlapped more than those of the APCADA classes (Figure A3). Even though the APCADA classes correlate well with $-Q_s^*$, the spatial temperature perturbation of each APCADA class was barely different and the range of perturbations did not decrease for increasing fractional cloud cover (Figure A4a,b) in contrast to the dLRF classes (cf. section 4.3). From this we contend that the fractional cloud cover exerts less of a control on the boundary-layer behaviour than the downwelling long-wave radiative forcing (dLRF).

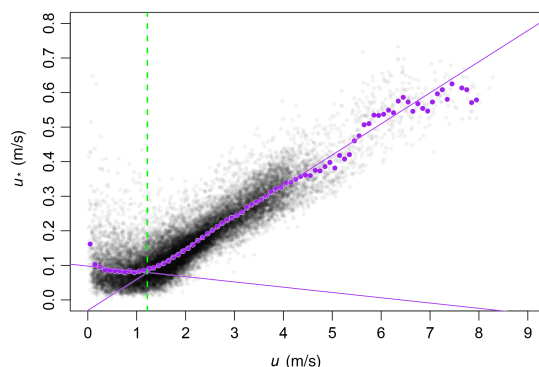


FIGURE 4 Determination of weak-wind regime by relation between friction velocity u_* and wind speed u of all 1 m stations visualized by black dots. Purple dots are bin averages of u_* . Purple lines show the best linear fits, and the vertical green line marks the intersection of the fitted lines [Colour figure can be viewed at wileyonlinelibrary.com]

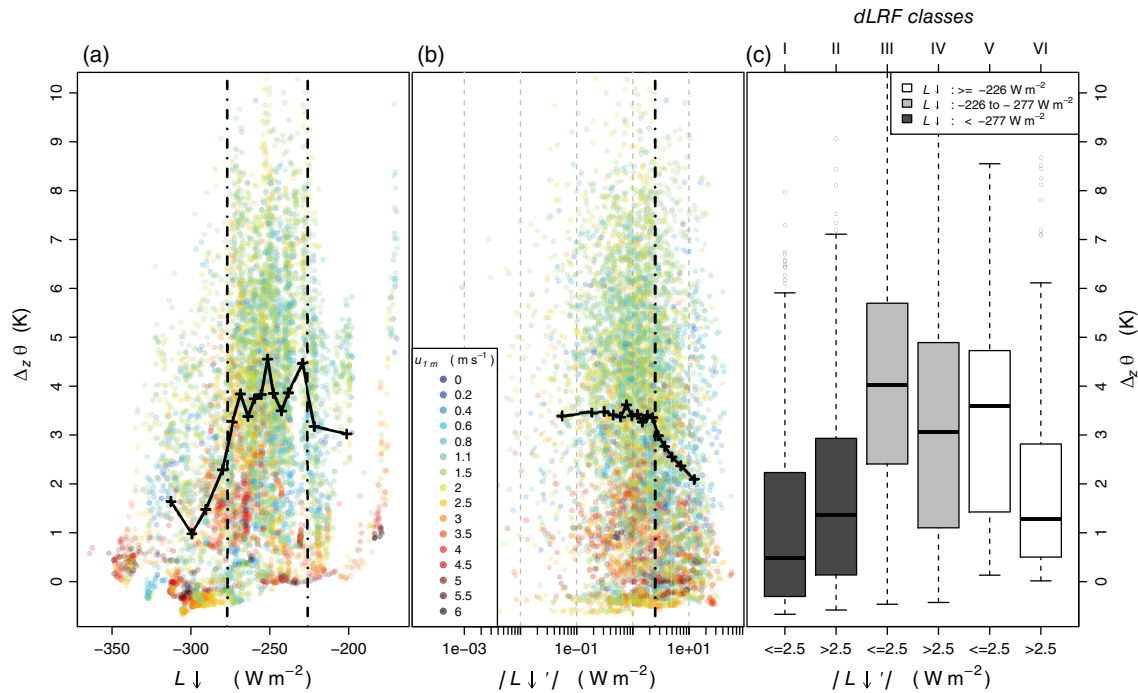


FIGURE 5 (a) Downwelling long-wave radiation L_d plotted against the vertical temperature difference between 15 and 0.5 m ($\Delta_z \theta$). (b) Fluctuation of $|L'_d|$ defined as the absolute deviation from the hourly mean plotted against $\Delta_z \theta$. (c) Distribution of $\Delta_z \theta$ for each downwelling long-wave radiative forcing (dLRF) class (top axis) defined by L_d (grey shading) and $|L'_d|$ (bottom axis). Boxplots show the median and interquartile range. Wind speed at the 1 m station at the main tower (u_{1m}) are indicated by colours in (a) and (b). Vertical dashed lines indicate threshold values for L_d and $|L'_d|$ defining dLRF classes. [Colour figure can be viewed at wileyonlinelibrary.com]

We defined the dLRF classes by the magnitude of incoming long-wave radiation L_d and its absolute temporal fluctuation $|L'_d|$, which is the deviation from the hourly mean. To objectively determine dLRF classes, we used the long-wave radiation as well as hygrothermometer data from 1 October until 1 December 2012 and investigated the relation between the vertical difference of potential temperatures $\Delta_z \theta$ (cf. section 3.2.1) and L_d as well as between $\Delta_z \theta$ and $|L'_d|$ (Figure 5a,b). We observed a large scatter of $\Delta_z \theta$ for similar values of L_d or of $|L'_d|$, which was mainly caused by strong wind speeds reducing $\Delta_z \theta$ by turbulent mixing. We therefore added the 1 m wind speed u_{1m} as colours in Figure 5a,b. Nevertheless, a clear correlation of $\Delta_z \theta$ to L_d and to $|L'_d|$ can be seen when computing bin averages of $\Delta_z \theta$ for increasing L_d and for increasing $|L'_d|$, with each bin spanning a fixed width of 400 data points (black lines and crosses). We did not add errorbars as the standard error of the mean was very small with values around 0.1 K and the distribution of $\Delta_z \theta$ is already shown in the scatterplots.

We determined two thresholds for L_d and one for $|L'_d|$ by evaluating maximum values of the first derivative of the bin averages, i.e. the highest change of the bin averages of $\Delta_z \theta$ between neighbouring bins, which are visualized by black vertical lines. As a result, we identified three regions for L_d with different mean values of $\Delta_z \theta$. For very low

values $L_d < -277$ W/m², very low bin averages of $\Delta_z \theta$ were observed (1.0–2.3 K), while for $-277 < L_d < -226$ W/m², the highest bin averages of $\Delta_z \theta$ were reached (3.3–4.5 K), and for $L_d > -226$ W/m² bin averages of $\Delta_z \theta$ ranged from 3.0 to 3.2 K (Figure 5a). Similarly, for $|L'_d| > 2.5$ W/m² bin averages of $\Delta_z \theta$ decreased significantly down to 2.1 K, while bin averages of $\Delta_z \theta$ showed values of 3.4 K with no relation to $|L'_d|$ for $|L'_d| < 2.5$ W/m² (Figure 5b).

The final dLRF classes used for our nocturnal classification scheme were selected using the three regions of L_d determined by the threshold values of -277 and -226 W/m² in combination with two regions of $|L'_d|$ determined by the threshold value of 2.5 W/m² (cf. Figure 5c). In this figure we also show the difference in $\Delta_z \theta$ between the dLRF classes.

4 | RESULTS AND DISCUSSION

4.1 | Static stability forcing

Statically unstable and neutral stratification revealed the lowest range of spatial temperature perturbations $[\hat{\theta}]$ with slightly higher temperatures at the gully bottom (0.1 K) than on both shoulders (−0.1 K) (Figure 6a). Also the lowest temporal temperature perturbations $[\hat{\theta}^2]$ were detected for these two stability classes (Figure 6b). The two stability classes showed

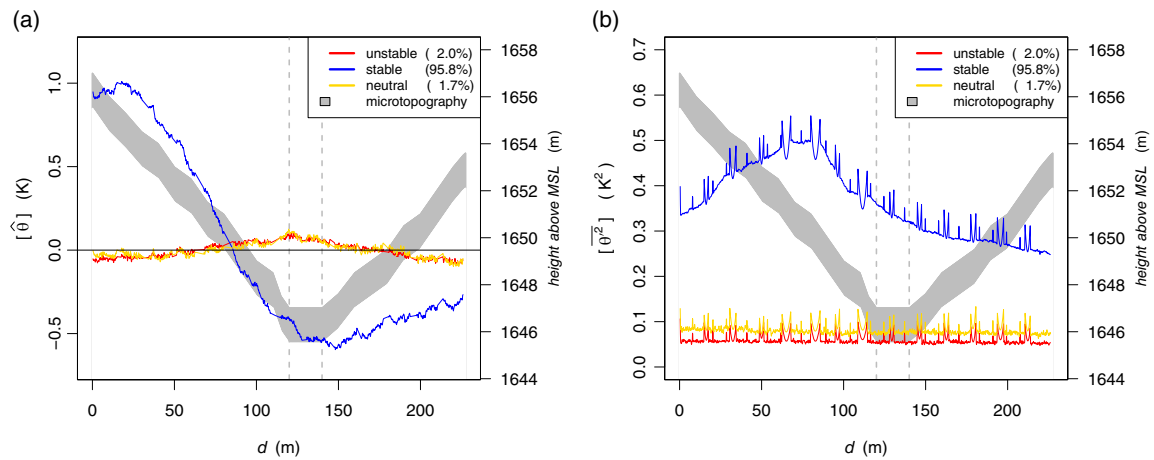


FIGURE 6 (a) Spatial ($\langle \hat{\theta} \rangle$) and (b) temporal ($\langle \hat{\theta}^2 \rangle$) temperature perturbation ensemble averaged for each static stability class. Abundance is given as a percentage of complete night-time data in the legend [Colour figure can be viewed at wileyonlinelibrary.com]

similar spatio-temporal temperature perturbations, because statically unstable stratification was weak with a mean $\Delta_z \theta$ of -0.3 K and only occurred between periods of neutral stratification. Hence, statically neutral and statically unstable stratification showed vanishing temperature perturbations temporally, horizontally, and vertically.

In contrast, statically stable stratification showed high temporal and spatial temperature perturbations (Figure 6a,b). Spatial temperature perturbations mimicked the microtopography with lowest temperatures at the gully bottom and higher temperatures at the gully shoulders.

The three static stability classes had similar *SEM* for $\langle \hat{\theta} \rangle$ (stable 0.003 K; neutral 0.004 K; unstable 0.003 K), while for $\langle \hat{\theta}^2 \rangle$ statically neutral and unstable conditions had lower values with 0.0011 K² and 0.0004 K² compared to stable conditions with 0.0025 K².

4.2 | Wind regime forcing

The wind regimes had the biggest impact on the bulk Richardson number [Ri_b] with values ranging from 0.2 to 1.3 for the weak-wind regime and values ranging only up to 0.15 for the strong-wind regime (Figure 7). By definition, the flow during the strong-wind regime is more turbulent than during the weak-wind regime. Spatial (Figure 8a) and temporal (Figure 8b) temperature perturbations showed strong differences for the wind regimes. Due to the increased turbulence during strong winds, a lower spatial and temporal temperature perturbation could be expected. However, even the strong-wind regime showed significant spatial and temporal temperature perturbations, but with a different spatial pattern within the transect than the weak-wind regime. For weak winds, spatial and temporal temperature perturbations closely followed the microtopography, with the lowest values at the gully bottom and higher values on the shoulders. In contrast,

observations during strong winds showed small temperature variance on the south shoulder, but strong temperature variance on the north shoulder as a result of lee turbulent mixing transporting warmer air from aloft down to the surface (cf. sections 4.3 and 4.4).

The weak-wind regime showed higher *SEM* than the strong wind regime with values of 0.006 K for $\langle \hat{\theta} \rangle$ and 0.0045 K² for $\langle \hat{\theta}^2 \rangle$ compared to 0.004 K and 0.0028 K². We speculate that the strong-wind regime shows smaller *SEM* since the boundary layer is dynamically forced with a linear relation between turbulence and wind speed, resulting in smaller temperature perturbations both horizontally and vertically. Hence, the strong-wind regime experiences smaller temporal variations than the weak-wind regime.

Accordingly, during the weak-wind regime, with weaker turbulence especially at the gully bottom, spatio-temporal temperature perturbations followed the microtopography,

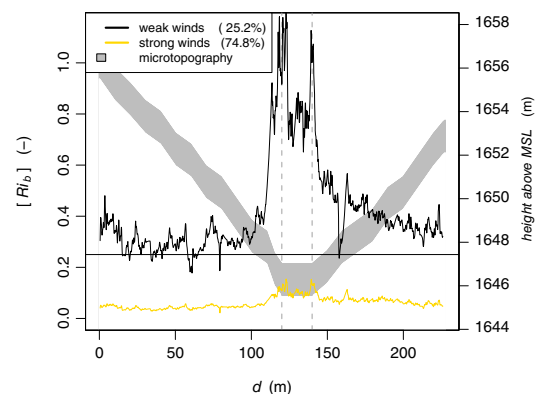


FIGURE 7 Bulk Richardson number Ri_b ensemble averaged for each wind regime. Abundance is given as percentages of complete night-time data. The horizontal line denotes the critical Ri_b [Colour figure can be viewed at wileyonlinelibrary.com]

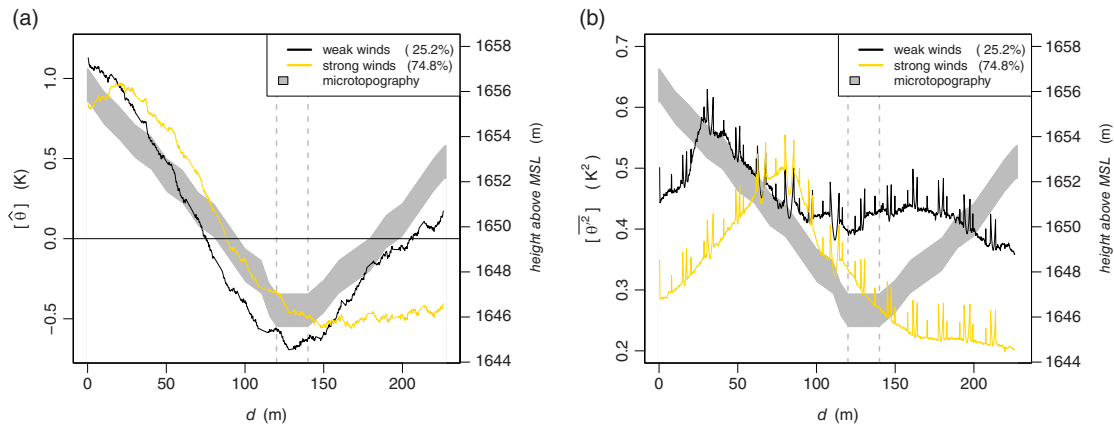


FIGURE 8 (a) Spatial ($\hat{\theta}$) and (b) temporal ($\hat{\theta}^2$) temperature perturbations ensemble averaged for each wind regime. Abundance is given as percentages of complete night-time data [Colour figure can be viewed at wileyonlinelibrary.com]

while turbulent flow dominated during the strong-wind regime with clearly different spatio-temporal temperature perturbations. Hence, the wind regimes distinctly divide the data into the weak-wind and strong-wind regime, both of which feature characteristically different patterns in spatial and temporal temperature perturbations.

4.3 | Downwelling long-wave radiative forcing

Analyzing the impact of the dLRF classes on near-surface temperatures from DTS revealed differences in the spatio-temporal temperature perturbations $\hat{\theta}$ and $\hat{\theta}^2$ (Figure 9a,b). The highest spatio-temporal temperature perturbations could be found for dLRF classes III and V. dLRF class III had intermediate L_d in combination with a low fluctuation of L_d . Hence, cold-air formation was likely to occur, resulting in low temperatures at the gully bottom and higher temperatures at the shoulders (yellow line Figure 9a).

However, the north shoulder ($d < 120$ m) showed the highest temperatures as indicated by maximum values of $\hat{\theta}$ up to 1.1 K, in addition to a peak in temporal temperature perturbations, $\hat{\theta}^2$, up to 0.65 K² at a distance $d \approx 83$ m (Figure 9b). Those peaks of spatial and temporal temperature perturbations on the north shoulder were most likely caused by lee turbulent mixing events. The turbulent mixing and increase of temperature induced a horizontal temperature difference between the cold air at the gully bottom and warmer air at the north shoulder. However, the spatial extent of lee turbulence within the transect was not stationary, i.e. the warmer downward-mixed air moved back and forth depending how far the lee turbulence reached within the transect. As a result, the temperature at any point in the transect could change rapidly in time as a result of the transient thermal microfront. Lee turbulent mixing resulted in a higher spatial and temporal temperature perturbation especially on the north shoulder. This observation agrees with the study of Mahrt (2017a),

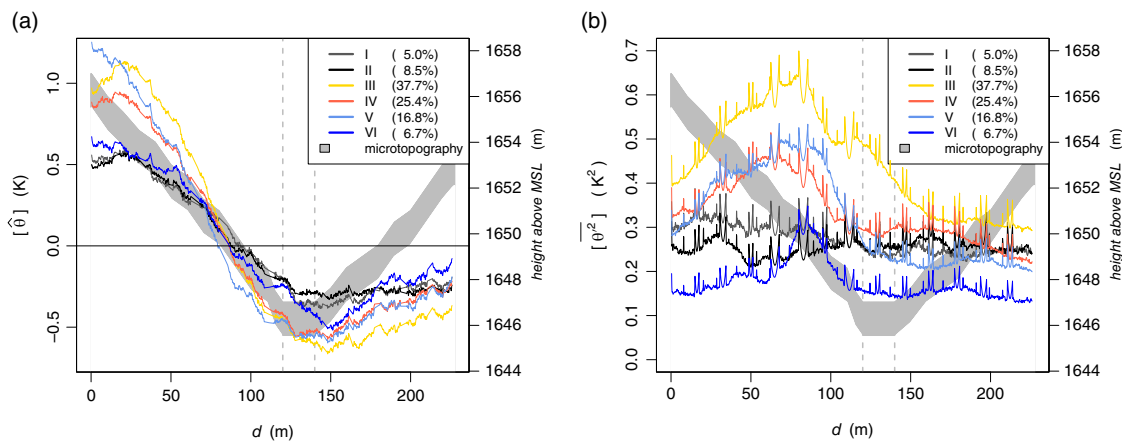


FIGURE 9 (a) Spatial ($\hat{\theta}$) and (b) temporal ($\hat{\theta}^2$) temperature perturbation ensemble averaged for each dLRF class. Abundance is given as percentages of complete night-time data [Colour figure can be viewed at wileyonlinelibrary.com]

which investigated stably stratified flow for the same field experiment. They concluded that lee turbulence is induced at the north shoulder by the adjacent miniplateau. The nearest stations to this plateau (A4, A9 and A10) are characterized by the largest potential temperatures and largest downward heat flux among all stations of the network.

The spatial, as well as temporal, temperature perturbations are not only induced by the arrival frequency and strength of lee turbulent mixing events. dLRF class V had almost the same number of lee turbulent mixing events as dLRF class III, but spatial temperature perturbations were higher for dLRF class V, ranging from -0.6 K up to 1.3 K, while temporal temperature perturbations were lower with a peak value of only 0.50 K² at $d \approx 83$ m (Figure 9a,b). dLRF class V featured low L_1 in combination with a low fluctuation of L_1 promoting cold-air formation and thus leading to low temperatures at the gully bottom and higher temperatures at the shoulders. The lee turbulent mixing only increased the temperature at the north shoulder and created the peak in $[\theta'^2]$, while for $d > 120$ m spatial temperature perturbations followed the microtopography with lowest temperatures at the bottom. Generally, temperature perturbations were small where lee turbulent mixing was negligible ($d > 140$ m) (Figure 9b).

The lowest spatio-temporal temperature perturbations were found for dLRF classes I and II, both featuring high L_1 , but a low fluctuation of L_1 for dLRF class I and a high fluctuation of L_1 for dLRF class II. Even though the spatio-temporal temperature perturbations barely differed between these two dLRF classes, they did significantly differ when combined with wind or static stability regimes (not shown). During those two dLRF classes, lee turbulent mixing events occurred for 17.5% and 25.3% of the time, respectively. In contrast to other dLRF classes, classes I and II did not yield any systematic characteristic spatial pattern of the temperature perturbations.

Fluctuation in L_1 impacted spatio-temporal temperature perturbations within the DTS transect. Spatial and temporal temperature perturbations significantly differed between dLRF classes with a similar L_1 , but different levels of fluctuation of L_1 . For example dLRF class V, with a low fluctuation of L_1 , showed high spatial and temporal temperature perturbations, while for dLRF class VI, with a high fluctuation of L_1 , only small spatial and temporal temperature perturbations were found. Both classes should have offered perfect conditions for radiative cooling and thus cold-air drainage and pooling. Further, both classes had a similar wind speed range with mean wind speeds of 2.2 m/s for dLRF class V and 2.5 m/s for dLRF class VI. However, for dLRF class VI, cold-air formation was suppressed by strong variations in L_1 impeding the formation of temperature variations. Comparing both dLRF classes during lee turbulent mixing events, or during the absence of those, revealed the same results (not shown).

dLRF classes showed the highest *SEM* compared to the other input variables ranging from 0.010 K to 0.006 K for $[\hat{\theta}]$ and from 0.0034 K² to 0.0070 K² for $[\theta'^2]$. Such large

values indicate that within dLRF classes a high spread of spatio-temporal temperature perturbations exists. We believe that this spread is also dynamically forced, as dLRF classes averaged over different wind regimes showing different spatial and temporal temperature perturbations, as shown above.

In summary, spatial and temporal perturbations of near-surface air temperature are highly affected by the magnitude of downwelling long-wave radiation as well as by its temporal variability. As a result, we chose dLRF classes to represent radiative forcing of the nocturnal boundary layer to distinguish between physically meaningful regimes.

4.4 | Boundary-layer regimes derived from the night classification scheme

Combining the six dLRF classes, the three static stability classes, and the two wind regimes yielded a total of 36 night classes (cf. Figure 1). Based on the results presented above, we decided to combine all classes for neutral stratification creating a well-mixed boundary layer independent of dLRF or wind regime, which reduced the total number of night classes to 25. As the results of neutral and unstable stratification were almost identical and we only found one night class with unstable stratification, we decided also to combine all classes for unstable stratification which reduced the total number of night classes to 14.

After sorting all 5 min observation intervals, all 14 night classes contained data. The ten night classes containing the most data are listed in Table A1. Out of these we selected three classes for further analysis guided by the abundance of data and their representativeness for idealized transport regimes at the SCP site. Even though our selection was arbitrary to some degree, a different choice would have focused on classes representing rather transitional regimes. We think it is valuable to initially focus on the end members of the continuous spectrum defined by the interplay between the boundary-layer forcings. We will compare ensemble averages of $[\hat{\theta}]$, $[\theta'^2]$ and $[R_b]$, as well as profiles of sensible heat flux and wind speed and direction for the following three night classes all featuring stable conditions:

- NC 1: strong winds+dLRF class III (intermediate L_1 +low $|L'_1|$)
- NC 3: strong winds+dLRF class V (low L_1 +low $|L'_1|$)
- NC 4: weak winds + dLRF class IV (intermediate L_1 + high $|L'_1|$)

First we compared the wind speed and direction of each night class at the main tower at 20 m agl with station A17 at the gully bottom at 0.5 m agl (cf. Figure 2). NC 1 showed the highest wind speeds with 67.1% exceeding 4.0 m/s, mostly coming from the northwest, while NC 3 experienced lower wind speeds (53.7% >4.0 m/s) in combination with a shift to more westerly winds and the absence of winds from the southwest to east (Figure A5a). NC 4 showed the lowest wind speeds with only 11.5% exceeding 4.0 m/s mainly from the

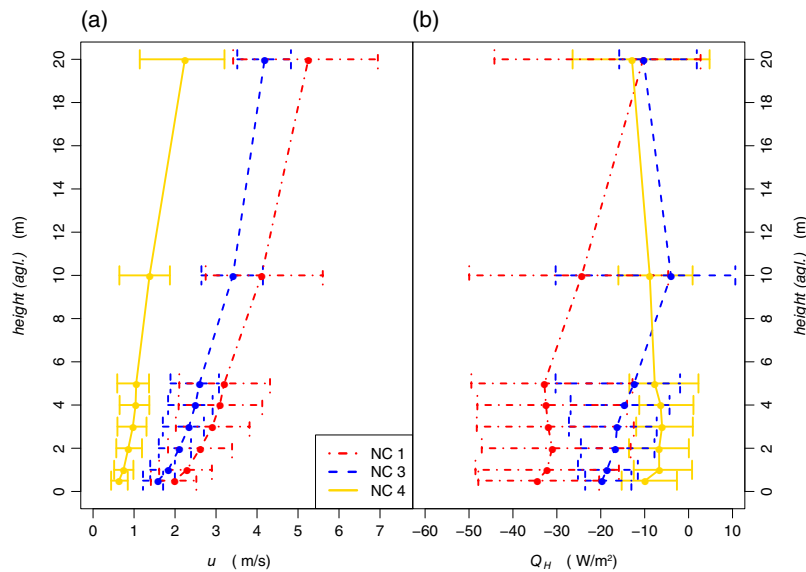


FIGURE 10 (a) Wind speed u and (b) sensible heat flux Q_H computed for each height of the main tower for each night class (colours). Dots show the mean values and the whiskers show the interquartile range (IQR) [Colour figure can be viewed at wileyonlinelibrary.com]

north and northeast. Hence, the wind direction above the valley was associated with a specific night class representing a specific boundary-layer regime. Similar differences for wind speed and direction were found for the station A17 at the gully bottom (Figure A5b). When comparing the wind directional shear between station A17 and the 20 m station, NC 1 and 3 revealed rather small shear angles with a mean of 38° and 28° , respectively, while NC 4 revealed a mean of 68° . Hence, the two night classes with a strong-wind regime revealed rather low wind directional shear, while the night class with a weak-wind regime experienced strong directional shear.

The selected night classes showed distinctly different wind and sensible heat flux profiles (Figure 10). By definition, NC 4 had the lowest wind speeds and could clearly be differentiated from NC 1 and 3 (Figure 10a). The interquartile ranges (IQR) of the wind speed for NC 1 and 3 overlap, but the IQRs of NC 3 were smaller and the increase of the mean wind speed with height was less steep than in NC 1. Hence, NC 1 featured higher vertical wind shear and associated turbulent mixing. These findings agree with the vertical profiles of Q_H of each night class (Figure 10b). When comparing observations below 10 m, NC 1 showed the highest $Q_H \approx -35$ W/m², while NC 3 revealed lower values ≈ -15 W/m² and NC 4 had the lowest means ≈ -10 W/m². We conclude that NC 1 had the highest sensible heat flux because of the strong winds and enhanced turbulent mixing. NC 3 had lower wind speeds than NC 1 in combination with very low magnitude of L_1 , favouring generation of cold air, both reducing the sensible heat flux through reduced turbulent mixing and enhanced static stability. The heat flux profile of NC 4 showed the smallest sensible heat flux, as the boundary layer is turbulence-limited due to the weak-wind regime. We also

highlight different vertical divergence of mean Q_H between the night classes. NC 1 had intermediate, NC 3 the highest and NC 4 the lowest divergence, but NC 4 had the highest divergence of all at the surface. All three night classes reached similar values of Q_H at the 20 m height, since this height is most likely already outside the near-surface boundary layer.

Distinct differences in spatio-temporal temperature perturbations and the bulk Richardson number were found. NC 1 and NC 4 had similar L_1 of ≈ -250 W/m². However, NC 1 revealed high temperature perturbations at the north shoulder and low temperature perturbations at the south shoulder, while temperature perturbations were mimicking the microtopography during NC 4 with the lowest temperatures at the gully bottom and higher temperatures at the shoulders (Figure 11a). NC 3 had the smallest magnitude of L_1 with a mean of -209 W/m², but very similar spatial temperature perturbations to NC 1. Nevertheless, NC 1 and NC 3 differed significantly in temporal temperature perturbations (Figure 11b) and in Ri_b (Figure 12). NC 3 showed lower temperature perturbations, especially on the south shoulder ($d > 140$ m), where lee turbulent mixing was negligible, while NC 1 showed a stronger variability of temperatures along the transect. NC 3 showed higher Ri_b especially at the gully bottom, indicative of cold-air formation, which was absent during NC 1 caused by the enhanced L_1 . The highest values of $Ri_b > 0.25$ were found for NC 4. These results suggest that the downwelling long-wave radiation limits the magnitude of spatio-temporal temperature perturbations, while the wind regime impacts their spatial distribution.

Despite these differences, all three night classes showed an asymmetry between the gully shoulders with higher spatial and temporal temperature perturbations on the north shoulder

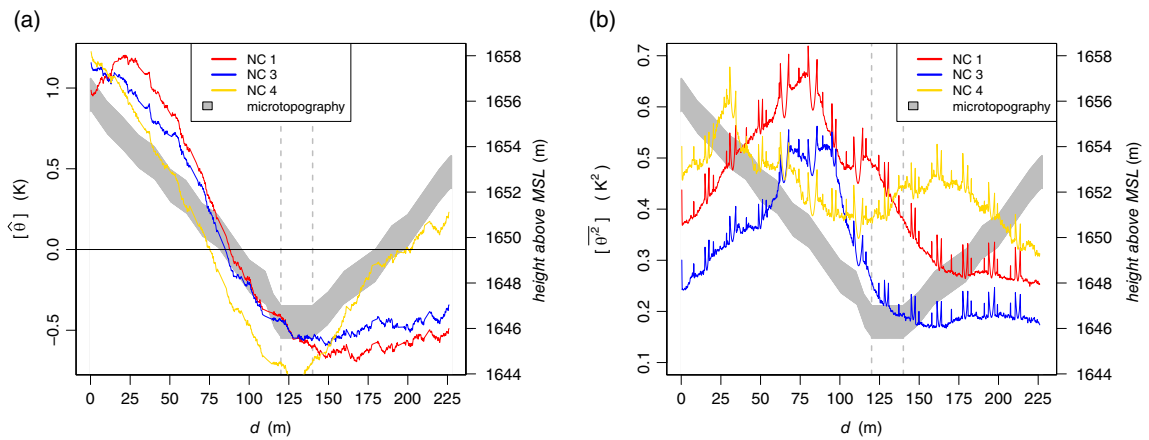


FIGURE 11 (a) Spatial ($\langle \hat{\theta} \rangle$) and (b) temporal ($\langle \hat{\theta}^2 \rangle$) temperature perturbations ensemble averaged for each night class [Colour figure can be viewed at wileyonlinelibrary.com]

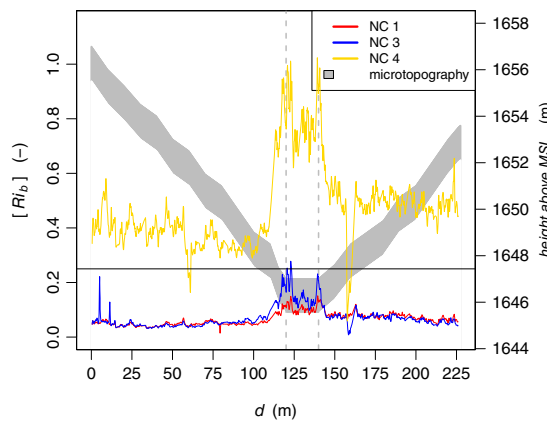


FIGURE 12 Bulk Richardson number values ensemble averaged $[Ri_b]$ for each night class. The horizontal line denotes the critical Ri_b [Colour figure can be viewed at wileyonlinelibrary.com]

and reduced or vanishing perturbations on the south shoulder. This asymmetry is a result of the lee turbulence mixing events. We conclude that, depending on the wind speed, lee turbulence is generated acting to increase the downward heat flux and near-surface temperatures up to 150 m into the DTS transect (cf. Figure 11). This semi-stationary mixing causes the strong differences in spatio-temporal temperature perturbations between the gully shoulders. All night classes revealed flows approaching from northwest to north as indicated by the 20 m tower (Figure A5a) for which lee turbulent mixing events occurred (Mahrt, 2017a). We detected the peak of temporal temperature perturbations at $d \approx 80$ m. However, the range and magnitude of spatial and temporal temperature perturbations differ systematically between the night classes. The lee turbulent mixing events cause distinct thermal microfronts, which could only be detected in the spatially continuous DTS observations. The passage of a transitory microfront in point observations from classic time-domain

sonic anemometry was difficult or impossible to separate from the thermal fingerprint of turbulent and submeso-scale motions. However, a detailed investigation using the DTS data and characterization is outside the scope of this paper, but will be analyzed in a separate study.

The *SEM* for night classes differed with the lowest values for NC 1 ($\langle \hat{\theta} \rangle$ 0.006 K; $\langle \hat{\theta}^2 \rangle$ 0.0055 K²), intermediate values for NC 3 ($\langle \hat{\theta} \rangle$ 0.009 K; $\langle \hat{\theta}^2 \rangle$ 0.0049 K²) and highest values for NC 4 ($\langle \hat{\theta} \rangle$ 0.012 K; $\langle \hat{\theta}^2 \rangle$ 0.0072 K²). However, the *SEM* does not change the spatial pattern of temperature perturbations discussed above, and the *SEM* values themselves are small compared to the mean values.

In summary, we found that wind direction, wind speed, sensible heat flux, spatio-temporal temperature perturbations, as well as Ri_b differed significantly between the night classes. In the following sections we continue characterizing the boundary-layer regimes for the selected night classes by discussing case studies (sections 4.4.1 - 4.4.3) subject to multi-resolution decomposition for the following intervals:

- NC 1: 19–20 November 2100–0400 (81.0%)
- NC 3: 22–23 November 2130–0430 (85.7%)
- NC 4: 23–24 November 2130–0230 (66.7%).

No interval long enough could be found to represent only one night class, but we chose the case studies aiming at the highest possible abundance. The percentage indicates the abundance of each night class within the interval.

4.4.1 | Boundary-layer regime of Night Class 1

In NC 1, one expects a boundary layer in which the strong-wind regime dominates spatio-temporal temperature perturbations. The magnitude of the incoming long-wave radiation is large and enhanced shear-generated mixing is anticipated, which prevents cold-air formation and pooling.

The existence of enhanced turbulent mixing and friction velocities could be confirmed with peak wind speeds ranging up to 13.2 m/s with a mean of 5.3 m/s at the 20 m height of the

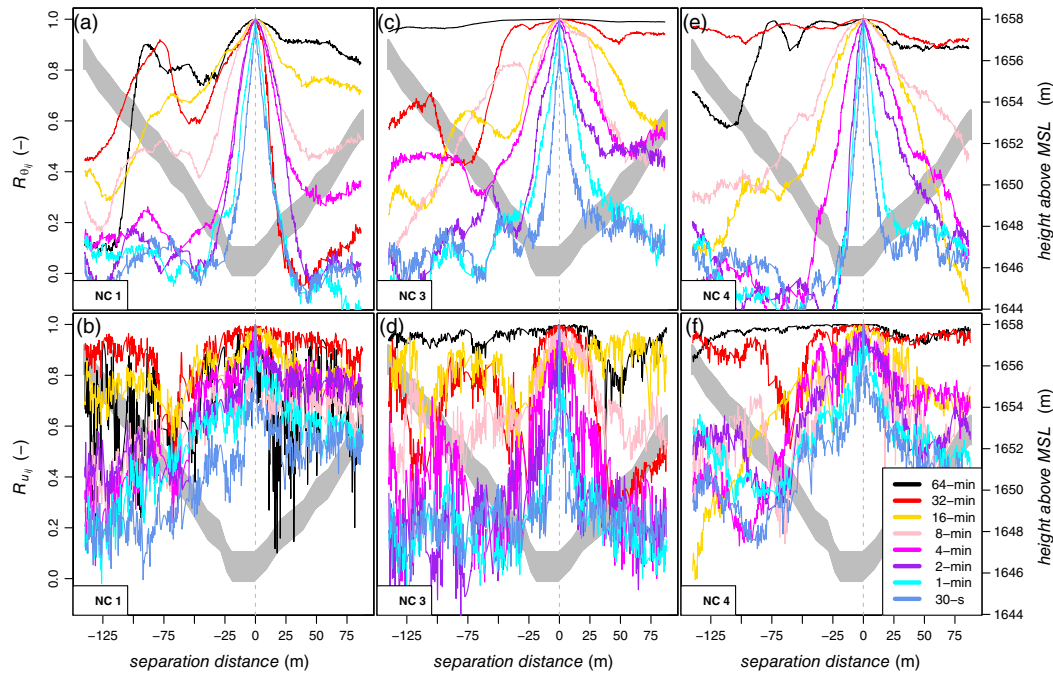


FIGURE 13 Spatial correlation of (a, c, e) temperature $R_{\theta_{ij}}$ and (b, d, f) wind speed $R_{u_{ij}}$ versus separation distance between the reference point i at the gully bottom and the distant point j for different time-scales (colours) for (a, b) NC 1, (c, d) NC 3 and (e, f) NC 4 [Colour figure can be viewed at wileyonlinelibrary.com]

main tower, and high friction velocities at station A15 at the north shoulder and station A17 at the gully bottom with mean values of 0.20 m/s and 0.14 m/s, respectively. Contrary to our expectation, measurements determined the net radiation balance as -58 W/m^2 , which could be sufficient to support cold-air formation. However, a significant L_d of -276 W/m^2 in combination with a small fluctuation of L_d with a mean of 1.0 W/m^2 counteract the formation of cold air. Following the dLRF class instead of the net radiation balance, we expect that, if a cold-air layer did accumulate at the gully bottom, it was very shallow.

The DTS observations were indicative of the existence of a cold-air layer by showing a strong spatial correlation of temperatures $R_{\theta_{ij}}$ at and near the gully bottom for all time-scales and separation distances $\pm 15 \text{ m}$ (Figure 13a). However, for separation distances beyond 15 m, the spatial correlation of temperature diminished quickly, which indicated different temperature dynamics at both shoulders compared to the gully bottom. The bulk Richardson number Ri_b was larger at the gully bottom (≈ 0.10) than at the gully shoulders (≈ 0.06) (Figure 12), which may indicate weaker turbulence through strong stratification. So only a sonic anemometer at the gully bottom was able to detect this cold-air pooling, however the horizontal spatial extent of this cold-air pool could only be quantified by the DTS technique.

Lee turbulent mixing events as described by Mahrt (2017a) were evident during NC 1 supported by high friction velocities at station A15 on the north shoulder. Here, high spatial

and temporal temperature perturbations were found with peak values of 1.2 K and 0.70 K^2 , respectively, while temporal and spatial temperature perturbations at the south shoulder ($d > 140 \text{ m}$) were much smaller (Figure 11a,b). The two-point spatial correlation coefficient of temperature $R_{\theta_{ij}}$ showed a faster decay with increasing separation distances on the north shoulder than at same distances along the south shoulder (Figure 13a). As an example, $R_{\theta_{ij}}$ for the 16 min time-scale did not drop below 0.7 for positive separation distances at the south shoulder, while $R_{\theta_{ij}}$ decreased rapidly for separation distances $< -35 \text{ m}$ on the north shoulder. Additionally, all time-scales exhibited a minimum or sudden drop in $R_{\theta_{ij}}$ at a separation distance of about -35 m . At this position, lee turbulent mixing events were observed most frequently leading to the strong spatial decorrelation. During the NC 1 case study, 84% of intervals showed lee turbulent mixing.

A drop in the spatial correlation for temperature for the 64-min time-scale was observed (Figure 13a,b), in contrast to results from Thomas (2011) and Pfister *et al.* (2017) who also performed a MRD analysis of sonic network or DTS observations. Both studies found almost no drop of the spatial correlation for temperature across the entire domain at the 64-min time-scale, because near-surface temperatures followed the diurnal cycle of heating during the day and cooling during the night. However, the case studies discussed here spanned only 7 hr for one night, which apparently is insufficient to capture the complete cycle of nocturnal cooling.

The spatial correlation of wind speeds $R_{u_{ij}}$ mainly remained >0.3 for all time-scales (Figure 13b). With the exception of the 64-min time-scale, all time-scales decreased slowly with increasing separation distance. As an example, the 32-min time-scale stayed at $R_{u_{ij}} > 0.8$. This means that the entire transect was subject to the same flow dynamics at all time-scales. In fact, we found that flow dynamics did not change much along the transect, showing a homogeneous flow field across the gully. Consequently, the impact of the wind regime on this boundary-layer regime was strong.

In summary, we could show that the near-surface temperatures of NC 1 were influenced by enhanced lee turbulent mixing on the north shoulder, by the strong-wind regime, and by the downwelling long-wave radiation, while the net radiation balance was misleading.

4.4.2 | Boundary-layer regime of Night Class 3

NC 3 featured stable stratification, strong winds and low dLRF associated with clear-sky conditions. Hence, one expects a stable boundary layer, in which strong surface cooling acting to suppress turbulence competes with enhanced turbulent mixing due to significant winds. The mean downwelling long-wave radiation was -209 W/m^2 , so a smaller amount of incoming long-wave radiation than for NC 1 supported cold-air formation. The net radiation balance was large with -71 W/m^2 , also confirming strong radiative cooling. The wind speeds for NC 3 were lower than in NC 1, but still were substantial with a mean wind speed of 4.2 m/s at the 20 m height of the main tower and enhanced friction velocities at A15 (0.15 m/s) and at A17 (0.10 m/s).

Observations from the DTS transect confirmed the anticipated cold-air formation as the spatial temperature perturbations closely followed the microtopography with the lowest temperatures being measured at the gully bottom and higher temperatures at the gully shoulders (Figure 11a). Bulk Richardson numbers within the transect were larger than in NC 1, and Ri_b were close to the critical Ri_b at the gully bottom (Figure 12). For the case study, the spatial correlation was strong for separation distances between $\pm 25 \text{ m}$ and time-scales $> 4 \text{ min}$ (Figure 13c). We conclude that cold-air pooling occurred, which is supported by the low temperatures throughout the transect, the weak turbulent flow and high spatial correlation of temperatures at the gully bottom.

Lee turbulent mixing was also evident during NC 3. The north shoulder was warmer than the south shoulder and showed a strong temporal variability of temperatures with a peak value of 0.52 K^2 at 95 m (Figure 11). The bulk Richardson number indicated slightly stronger turbulence on the north shoulder (Figure 12). The two-point correlation coefficient of temperature as well as that of wind speed decreased faster at the north shoulder than at the south shoulder for most time-scales, revealing spatial differences sustained in absolute temperature and wind speed (Figure 13c,d). While wind speeds were lower for NC 3 than NC 1, the flow was strong

enough to induce lee turbulent mixing events, which were detected in 37% of observations for NC 3.

A small fluctuation of the downwelling long-wave radiation in combination with a large net radiation balance led to radiative cooling across the entire transect. This is also supported by $R_{\theta_{ij}} \approx 1.0$ for the 64-min time-scale for NC 3 indicating horizontally homogeneous cooling, similar to the results of Thomas (2011) and Pfister *et al.* (2017). Lee turbulence impacted near-surface temperatures only for time-scales smaller 64 min, which was evident by the asymmetry in decay of $R_{\theta_{ij}}$ at the north and south shoulders (Figure 13c). As an example, the 32 min time-scale dropped from 0.9 to 0.4 for separation distances of $\sim 50 \text{ m}$, while this drop did not occur on the south shoulder. Similar to the spatial correlation of temperature, that of wind speed also did not drop significantly for the 64-min time-scale (Figure 13d). We conclude that the spatial correlation of temperatures and wind speeds for NC 3 were influenced by processes occurring on two separate time-scales.

In summary, for NC 3 the entire transect was subject to similar temperature and wind speed dynamics at the 64 min time-scale, while on shorter time-scales ($\leq 32 \text{ min}$) near-surface temperatures and wind speeds were subject to lee turbulent mixing events on the north shoulder.

4.4.3 | Boundary-layer regime of Night Class 4

NC 4 was characterized by a high fluctuation of the downwelling long-wave radiation, stable stratification, and weak winds. One would therefore expect cold-air formation and pooling supported by the limited shear-induced turbulence, but with interruptions caused by the non-stationary downwelling long-wave radiation.

Low wind speeds and turbulent mixing were evident from observations yielding a mean wind speed of 2.3 m/s at the 20 m height of the main tower and associated lower friction velocities at station A15 (0.07 m/s) and station A17 (0.05 m/s). Even though this night class revealed the highest wind directional shear compared to NC 1 and 3, this seemed not to add any turbulence strength near the surface. The net radiation balance was the smallest of all night classes with a mean of -44 W/m^2 , in contrast to the dLRF class featuring a intermediate L_d with a mean of -252 W/m^2 and a large temporal fluctuation of L_d with a mean of 8.5 W/m^2 .

Spatial temperature perturbations were indicative of cold-air drainage and pooling following the microtopography with lowest temperatures at the gully bottom and higher temperatures at the gully shoulders (Figure 11a) and small temporal variability at the gully bottom (Figure 11b). The bulk Richardson numbers were maximum (Figure 12), suggesting a strong buoyant suppression of turbulence, particularly at the gully bottom with Ri_b ranging up to 1.0. We conclude that, due to the reduced vertical mixing as a result of the weak winds, cold-air formation and drainage were the dominant flow and transport processes in spite of the

smaller net radiation balance than NC 1 and 3. Hence, the net radiation balance does not represent near-surface processes well for NC 4.

For NC 4 the effects of lee turbulence were demonstrated by the systematically higher temperatures at the north shoulder in combination with higher temporal temperature perturbations than at the south shoulder (Figure 11). However, the impact of lee turbulence on spatio-temporal temperature perturbations was less for NC 4 than for NC 1 and 3, indicated by less obvious peaks in spatial and temporal temperature perturbations. This result suggests that the minimum wind speed required to induce topographic lee turbulent mixing is lower than the threshold for the weak-wind regime.

The spatial correlation of temperature $R_{\theta_{ij}}$ decreased almost linearly for increasing separation distances with a steeper slope for smaller time-scales (Figure 13e). We speculate that cold-air formation is interrupted by the strong temporal variability of the radiative forcing supported by the large fluctuation of the downwelling long-wave radiation leading to $R_{\theta_{ij}}$ dropping systematically with increasing separation distances and decreasing time-scales. We conclude that cold-air formation and pooling at the gully bottom can persist despite the intermittent downwelling long-wave radiation, while cold-air formation at the shoulders is diminished or interrupted.

For NC 4, the spatial correlation of wind speed $R_{u_{ij}}$ remained ≥ 0.4 for all time-scales and separation distances from -50 m to 80 m and systematically decayed faster for smaller time-scales (Figure 13f). We conclude that atmospheric motions occupied large spatial scales which caused this observed decay for smaller time-scales. We speculate that only one dominant near-surface flow like down-valley cold-air drainage prevails in the case of NC 4 leading to the detected high spatial correlation of the wind speed.

However, for separation distance < -50 m $R_{u_{ij}}$ did drop significantly for all time-scales with the exception of the 64-min time-scale. Similar observations were discussed by Thomas (2011). A high variability of the spatial correlation of wind speeds for long time-scales indicate a location-specific wind microclimate, i.e. systematic semi-stationary motions have a smaller spatial extent. This wind microclimate is most likely induced by nearby obstacles like bushes or trees. Such features can be ruled out for the SCP experiment as topographic and vegetation effects, especially for long time-scales, should not occur as vegetation was short. We think that for NC 4 lee turbulence, which occurred about 70% of the time, interfered with the DTS wind speed measurements by additional cooling of the actively heated fibre due to the enhanced mixing of lee turbulence, which resulted in an overestimation of wind speeds. Hence, different wind speed dynamics were observed at the north shoulder compared to the south shoulder, where lee turbulent mixing was negligible. This difference in wind speed dynamics led to the drop of spatial correlation of wind speed for negative separation distances (Figure 13f). This was less evident for NC 1 and 3, which had strong winds and

thus enhanced mixing to which lee turbulent mixing added less than the weak winds during NC 4. Lee turbulent mixing events and corresponding downward mixing of air from aloft also led to higher temperature at the north shoulder. Hence, lee turbulence also led to the decrease of $R_{\theta_{ij}}$ on the north shoulder compared to the south shoulder for time-scales smaller than 32 min (Figure 13e).

In summary, for NC 4 the weak-wind regime had the strongest impact on atmospheric turbulence and mixing, leading to a high spatial correlation of temperatures and wind speeds across the transect as a result of reduced mixing and enhanced cold-air formation. However, the strong temporal variability of downwelling long-wave radiation acted to suppress cold-air formation particularly at the shoulders. This highlights the importance of L_1 and its fluctuation over the net radiation balance. Lee turbulent mixing was observed, but had a rather small impact on near-surface temperatures.

4.5 | Utility of the night classification scheme and fibre-optic DTS observations

We analyzed the impact of each input variable on the spatio-temporal temperature perturbations. For certain cases, one input variable can supersede the others. For example during statically neutral or unstable stratification, independent of dLRF class and wind regime, we observed no significant spatio-temporal temperature perturbations. Nevertheless, we also found similarities between the input variables. For example, during statically stable conditions and during the strong-wind regime, similarly high temporal temperature perturbations were observed (Figures 6b and 8b). Also spatial temperature perturbations of dLRF class V and of the weak-wind regime are almost identical (Figures 9a and 8a). We conclude that in these regimes the input variables depend on each other, as can be expected from the surface energy balance (cf. section 2.2). The eddy diffusivity for the sensible heat flux depends on the friction velocity, which is a function of the wind speed and thus is influenced by the wind regime. The sensible heat flux is also determined by the vertical temperature gradient, i.e. static stability. Further, the sensible heat flux is a response of the surface and surface layers to the downwelling long-wave. Hence, the input variables cannot be interpreted as independent, but as major interdependent forcings.

The proposed night classification scheme successfully divided the nocturnal boundary layer into physically meaningful regimes. The employed DTS technique with its spatially continuous observations at high resolution gave unique insights into the near-surface temperatures and wind speeds, which even a dense network of single-point measurements cannot observe in such detail. For example, microtopography-induced lee turbulence was detected by the sonic anemometer network of the SCP experiment (Mahrt, 2017a), but only with the night classification scheme in combination with the observations from DTS could we quantify

the impact of lee turbulence on spatio-temporal temperature perturbations depending on wind regime, dLRF class, and static stability. Similar analyses could be performed for a variety of motions characteristic of the nocturnal boundary layer.

The high spatio-temporal variability of Ri_b within the DTS transect revealed in a unique fashion the impact of microtopography on turbulent flows and fluxes. This finding emphasizes the ambiguousness of a unique Ri_b as a local stability indicator, which was also demonstrated by van Hooijdonk *et al.* (2015). They found an identical value of the critical gradient Richardson number for contrasting conditions, namely a very stable, shallow boundary layer at a low observational level and a deeper, more turbulent boundary layer at a greater height. Based on our findings we can add that Ri_b strongly varies with horizontal position even in gently undulating terrain such as a shallow gully.

Thomas (2011) showed the invalidity of Taylor's hypothesis by analyzing the spatial correlation of temperature and of wind speeds for a network of ultrasonic anemometers in the sub-canopy of a dense forest with separation distances between 20 and 230 m. They found fundamental differences in the space-time structure of the motions dominating the variability of the sub-canopy wind and temperature fields. So, no simple symmetry between temporal and spatial temperature gradients can be expected when considering the domain-averaged flow. This renders Taylor's hypothesis invalid for computing meaningful horizontal advection without dense spatial observation. Our study offered spatial continuous data and, similar to the study of Mahrt *et al.* (2009), we can arbitrarily define a horizontal length-scale L_e , where $R_{\theta_{ij}}$ decreased to $1/(e - 1)$. L_e increased systematically with increasing time-scale, but the increase was different between the night classes. When a linear fit between time-scale and L_e is applied, we derive a velocity scale, which represents the mean advective velocity for temperature. This advective velocity might only roughly describe the systematic increase of the horizontal length-scale with increasing time-scale, especially because we are not considering the wind direction with respect to the DTS orientation. The advective velocity was similar to the mean wind speed at A15 for NC 1 and NC 3, but for NC 4 the advective velocity of 3.5 m/s was more than twice as high as the mean wind speed with 1.5 m/s. Hence, we cannot assume that the temperature perturbations are transported with the mean wind. We conclude that Taylor's hypothesis is invalid for NC 4.

5 | CONCLUSION

In this study we propose a classification scheme for the nocturnal atmospheric boundary layer constructed from three input variables: static stability, wind regime and downwelling long-wave radiative forcing. This night classification scheme was evaluated using field observations over gently varying terrain of a shallow valley during the Shallow Cold Pool

(SCP) experiment. This field campaign offered a unique set of measurements from an extensive network of 19 ultrasonic anemometers and a cross-valley fibre-optic transect of air temperatures and wind speeds from actively heated distributed temperature sensing (DTS) at an unprecedented spatial and temporal resolution.

Overall we arrive at the following conclusions:

- The downwelling long-wave radiation and its fluctuation are the driving variables for near-surface temperatures rather than the net radiation balance. The net radiative balance is determined by the difference in downwelling and upwelling long-wave radiation, i.e. the radiative temperature of the sky and that of the surface times its emissivity. However, the upwelling long-wave radiation is a function of the surface temperature and thus a near-surface response rather than a forcing. To avoid self-correlation, it is essential to define the forcing of the near-surface temperature by a variable which does not include near-surface temperature itself. As a prominent example, NC 4 with the smallest net radiation balance showed the highest amount of cold-air pooling. Hence, we contend that L_1 and its fluctuation is the relevant forcing.
- Spatio-temporal temperature perturbations respond to each of the three input variables, but the input variables themselves are interdependent with a varying degree of coupling. Spatio-temporal temperature perturbations only occur under statically stable conditions and vanish for statically neutral or unstable conditions. The downwelling long-wave radiation limits the magnitude of spatio-temporal temperature perturbations, while the wind regime impacts their spatial distribution.
- The night classification scheme distinguishes between specific and inherently different boundary-layer regimes. Our analyses focused on discussing the dynamics of three most prevalent night classes for SCP:
 - NC 1: mostly dynamically forced boundary layer with a limited degree of cold-air formation;
 - NC 3: cold-air drainage and pooling competing with strong shear-induced mixing and lee turbulence caused by topography;
 - NC 4: cold-air drainage and pooling for the weak-wind regime competing with lee turbulence and fluctuation of downwelling long-wave radiation.
- Our night classification scheme can be adapted to any field study as long as long-wave radiation is measured at screen level height, vertical temperature measurements are taken at two levels and three-dimensional wind speeds are measured a few metres agl. This night classification scheme should prove to be useful for defining physically meaningful nocturnal boundary layers in other studies.
- The DTS technique provided unique measurements for the computation of the bulk Richardson number, Ri_b , in a spatially continuous fashion. Ri_b was found to not only

vary with height, but also with horizontal position and microtopography at the field site. Therefore, the utility of Ri_b to determine boundary-layer regimes from a limited number of sensors at a single location is questionable even in the case of gentle spatial heterogeneity.

- Our analyses confirmed the invalidity of Taylor's hypothesis, specifically during NC 4.

Future investigations of the nocturnal boundary layer should therefore include spatially explicit and – if possible – continuous observations from a variety of sensors and sensor networks to better understand the spatial variability of flow, temperature and transport for the identification of boundary-layer regimes and for finding suitable forcing mechanisms for transport under these conditions.

ACKNOWLEDGEMENTS

Important comments from the unknown reviewers are greatly appreciated and helped improve the manuscript substantially. This project received support from awards AGS-1115011, AGS-1614345, and AGS-0955444 by the National Science Foundation and contracts W911NF-10-1-0361 and W911NF-09-1-0271 by the Army Research Office. We acknowledge the Earth Observing Laboratory of the National Center for Atmospheric Research for collecting the sonic anemometer measurements for the Shallow Cold Pool experiment (https://www.eol.ucar.edu/field_projects/scp and <https://data.eol.ucar.edu/dataset/385.003>; accessed 2 March 2017).

ORCID

Lena Pfister  <http://orcid.org/0000-0002-6645-4326>

Karl Lapo  <https://orcid.org/0000-0002-4637-2032>

Chadi Sayde  <https://orcid.org/0000-0002-4802-252X>

John Selker  <https://orcid.org/0000-0001-9751-6094>

Larry Mahrt  <http://orcid.org/0000-0002-0212-3165>

Christoph K. Thomas  <https://orcid.org/0000-0003-2277-6013>

REFERENCES

- Acevedo, O.C., Mahrt, L., Puhales, F.S., Costa, F.D., Medeiros, L.E. and Degrazia, G.A. (2016) Contrasting structures between the decoupled and coupled states of the stable boundary layer. *Quarterly Journal of the Royal Meteorological Society*, 142, 693–702.
- Baas, P., van de Wiel, B.J.H., van der Linden, S.J.A. and Bosveld, F.C. (2018) From near-neutral to strongly stratified: adequately modelling the clear-sky nocturnal boundary layer at Cabauw. *Boundary-Layer Meteorology*, 166, 217–238.
- Derbyshire, S.H. (1999) Stable boundary-layer modelling: established approaches and beyond. *Boundary-Layer Meteorology*, 90, 423–446.
- Dürr, B. and Philipona, R. (2004) Automatic cloud amount detection by surface longwave downward radiation measurements. *Journal of Geophysical Research, Atmospheres*, 109, D05201.
- Edwards, J.M. (2009) Radiative processes in the stable boundary layer: Part II. The development of the nocturnal boundary layer. *Boundary-Layer Meteorology*, 131, 127–146.
- Foken, T. (2017a) *Energy Balance at the Earth's Surface, Section 1.4 in Micrometeorology*. Berlin.
- Foken, T. (2017b) *Flux-gradient Similarity, Section 2.3 in Micrometeorology*. Berlin.
- Galperin, B., Sukoriansky, S. and Anderson, P.S. (2007) On the critical Richardson number in stably stratified turbulence. *Atmospheric Science Letters*, 8, 65–69.
- Holtstag, A.A.M. and De Bruin, H.A.R. (1988) Applied modeling of the night-time surface energy balance over land. *Journal of Applied Meteorology*, 27, 689–704.
- Holtstag, A.A.M. and Nieuwstadt, F.T.M. (1986) Scaling the atmospheric boundary layer. *Boundary-Layer Meteorology*, 36, 201–209.
- Howell, J.F. and Mahrt, L. (1997) Multiresolution flux decomposition. *Boundary-Layer Meteorology*, 83, 117–137.
- Mahrt, L. (1998) Nocturnal boundary-layer regimes. *Boundary-Layer Meteorology*, 88, 255–278.
- Mahrt, L. (2017a) Lee mixing and nocturnal structure over gentle topography. *Journal of the Atmospheric Sciences*, 74, 1989–1999.
- Mahrt, L. (2017b) Stably stratified flow in a shallow valley. *Boundary-Layer Meteorology*, 162, 1–20.
- Mahrt, L. and Heald, R. (2015) Common marginal cold pools. *Journal of Applied Meteorology and Climatology*, 54, 339–351.
- Mahrt, L., Richardson, S., Stauffer, D. and Seaman, N. (2014a) Nocturnal wind-directional shear in complex terrain. *Quarterly Journal of the Royal Meteorological Society*, 140, 2393–2400.
- Mahrt, L., Sun, J., Oncley, S.P. and Horst, T.W. (2014b) Transient cold air drainage down a shallow valley. *Journal of the Atmospheric Sciences*, 71, 2534–2544.
- Mahrt, L., Sun, J. and Stauffer, D. (2015) Dependence of turbulent velocities on wind speed and stratification. *Boundary-Layer Meteorology*, 155, 55–71.
- Mahrt, L., Thomas, C.K. and Prueger, J.H. (2009) Space-time structure of mesoscale motions in the stable boundary layer. *Quarterly Journal of the Royal Meteorological Society*, 135, 67–75.
- Marty, C. and Philipona, R. (2000) The clear-sky index to separate clear-sky from cloudy-sky situations in climate research. *Geophysical Research Letters*, 27, 2649–2652. <https://doi.org/10.1029/2000GL011743>.
- Meybeck, M., Green, P. and Vörösmarty, C. (2001) A new typology for mountains and other relief classes. *Mountain Research and Development*, 21, 34–45.
- Monahan, A.H., Rees, T., He, Y. and McFarlane, N. (2015) Multiple regimes of wind, stratification, and turbulence in the stable boundary layer. *Journal of the Atmospheric Sciences*, 72, 3178–3198.
- Paltridge, G.W. (1974) Global cloud cover and Earth surface temperature. *Journal of the Atmospheric Sciences*, 31, 1571–1576.
- Pfister, L., Sigmund, A., Olesch, J. and Thomas, C.K. (2017) Nocturnal near-surface temperature, but not flow dynamics, can be predicted by microtopography in a mid-range mountain valley. *Boundary-Layer Meteorology*, 165, 333–348.
- Sayde, C., Thomas, C.K., Wagner, J. and Selker, J. (2015) High-resolution wind speed measurements using actively heated fiber optics. *Geophysical Research Letters*, 42, 10064–10073.
- Selker, J.S., Thévenaz, L., Huwald, H., Mallet, A., Luxemburg, W., van de Giesen, N., Stejskal, M., Zeman, J., Westhoff, M. and Parlange, M.B. (2006) Distributed fiber-optic temperature sensing for hydrologic systems. *Water Resources Research*, 42(12). <https://doi.org/10.1029/2006WR005326>.
- Stull, R.B. (2000) *Katabatic wind, section 10.5.3 pp. 209–210*. Pacific Grove, CA.
- Sun, J., Mahrt, L., Banta, R.M. and Pichugina, Y.L. (2012) Turbulence regimes and turbulence intermittency in the stable boundary layer during CASES-99. *Journal of the Atmospheric Sciences*, 69, 338–351.
- Sun, J., Mahrt, L., Nappo, C. and Lenschow, D.H. (2015) Wind and temperature oscillations generated by wave turbulence interactions in the stably stratified boundary layer. *Journal of the Atmospheric Sciences*, 72, 1484–1503.
- Thomas, C.K. (2011) Variability of sub-canopy flow, temperature, and horizontal advection in moderately complex terrain. *Boundary-Layer Meteorology*, 139, 61–81.
- Thomas, C.K., Kennedy, A.M., Selker, J.S., Moretti, A., Schroth, M.H., Smoot, A.R., Tufillaro, N.B. and Zeeman, M.J. (2012) High-resolution fibre-optic temperature sensing: a new tool to study the two-dimensional structure of atmospheric surface-layer flow. *Boundary-Layer Meteorology*, 142, 177–192.
- Van de Wiel, B.J.H., Moene, A.F., Jonker, H.J.J., Baas, P., Basu, S., Donda, J.M.M., Sun, J. and Holtstag, A.A.M. (2012) The minimum wind speed for sustainable turbulence in the nocturnal boundary layer. *Journal of the Atmospheric Sciences*, 69, 3116–3127.

- van der Linden, S.J.A., Baas, P., Antoon van Hooft, J., van Hooijdonk, I.G.S., Bosveld, F.C. and van de Wiel, B.J.H. (2017) Local characteristics of the nocturnal boundary layer in response to external pressure forcing. *Journal of Applied Meteorology and Climatology*, 56, 3035–3047.
- van Hooijdonk, I.G.S., Donda, J.M.M., Clercx, H.J.H., Bosveld, F.C. and van de Wiel, B.J.H. (2015) Shear capacity as prognostic for nocturnal boundary-layer regimes. *Journal of Applied Meteorology*, 72, 1518–1532.
- Zeeman, M.J., Selker, J.S. and Thomas, C.K. (2015) Near-surface motion in the nocturnal, stable boundary layer observed with fibre-optic distributed temperature sensing. *Boundary-Layer Meteorology*, 154, 189–205.

How to cite this article: Pfister L, Lapo K, Sayde C, Selker J, Mahrt L, Thomas CK. Classifying the nocturnal atmospheric boundary layer into temperature and flow regimes. *Q J R Meteorol Soc.* 2019;145:1515–1534. <https://doi.org/10.1002/qj.3508>

APPENDIX

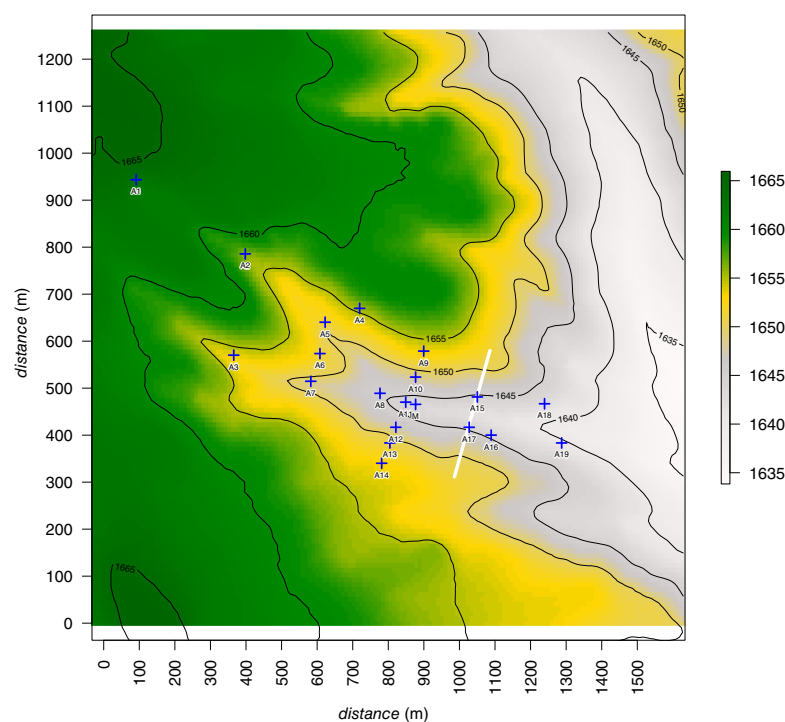


FIGURE A1 Elevation of field site in metres above MSL with the position of each ultrasonic anemometer station (blue crosses) and the DTS transect (white line) [Colour figure can be viewed at wileyonlinelibrary.com]

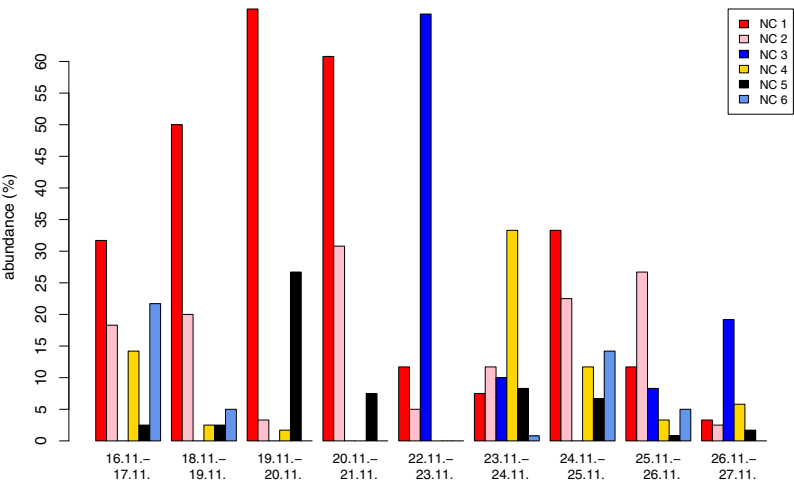


FIGURE A2 Abundance of the six most abundant night classes [Colour figure can be viewed at [wileyonlinelibrary.com](#)]

TABLE A1 Ten most abundant night classes derived by the night classification scheme

Night class	Wind regime	dLRF class	Static stability	Abundance (%)	Expected boundary layer
NC 1	Strong	III	Stable	30.9	Intermittent cold-air formation competing with turbulence of wind regime
NC 2	Strong	IV	Stable	15.6	Turbulence of wind regime dominates; cold-air formation is damped due to high fluctuation
NC 3	Strong	V	Stable	11.7	Cold-air dynamics competing with turbulence of wind regime
NC 4	Weak	IV	Stable	8.1	Intermittent cold-air formation due to dLRF class, but cold-air dynamics will dominate due to low turbulence of wind regime
NC 5	Weak	III	Stable	6.3	Similar to NC 4, but with stronger inversion and higher spatial temperature perturbations
NC 6	Strong	II	Stable	5.2	Vanishing temperature perturbations, dominating wind regime, almost no cold-air formation
NC 7	Weak	V	Stable	4.9	Cold-air dynamics dominate, strong inversion
NC 8	Strong	I	Stable	3.7	Depending on wind speed near well-mixed boundary layer
NC 9	Strong	VI	Stable	3.6	As NC 3, but with less strong inversions
NC 10	Weak	VI	Stable	3.0	As NC 4, but with less strong inversions

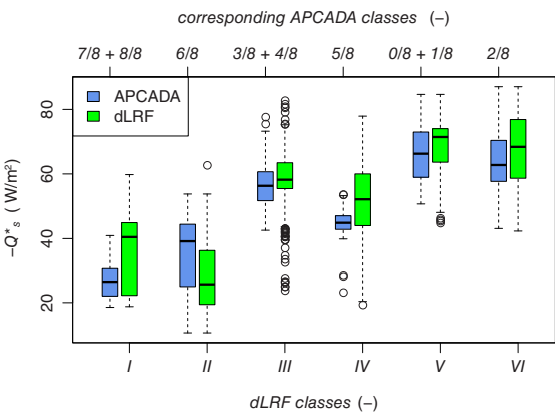


FIGURE A3 Comparison of nocturnal net radiation balance of APCADA classes and dLRF classes during DTS measurement period from 16 November to 27 November [Colour figure can be viewed at [wileyonlinelibrary.com](#)]

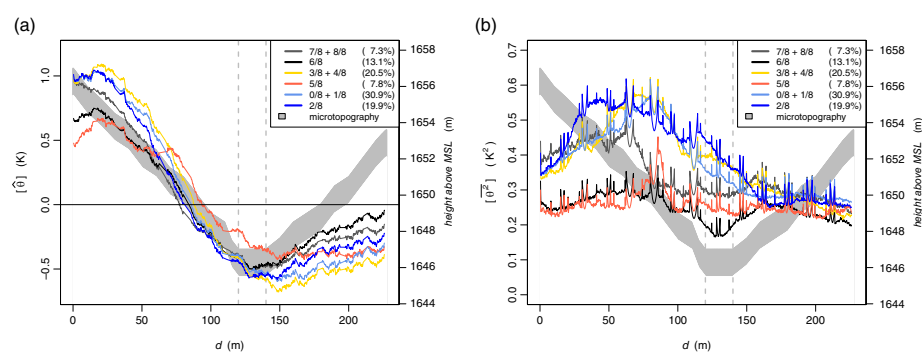


FIGURE A4 (a) Spatial ($[\hat{\theta}]$) and (b) temporal ($[\hat{\theta}^2]$) temperature perturbation, ensemble averaged for each APCADA class. Abundance is given as a percentage of complete night-time data [Colour figure can be viewed at wileyonlinelibrary.com]

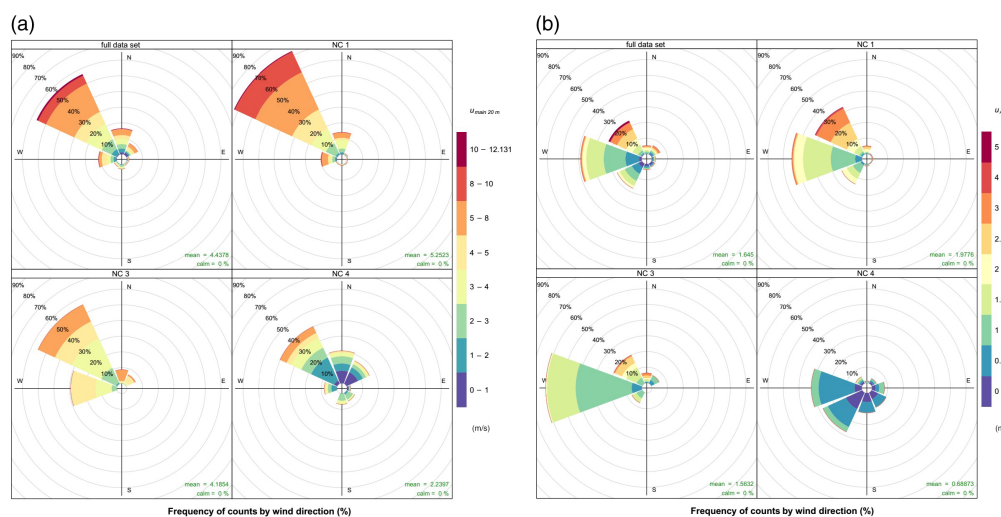


FIGURE A5 Wind roses at (a) the 20 m height at the main tower and (b) A17 at the gully bottom for each night class [Colour figure can be viewed at wileyonlinelibrary.com]

B Small-Scale Variability in the Nocturnal Boundary Layer

Boundary-Layer Meteorology (2020) 174:81–98
<https://doi.org/10.1007/s10546-019-00476-x>

RESEARCH ARTICLE



Small-Scale Variability in the Nocturnal Boundary Layer

L. Mahrt¹ · Lena Pfister² · Christoph K. Thomas²

Received: 15 April 2019 / Accepted: 12 August 2019 / Published online: 17 September 2019
© The Author(s) 2019

Abstract

Nocturnal variations of temperature and wind are examined at three contrasting sites. After the early evening period of rapid cooling, the magnitude of the variations of temperature on a time scale of 10 min to an hour often become larger than the corresponding temperature change due to the nocturnal trend. These shorter-term temperature variations are forced by wave-like motions and more complex modes. Observations from a network of stations across a shallow valley at one of the sites are analyzed in more detail. Typically, decreasing wind speed corresponds to less mixing and lower temperature at the surface followed by increasing wind speed, increased mixing, and higher temperatures. The flow may continue to switch back and forth between these two states for much of the night. These non-stationary motions interact with motions induced by the gentle local topography, leading to intermittent local drainage flows, transient cold pools, and both propagating and semi-stationary microfronts.

Keywords Microfronts · Nocturnal boundary layer · Non-stationarity · Stratified turbulence · Submeso

1 Introduction

The stable boundary layer is often partitioned into a weakly stable regime of significant turbulence intensity and a very stable regime with lower turbulence intensity, which is often intermittent. However, Monahan et al. (2015) finds that traditional stability parameters alone are inadequate for partitioning the stable boundary layer. The causes of the variability of the turbulence in the more stable regime are not precisely known, although some of the variability is attributed to non-turbulent submeso motions (Acevedo et al. 2014) that include microfronts and wind direction shifts (Lang et al. 2018), internal gravity waves (Sun et al. 2015b), nearly horizontal two-dimensional modes (Mortarini et al. 2016), locally generated large-scale structures (Ansorge and Mellado 2014), and more complex modes. These motions collectively perturb the local flow (e.g., Monti et al. 2002; Sun et al. 2015a; Vercauteren et al. 2016; Cava et al. 2019a).

✉ L. Mahrt
mahrt@nwra.com

¹ NorthWest Research Associates, 2171 NW Kari Pl, Corvallis, OR 97330, USA

² Micrometeorology Group, University of Bayreuth, 95540 Bayreuth, Germany

Intermittent bursts of turbulence and associated warming are common and occur on a variety of time scales in the stable boundary layer (e.g., Nappo 1991; Ohya et al. 2008; Tampieri et al. 2015; Burman et al. 2018), although their relation to the non-turbulent motions is not always clear. The very stable boundary layer also includes short periods of particularly low turbulence intensity and lower temperatures that may last minutes (Zeeman et al. 2015) or tens of minutes (Mahrt 2017c). These micro cold events are sometimes well defined with sharp edges and arrive as microfronts (Zeeman et al. 2015; Kang et al. 2015; Lang et al. 2018; Grudzielanek and Cermak 2018). Cold air can originate over colder surfaces related to even weak heterogeneity of the soil and vegetation (Van de Wiel et al. 2002) or may be generated in cloud-free areas embedded within a general cloud cover and then advect over adjacent surfaces.

Vercauteren et al. (2016, 2019) find that stable conditions can be partitioned into subclasses based on whether or not submeso motions are significant and generate significant turbulence. Stable conditions can also be subdivided based on whether or not the submeso horizontal motions are separated in scale from the largest turbulence eddies (partial spectral gap). Without a clear separation of scales, the turbulence may not be able to maintain equilibrium with the changing submeso flow. Petenko et al. (2019) finds a general absence of organized temperature variations in thin very stable boundary layers except for sporadic elevated bursts of turbulence. However, in the deeper, less stable boundary layer, they find two subclasses, one with significant organized submeso variation of temperature and one without such structure. Acevedo et al. (2014), Vercauteren et al. (2019), and others have emphasized that the nature of the submeso motions varies between sites. The unpredictable variation of temperature and wind speed and direction on small time scales and the site differences are of considerable practical interest with respect to dispersion, frost occurrence and fog forecasting (Izett et al. 2018).

Momen and Bou-Zeid (2017) explicitly identifies the role of the time scale of the forcing through numerical examination of the response of the turbulence to a non-stationary horizontal pressure gradient. When the time scale of the forcing by the perturbation pressure gradient is large compared to the characteristic time scale of the turbulence (a scale gap), the turbulence maintains approximate equilibrium with the forcing. In contrast, the turbulence does not maintain equilibrium when the forcing time scale is the same order of magnitude as the turbulence time scale (no scale gap).

Mortarini et al. (2017) details the potential complexity of nocturnal boundary layers due partly to the interaction between the turbulence and a variety of submeso motions as well as circulations driven by surface heterogeneity and associated low-level jets. Cava et al. (2019b) examines formation of a low-level jet that follows the collapse of the turbulence. Subsequently, the low-level jet generates mixing below the wind maximum. Intermittent turbulence and associated warm and cold events in the stable nocturnal boundary layer can be induced by even modest microtopography (Pfister et al. 2017; Mahrt 2017c). Guerra et al. (2018) found that the microtopography induces horizontal variation of temperature that systematically increases with decreasing wind speed. Based on fine-scale measurements of the horizontal structure, Pfister et al. (2019) found that spatial and temporal variations of temperature on horizontal scales of a few 100 m or less in gentle topography tended to organize into several prototype regimes: windy with limited formation of cold air; windy but with cold air drainage and pooling modulated by large shear-induced mixing and lee turbulence; and low wind speeds with more robust cold-air drainage and cold pool formation. This organization was formulated in terms of the general wind speed, stratification, and downward longwave radiation. These forcing variables were found to be interdependent but not to the extent that one of them could be eliminated.

To examine these interactions, measurements from three sites are investigated. After describing the datasets, we contrast the statistics of the non-turbulent changes of temperature between the sites. We then focus on a case-study night that reveals the interaction between the impact of weak local topography and transient motions.

2 Observations and Analysis

The Shallow Cold Pool (SCP) Experiment was conducted over semi-arid grasslands in north-east Colorado, USA, from 1 October to 1 December 2012 (https://www.eol.ucar.edu/field_projects/scp). See Mahrt and Thomas (2016) for more information on this site. The main valley is relatively small, roughly 12 m deep and 270 m across (Fig. 7, Sect. 5.2). The width of the valley floor averages about 5 m with an average down-valley slope of 2%, increasing to about 3% at the upper end of the valley. The side slopes of the valley are on the order of 10% or less. We analyze the 1-m sonic anemometer observations from 20 stations and from the main tower at 0.5, 1, 2, 3, 4, 5, 10, and 20 m. The SCP measurements include fiber-optic distributed temperature sensing (DTS) (Thomas et al. 2012; Zeeman et al. 2015; Pfister et al. 2017, 2019), which provides fine horizontal resolution of 0.3 m and time resolution of 5 s at 0.5, 1, and 2 m above the ground surface along a 250-m cross-valley transect. Times are expressed in local standard time (LST = UTC − 7 h). For examination of the time structure of events, decimal time is used.

The second field campaign contains measurements from sonic anemometer measurements collected in North Park, Colorado, USA, in 2002, during the Fluxes Over a Snow Surface II field program (*FLOSSII*, <http://www.eol.ucar.edu/isf/projects/FLOSSII/>) within the North Park Basin (Mahrt and Thomas 2016). On average, the valley floor is about 30 km wide with valley sidewalls of 1000 m over a horizontal width of about 7 km. The basin is approximately 50 km from south to north. The surface consists of matted grass, sometimes with a shallow snow cover. The roughness length for this site is quite small, less than 1 mm with snow cover. Scattered short brush occurs beginning 100–200 m upwind with respect to the prevailing southerly flow.

The third set of observations were collected during the CASES-99 (Cooperative Atmospheric Surface Exchange Study) over grassland in south-central Kansas, USA (Poulos et al. 2001; Sun et al. 2002). This dataset is only of 1-month duration but includes a 60-m tower and has become a standard for analysis of the nocturnal boundary layer. We analyze sonic anemometer measurements taken at 1.5 m for the first part of the program and then moved to 0.5 m for the remainder of the field program.

2.1 Averaging

Our analysis approach is detailed in Mahrt and Thomas (2016). The flow is partitioned as

$$\phi = \phi' + \bar{\phi}, \quad (1)$$

where the overbar designates a time average over a window of width τ , chosen here to be 1 min. ϕ' is the deviation from such an average. ϕ is potential temperature or one of the velocity components. The heat flux is computed as $w'\theta'$, where w' is the perturbation vertical velocity. The wind speed is determined as

$$U \equiv \sqrt{\bar{u}^2 + \bar{v}^2}. \quad (2)$$

We also compute the standard deviation of the vertical velocity fluctuation within the averaging window, σ_w , as a measure of the turbulence intensity.

A local potential temperature at each station is defined with respect to the base of the tower on the valley floor by using the dry adiabatic lapse rate between the absolute elevation of the base of the tower (Z_{base}) and the absolute elevation of the 1-m level at a given station (Z) such that the potential temperature at a given station is

$$\theta \equiv T + 0.01(Z - Z_{\text{base}}), \quad (3)$$

with height in m. Station A1 is the highest station where the 1 m level is 20 m above the base of the tower. For time series, θ is expressed in °C.

3 Short-Term Variability Versus Nocturnal Trend

We begin with a simple statistical assessment of time variability of temperature in the nocturnal boundary layer. The temperature change, $\delta_t(\theta)$, is defined to be the difference of θ between two adjacent half window means with a total window width of τ_F . If the averages for each half window are considered to represent the midpoint of their respective half window, then $\delta_t\theta$ (K) estimates the variation of θ over $\tau_F/2$ because $\tau_F/2$ is the distance between the midpoints of two half windows. Nominally, $\tau_F/2$ is chosen to be 1 h. This window sequentially moves through the record 1 min at a time, corresponding to considerable overlap of the windows. We average $\delta_t\theta$ over all windows in a given field program to compute $[\delta_t\theta]$. For each window, we require that $\{\overline{w'\theta'}\} < -0.003 \text{ Km s}^{-1}$ to eliminate unstable and near-neutral conditions where the heat flux may be too small to adequately estimate. Curley brackets refer to averaging over the window. We also require that $\{R_{\text{net}}\} < -20 \text{ W m}^{-2}$. This requirement removes overcast conditions and also removes most of the rapid cooling period during the evening transition when the positive net radiation decreases with time and reverses to negative net radiation (Mahrt 2017b). With this condition, there is no need to apply time of day restrictions.

As the window moves sequentially through the record, it samples structures with random phase and variable sign of $\delta_t\theta$. An estimate of the contribution of the nocturnal trend to $\delta_t\theta$ is constructed by averaging $\delta_t\theta$ (sign retained) over all of the windows such that $[\delta_t\theta]$ becomes an estimate of the average nocturnal temperature decrease over the time interval $\tau_F/2$. This averaging filters out small-scale time variability, which has no sign preference. Averaging the absolute values to compute $[\text{abs}(\delta_t\theta)]$ provides an estimate of the total temperature variation that includes both the systematic nocturnal variation and the smaller-scale variations that contain both positive and negative values.

A measure of the smaller-scale temperature variations can be expressed as

$$[\delta_t\theta]_{sm} \equiv [\text{abs}(\delta_t\theta)] - [\delta_t\theta], \quad (4)$$

where again $[\text{abs}(\delta_t\theta)]$ is the average of the total variation and $[\delta_t\theta]$ is the temperature difference due to the nocturnal trend, hereafter referred to as simply the nocturnal trend. We refer to $[\delta_t\theta]_{sm}$ as the small-scale (submeso) temperature variability, which is the variability not explained by the nocturnal trend.

3.1 Differences Between the Small-Scale Variations and the Nocturnal Trend

We now examine the dependence of the total variation, $[\text{abs}(\delta_t\theta)]$, on the window width τ_F . For station A1 outside the valley at the SCP site, $[\text{abs}(\delta_t\theta)]$ increases with increasing $\tau_F/2$ (black, Fig. 1) due to the capture of a larger range of non-stationary motions. $[\text{abs}(\delta_t\theta)]$ is

Fig. 1 Dependence of cooling on $\tau_F/2$ at Station A1 outside the valley at the SCP site. $\tau_F/2$ is the width over which temperature changes are estimated. The magnitude of the total temperature variation, $[\text{abs}(\delta_t\theta)]$ (K, black), includes contributions from both the nocturnal trend and the smaller-scale variations. $[\delta_t\theta]$ (K, red) is an estimate of the average nocturnal trend

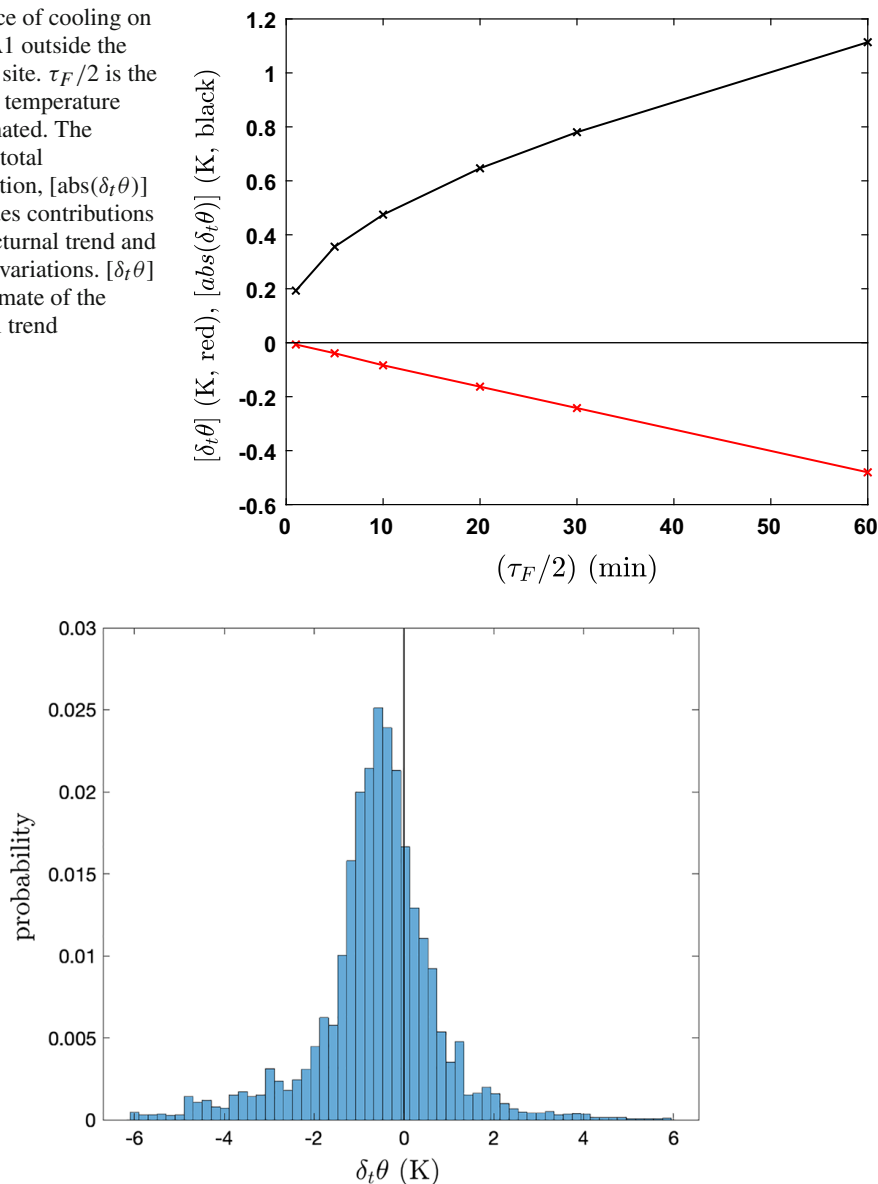


Fig. 2 The frequency distribution of $\delta_t\theta$ at SCP station A1 outside of the valley for $\tau_F/2 = 60$ min

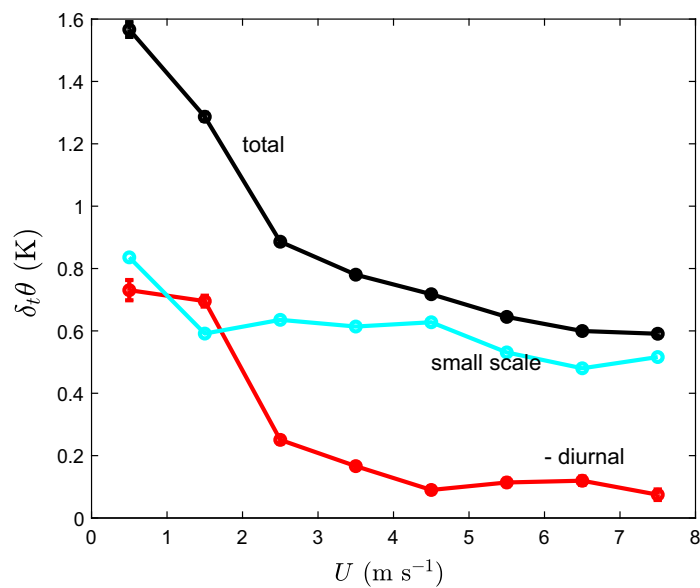
a little more than 1 K for $\tau_F/2 = 1$ h. Because the temperature difference $[\delta_t\theta]$ increases approximately linearly with $\tau_F/2$, the cooling rate due to the nocturnal trend ($[\delta_t\theta]/(\tau_F/2)$) is approximately independent of $\tau_F/2$. The effect of the choice of the window width on the above statistics is similar to that at the FLOSSII and CASES-99 sites.

The frequency distribution of $\delta_t\theta$ for $\tau_F/2 = 60$ min at the SCP station A1 (Fig. 2) indicates that the total variation $\delta_t\theta$ is a combination of the submeso temperature variations and an approximate -0.5 K shift due to the nocturnal trend. The frequency distribution indicates that the magnitude of $\delta_t\theta$ for individual sampling windows is often large compared to the magnitude of the nocturnal trend. The average nocturnal trend over a 1-h period (Table 1) is about 0.5 K h at the FLOSSII and SCP sites and is 0.6 K at the CASES-99 site. Recall that these results include windy nights and partly cloudy conditions, which reduce the averaged nocturnal cooling compared to clear nights with low wind speeds. At the FLOSSII

Table 1 Site, the averaged temperature change due to the nocturnal trend, $[\delta_t\theta]$, the averaged absolute temperature change $[\text{abs}(\delta_t\theta)]$, and the estimate of the small-scale time variability of temperature, $[\delta_t\theta]_{sm}$

Site	$[\delta_t\theta]$	$[\text{abs}(\delta_t\theta)]$	$[\delta_t\theta]_{sm}$	P (%)
FLOSSII	-0.50	1.12	0.61	34
SCP A1	-0.48	1.11	0.63	35
SCP A9	-0.48	1.12	0.63	35
SCP A11	-0.50	1.23	0.73	37
CASES-99	-0.60	1.06	0.46	27

Temperature differences are estimated over the time interval $\tau_F/2 = 60$ min. P is the percent of the values of $\delta_t\theta$ that are positive, counter to the sign of the nocturnal trend

**Fig. 3** The 1-m temperature difference $\delta_t\theta$ at the FLOSSII site for $\tau_F/2 = 60$ min. The dependence of the total temperature variation ($[\text{abs}(\delta_t\theta)]$, black), the negative of the nocturnal trend ($-\delta_t\theta$, red), and the inferred small-scale time variability of temperature ($[\delta_t\theta]_{sm}$, cyan) on the wind speed, U . Here, the operator $[\]$ is an average over all of the samples for the entire field program for a given interval (bin) of the wind speed

and SCP sites, the submeso temperature variation, $[\delta_t\theta]_{sm}$, averages about 30% more than the magnitude of the nocturnal trend, depending on the station. $[\delta_t\theta]_{sm}$ is a little smaller than the magnitude of the nocturnal trend at the CASES-99 site probably because of flatter terrain.

We define P as the probability of $\delta_t\theta > 0$; that is, the probability that the 1-h temperature change is opposite to the expected nocturnal trend. With no small-scale variability and only nocturnal trend, P is small because the nocturnal trend is generally negative. The probability P may approach 50% when the magnitude of the nocturnal trend is negligible compared to the small-scale variability because the small-scale temperature variability shows no sign preference. The probability P is about 35% for both the FLOSSII and SCP sites (Table 1), implying that the magnitude of the small-scale temperature variability is important; P is only 27% for the CASES-99 site where the intensity of the submeso motions is lower.

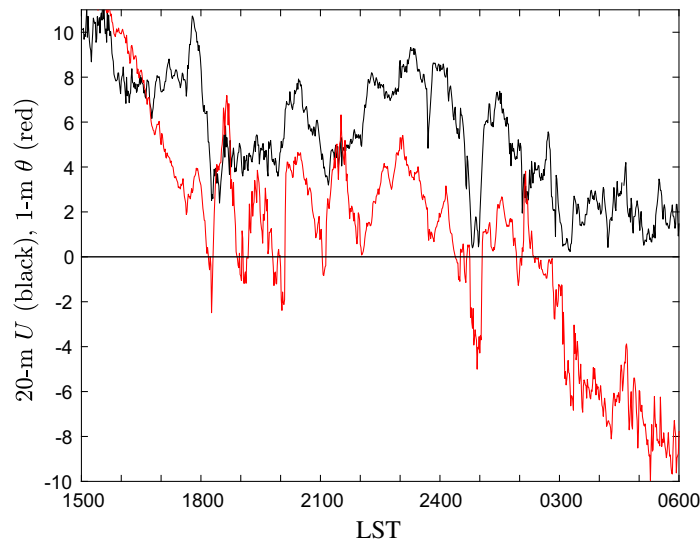


Fig. 4 Observations at the tower for night 24–25 November in the SCP field program. Shown are the 20-m wind speed U (m s^{-1} , black) and θ at 1 m on the tower ($^{\circ}\text{C}$, red) relative to the night-averaged temperature

3.2 Dependence on Wind Speed

The magnitude of the nocturnal temperature trend is normally expected to be larger with low wind speeds and clear skies. However, the dependence of the temperature variation on the wind speed, net radiative cooling, and stratification is complicated at the SCP site because the net radiative cooling, on average, increases with increasing wind speed. The very lowest wind speeds, less than 1 m s^{-1} , are often associated with cloudy conditions. Clear skies and significant radiative cooling induce drainage/down-valley flows and thus prevent very low wind speeds. In addition, the relationship between the wind and stratification at the SCP site depends partly on the wind direction through horizontal temperature advection (Mahrt 2017a).

The temperature changes at the FLOSSII site depend more systematically on the wind speed U . As expected, the magnitude of the nocturnal trend (Fig. 3a, red) decreases systematically with increasing U . The small-scale time variability of temperature, $[\delta_t \theta]_{sm}$ (cyan), is more independent of U so that the small-scale temperature variability becomes relatively more important for larger U . One might have thought that the greater mixing with large U would reduce $[\delta_t \theta]_{sm}$. However, horizontal temperature variations more effectively generate local time variations with larger advecting velocity.

The overall statistics for the FLOSSII site (Table 1) are significantly influenced by the frequent low wind speeds $< 2 \text{ m s}^{-1}$ at the FLOSSII site where the magnitude of the nocturnal trend increases to values comparable to those for $[\delta_t \theta]_{sm}$ (Fig. 3). The plotted error bars in Fig. 3 are generally too small to be seen, although the standard error neglects the large dependence between samples and might seriously underestimate the uncertainty. $[\delta_t \theta]_{sm}$ also appears to depend significantly on the stratification and wind direction, currently under investigation.

4 Night of 24–25 November (DOY 329)

The above statistics indicate that the magnitude of the small-scale non-turbulent variations of temperature are often large compared to the magnitude of the nocturnal trend and motivate

the examination of individual cases that contribute to such variability. We concentrate on the SCP observations where the spatial coverage is extensive. We proceed with a case study based on the night of 24–25 November in the SCP field program, which includes multiple flow regimes (Fig. 4) and is one of the nights with fiber-optic DTS measurements. We partition the night into two main periods. The first period begins at 1800 LST, after the early evening period of rapid cooling, and extends to 0200 LST when the wind speed at the 20-m top of the tower decreases substantially to an averaged value of about 2 m s^{-1} (Fig. 4, black).

The second period from 0300 to 0600 LST is characterized by relatively low wind speeds even at 20 m (Fig. 4, black). The nocturnal cooling trend becomes large during this period due to the decreased wind speed and turbulence intensity. The flow is characterized by somewhat chaotic small-scale variations of temperature, which are lower amplitude compared to the first half of the night. There is no well-defined scale separation between the turbulent scales and the smallest non-turbulent motions.

We now examine the first half of the night when the nocturnal temperature trend is small, but the variations of temperature on a time scale of roughly 1 h are large, sometimes exceeding 5 K (red, Fig. 4). We concentrate on stations A1 located west of the valley system, A3 in an up-valley tributary gully, A11 on the valley floor, A9 on the slope north of the valley, and the 20-m level of the main tower. See Fig. 8 (Sect. 5) for station locations. The flow is characterized by periods of higher wind speed and generally higher temperatures and periods of lower wind speed and generally lower temperatures (Fig. 5). These time variations of the wind speed and temperature are not closely approximated by a wave pattern because the amplitude varies with time, and sometimes the variations with time are relatively sharp, particularly near the surface. Such small-scale variations of wind and temperature affect the entire network with only small phase differences across the network, and thus are on a horizontal scale that is larger than the 500-m wide observational domain. These variations also extend above the 20-m tower.

The well-defined minimum values of temperature are separated by about 1 h (Fig. 5a). $\theta(A11)$ on the valley floor often becomes much lower than the temperature outside the valley (A1) or on the slope (A9) such that the temperature minimum on the valley floor is part of a transient cold pool (Fig. 5a). The temperature difference between the valley and outside the valley is as large as 7°C during periods of cold pools and can vanish between the periods of cold pools.

5 Case Study of Cooling and the Transient Cold Pool

We choose the period from 1900 to 2100 LST for further study of the development of a transient cold pool with a temperature minimum occurring at about 2000 LST (Fig. 6b). This study period includes the flow evolution leading up to the temperature minimum and subsequent rapid warming. From 19.2 to about 19.8 h, depending on the station, the cooling trend is roughly independent of time (Fig. 6b) and the wind direction is generally north-westerly (Fig. 6c), approximately aligned with the regional slope on a scale of 10–20 km. Just before 20 h, the wind direction generally shifts to south-westerly on the valley floor (for example, stations A8, A10, A11, and A16, Fig. 7) and west-south-westerly on the slope south of the valley (stations A12–A14). The stations on the valley floor experience an enhanced cooling rate during this brief period. This enhanced cooling is abruptly eliminated by a well-defined warm microfront that propagates through the entire network (Sect. 5.3).

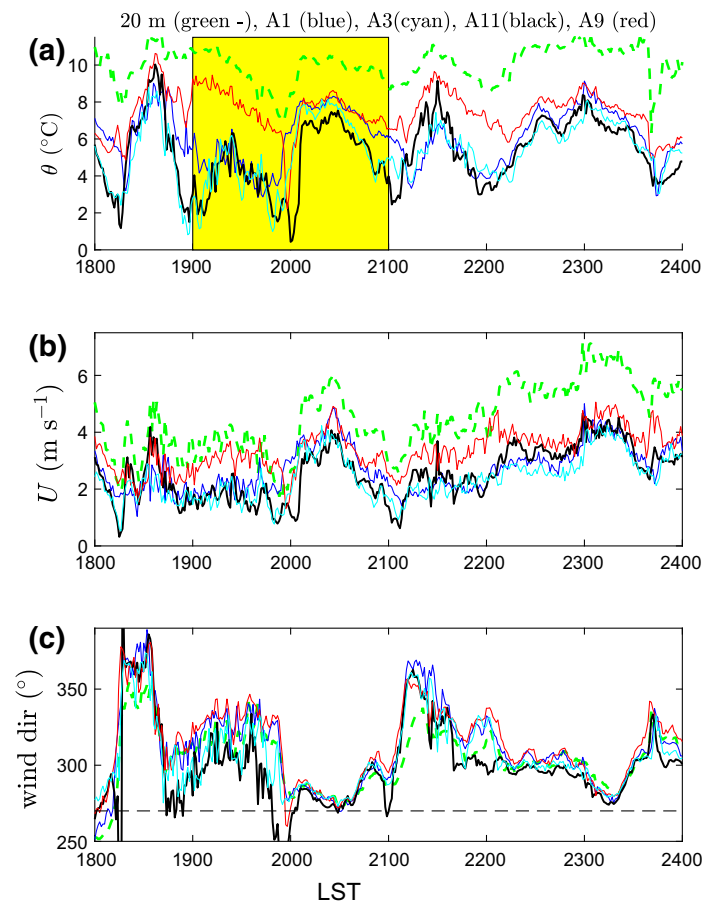


Fig. 5 The period of “higher” wind speed corresponding to the first half of the night. Shown are a) θ , b) U , and c) wind direction for five different stations (see Fig. 7 for station locations). The yellow shading identifies the period of focus for Sect. 5. Note that 360° has been added to north-easterly wind directions to avoid discontinuities. θ is the local potential temperature (Eq. 3)

5.1 The Local South-Westerly Flow

Downslope south-westerly flow develops on the slope south of the valley that ascends toward the south-west for a distance of about 750 m with an average slope magnitude of about 2.5%. At about 19.9 h, this south-westerly flow develops more or less simultaneously along the slope within the network (black, red, Fig. 6c) in association with the reduced north-westerly flow above the valley (green dashed, Fig. 6a, b).

The formation of the brief south-westerly flow occurs intermittently throughout the case study night. In the later half of the case study night when the wind speed is lower, the wind direction on the valley floor (not shown) sometimes oscillates between west-south-westerly and west-north-westerly flow. This oscillation includes station A12 just above the valley floor on the south-west slope. South-westerly flow south of the valley also occurs on other nights. The composite of the nocturnal wind vectors over the entire field program (not shown) indicates that the v -component is negative (northerly) at all of the stations except those on the slope south of the valley where it is approximately zero due to a significant number of cases of south-westerly flow. We conclude that cold-air drainage on the south-westerly slope is of climatic significance at this site. Cold-air drainage down the shorter slope north of the

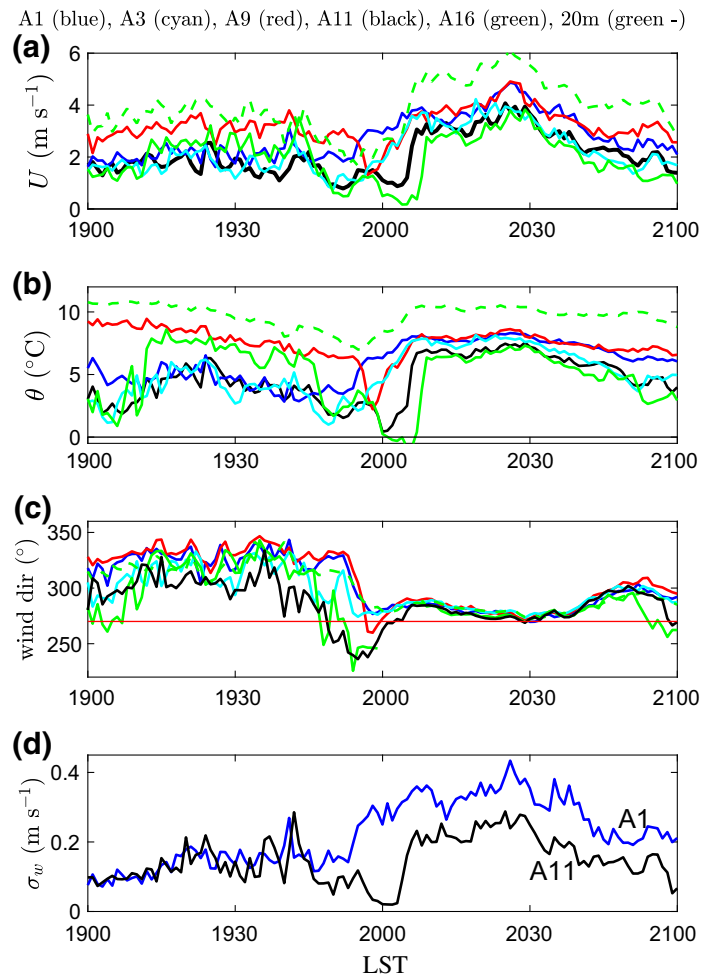


Fig. 6 The 2-h period surrounding the temperature minimum at 2000 LST for a) U , b) θ , c) wind direction, and d) σ_w . Dashed green is the 20-m level on the tower. The progression of the cold air down the shallow valley can be tracked from stations A3 (cyan), A11 (black), and A16 (green). $[\sigma_w]$ is shown for outside the valley at station A1 (blue) and on the valley floor at station A11 (black). See Fig. 7 for station locations

valley is uncommon, where lee turbulence is frequent with a northerly component of the larger-scale flow.

5.2 Transient Cold Pool and Upslope Advection

The temperature minimums on the valley floor can be viewed as a part of the transient cold pools. Brief enhanced local cooling occurs on the valley floor during the period of south-westerly flow (Fig. 6c). A minimum temperature of about 1.5°C occurs around 1951 LST at the up-valley gully station A3 (Fig. 6b, cyan), about 0.4°C at about 2000 LST at the valley station A11 (black), and 1.0°C at about 2006 LST further down the valley at station A16 (green). Apparently the valley imposes sufficient sheltering with the decreasing wind speed (Fig. 6a) to allow formation of a transient cold pool. The transient cold pool is characterized by particularly low turbulence intensity as shown for station A11 on the valley floor (black line, Fig. 6d). In other terms, the minimum wind speed occurs as part of the 1-h variation of the wind field and leads to reduced turbulence and an enhanced cooling rate on the valley

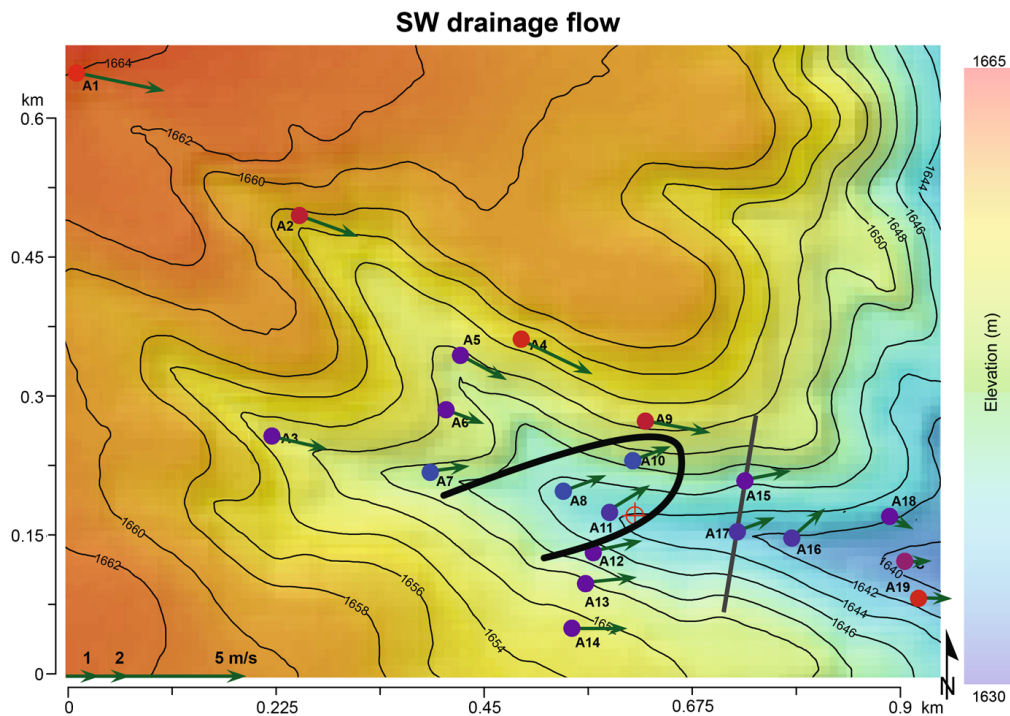


Fig. 7 The spatial distribution of the temperature and wind averaged over the 5-min period ending at 2000 LST. The temperature ranges from 1 °C (blue circles) to 6 °C (red circles). The solid black line roughly outlines the core of the south-west drainage flow. The thin grey line through stations A15 and A17 is the fiber-optic DTS transect. The red + marks the tower location

floor. This particular transient cold pool consists of a double structure at some of the stations divided by a very brief period of warmer air as is also evident in Figs. 9–10.

During the field program, cold events are also observed outside of the valley (not shown). The small-scale temperature variability at station A1 outside the valley is, on average, only about 15% less than that on the valley floor at station A11 (Table 1). However, the physics is different because the short-term temperature variation on the valley floor is typically associated with intermittent cold pools related to topographical sheltering.

An updraft observed in advance of the warm microfront causes adiabatic cooling that might contribute significantly to the total cooling. The vertical velocity on the tower reaches 0.1 m s^{-1} at the 3-m level and 0.2 m s^{-1} at the 20-m level. This updraft arrives too late to account for the initial rapid cooling but contributes to the formation of the coldest air occurring just after 20 h on the valley floor (A11).

The south-westerly flow advects cold air from the valley cold pool up the opposite slope north of the valley, causing cooling that reaches station A9 around 1957 LST (Fig. 6b, red). This corresponds to a displaced cold pool. This cold air then descends back down the slope and down the valley. In fact, the coldest air in the entire network occurs at station A10 on the slope north of the valley, located about 4 m above the elevation of the valley floor (not shown). The advection of the cold air up the slope north of the valley is also evident in the cross-valley fiber-optic DTS cross-section (Figs. 9, 10) where at 2000 LST the cold air (blue) briefly extends up-slope to the top of the fiber-optic DTS transect. For a brief period before 2000 LST, the air is colder on the slope than at the floor of the valley (Fig. 10). This displacement of the coldest air up the slope is common during the SCP field program. The northern edge of the cold air (dark blue) transitions to warm air (red) at a microfront that

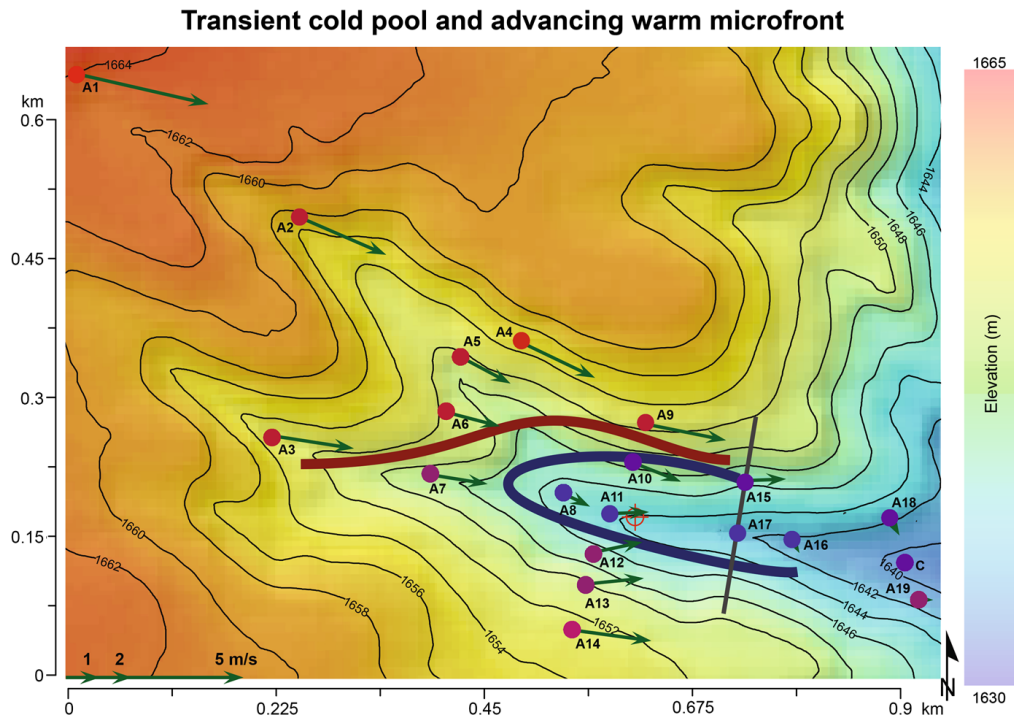


Fig. 8 The spatial distribution of the temperature and wind for the 5-min period beginning at 2000 LST. The temperature ranges from 1 °C (blue circles) to 6 °C (red circles). A plausible sketch of the warm microfront (thick red line), which propagates from the north-north-west in contrast to the surface wind, which is more from the west-north-west. Based on the tower observations, warm air passes over the transient cold pool (thick blue line) and then mixes downward to the valley floor. The thin grey line through stations A15 and A17 is the fiber-optic DTS transect. The red + marks the tower location

does not systematically propagate. This quasi-stationary microfront on the slope north of the valley appears intermittently throughout this night and appears on numerous other nights during the field program.

“Less cold” air on the slope south of the valley is evident in the fiber-optic DTS image that ends in a sharp semi-stationary microfront during the period 1948–2006 LST (light blue to dark blue transition in Figs. 9, 10). This microfront is temporary, does not systematically propagate, and is not particularly common on this slope during the field program.

5.3 Warm Microfront

The warm microfront quickly terminates the cooling trend and eliminates the transient cold pool in the valley, corresponding to a sudden increase of temperature, wind speed, and σ_w (Fig. 6). The enhanced mixing nearly eliminates horizontal variability in agreement with Guerra et al. (2018) and reduces both the stratification and wind directional shear (Fig. 11). The warm microfront begins at station A1 at about 1951 LST (blue, Fig. 6b) and propagates toward the south-east and then occupies the entire western part of the network by 2000 LST (see also Fig. 8). At this time, the warm air reaches A9 and A14 on the slopes north and south of the valley, respectively, but has not yet penetrated to the valley floor. The warm microfront invades the northern end of the fiber-optic DTS transect at about 2000 LST (Fig. 10) and then propagates toward the valley floor during a period of about 5 min. The warm air arrives at the south end of the fiber-optic DTS transect shortly before it reaches the valley floor, again

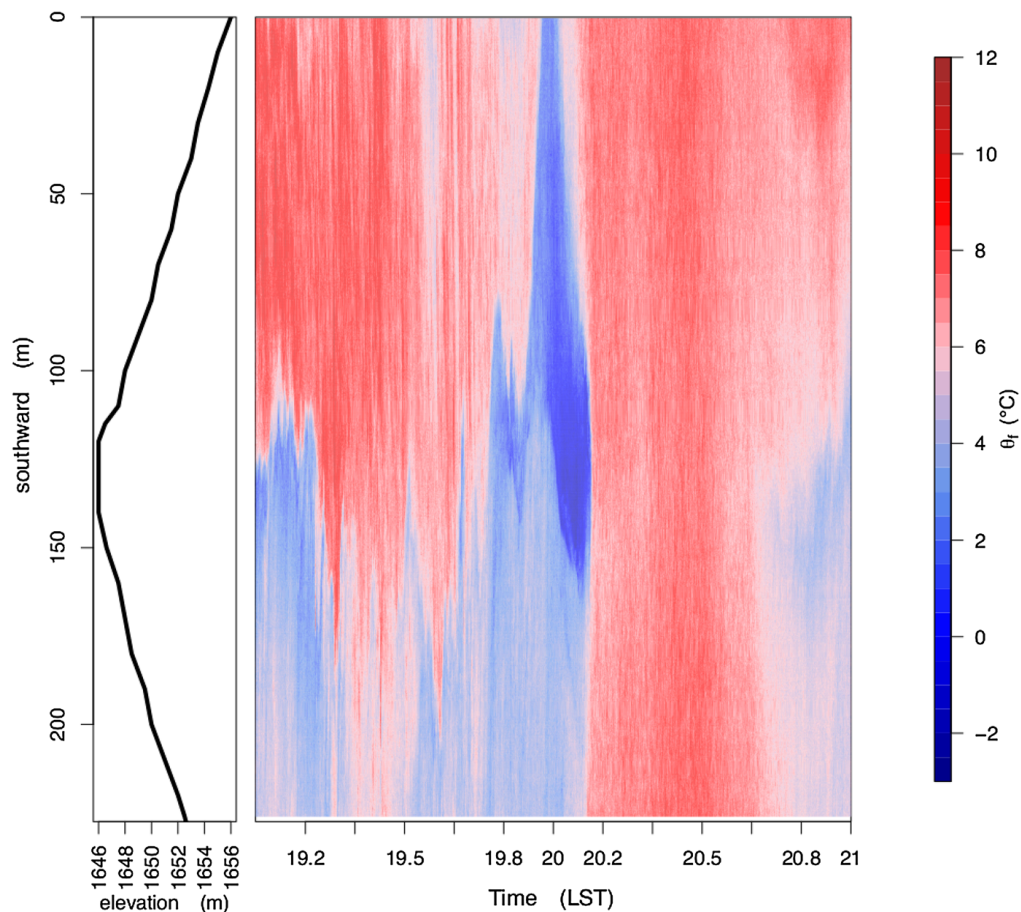


Fig. 9 The time–space variation of the local potential temperature measured by the fiber-optic DTS (θ_f). The coldest air arrives at the DTS cross-section at about 20.0h (2000 LST). It is important to avoid interpreting the x -axis as space instead of time. The topography following the DTS transect is shown on the left. North is toward the top

indicating that for a few minutes the warm air moves over the cold air on the valley floor (Figs. 9, 10). At 2004 LST, the valley cold pool is quickly eliminated, probably by the warm air that is mixed downward by the “relatively” high turbulence intensity in the warm air.

The propagation direction of the warm microfront from the north-west is distinctly different from the wind direction, which is generally more westerly behind the warm microfront. The difference between the wind direction and the apparent direction of the warm microfront propagation could be at least partly related to warming at the surface by the relatively “strong” downward mixing of warmer air behind the warm microfront, in which case the temperature changes are not completely controlled by horizontal advection. Large misalignment between the microfront propagation and the wind direction is common in the observational study of Lang et al. (2018).

5.4 Vertical Structure

The vertical structure of the temperature measured on the 20-m tower (Fig. 11a) indicates that the amplitude of the cooling and the subsequent warming both decrease with height, but are still significant at the top of the tower. The warming within the shallow valley cold

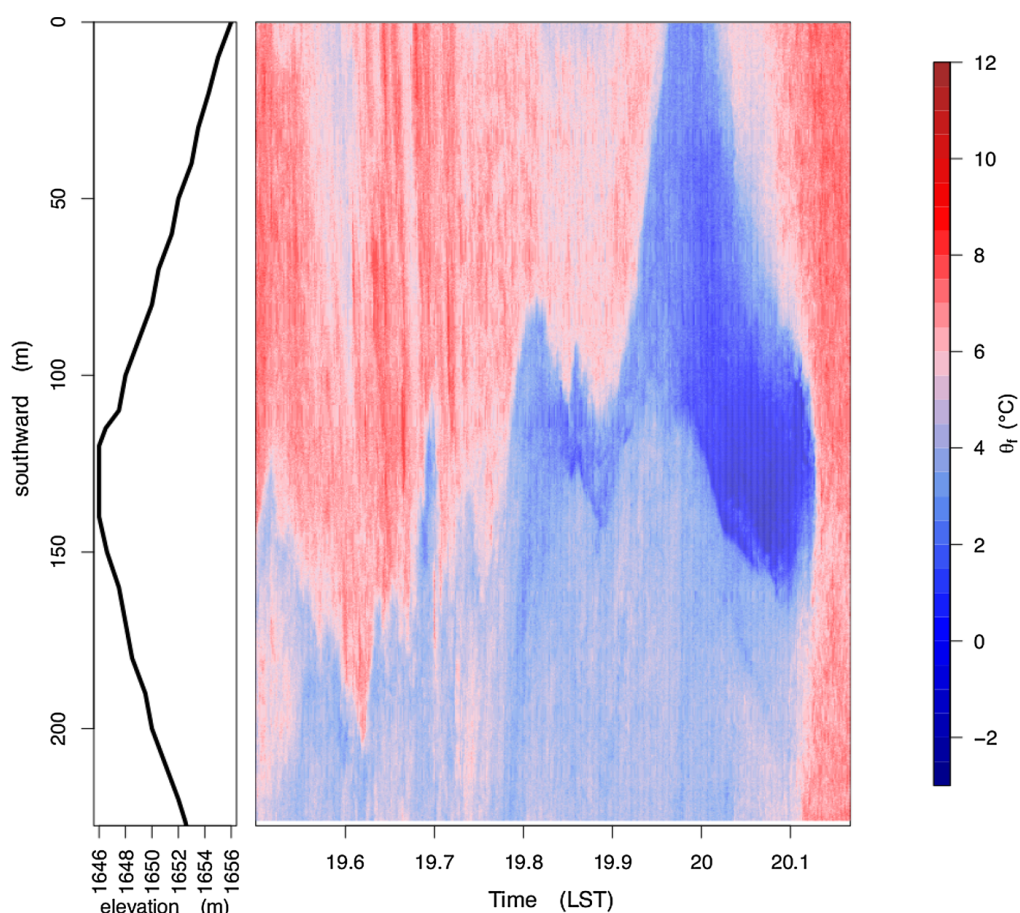


Fig. 10 A zoomed plot of the time-space variation of the local potential temperature measured by the fiber-optic DTS (θ_f) that focuses on the cold event (dark blue)

pool lags that at higher levels and lags the warming outside the valley. The near elimination of the wind directional shear after the warm microfront (Fig. 11b) is presumably due to the significant mixing following the warm microfront.

5.5 Synopsis

The cold event examined here is summarized in Fig. 12 and includes a period of relatively constant cooling rate (19.4–19.8 h, 1924–1948 LST), subject to short-term temperature fluctuations, and includes a period of more rapid cooling and development of drainage flows (19.8–20 h, 1948–2000 LST). A shallow transient cold pool forms on the valley floor followed by advection of cold air up the slope north of the valley floor. This cold event is quickly terminated by a sharp warm microfront (20.1 h, 2006 LST) that leads to significant vertical mixing, significant reduction of the stratification, and near elimination of horizontal variations of temperature within the observational domain.

Transient cold pools and temperature minimums are a common feature during the entire SCP field program and generally form during periods of reduced wind speed on time scales of 10 min to several hours. Wind speeds at 1 m that exceed about 2 m s^{-1} on the valley floor seem to eliminate the transient cold pools and maintain warmer air at the surface, although

Fig. 11 **a** The wind direction, and **b** temperature as a function of height on the tower for measurements at 0.5 m (blue), 1 m (red), 2 m (orange), 3 m (purple), 4 m (grey), 5 m (cyan), 10 m (dark red), and 20 m (blue)

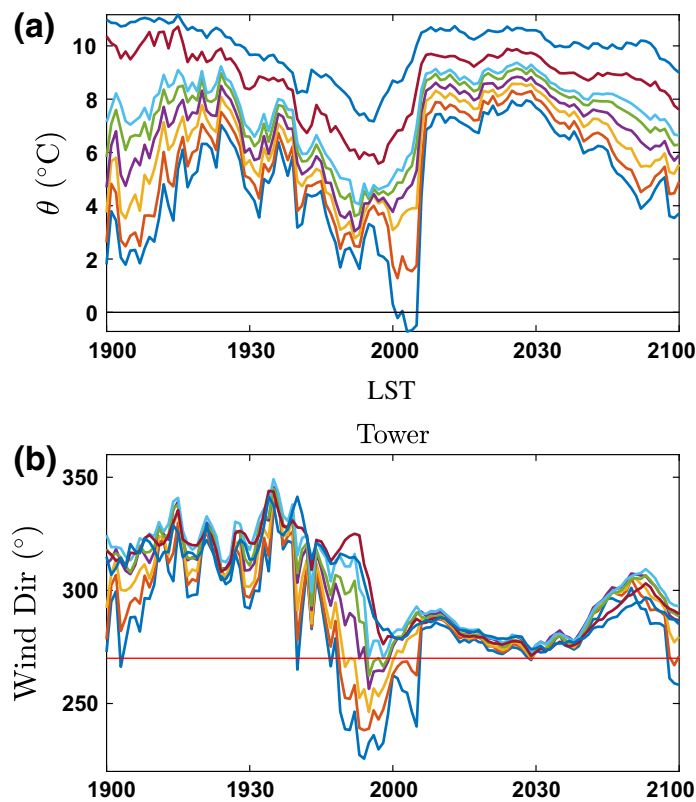
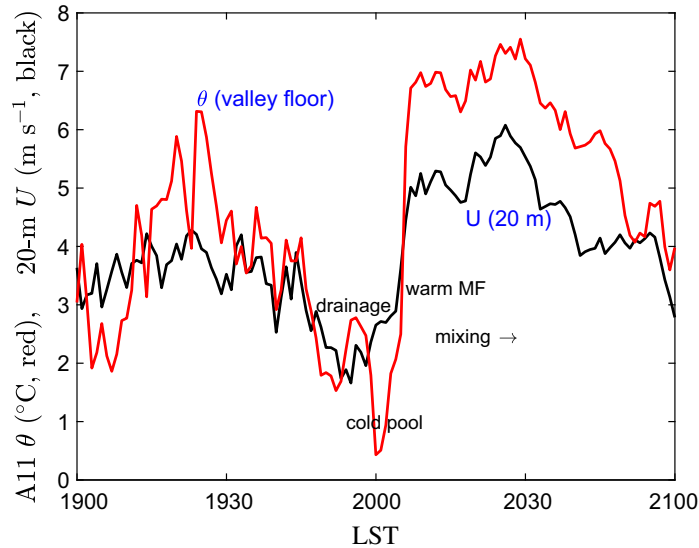


Fig. 12 A summary of the 2-h case study cold event based on the temperature at station A11 on the valley floor (red) and the wind speed at 20 m (black)



this “threshold” appears to vary between stations. This threshold wind speed is higher than the threshold wind speed for the “hockey stick” (Sun et al. 2012), which is about 1.2 m s^{-1} based on the dependence of the 1-m friction velocity on wind speed for the current SCP measurements outside of the valley (Pfister et al. 2019). The higher threshold for the cold pool compared to that for the usual hockey stick is probably due to the influence of sheltering by the topography and associated strong stratification. As a result, the cold-pool threshold also depends on the wind direction.

6 Conclusions

After the early evening period of rapid cooling, small-scale (submeso) temperature variations often become larger than the magnitude of the nocturnal temperature trend (Sect 3). As a consequence of the small-scale temperature variations, the nocturnal temperature actually increases over 1-h periods about 35% of the time at the FLOSSII and SCP sites and 27% of the time at the CASES-99 site. The generality of these results and the complexities of the physics behind these statistics are currently under investigation.

The large variations of temperature on small time scales at the SCP site appear to be due to transient propagating modes that interact with the local modest topography. Spatial and time variation of the temperature, wind, and other quantities associated with the propagating modes can be locally intensified near the surface, sometimes forming cold or warm microfronts. For the first part of the case study night, semi-periodic variations of the wind speed on a time scale of about 1 h range between 1 and 4 m s^{-1} and modulate the turbulence and temperature. Higher-speed periods correspond to greater turbulence intensity and higher temperatures while periods of lower wind speed correspond to lower turbulence intensity and lower temperatures, as expected. During the phases of lower wind speed, local slope circulations and cold pools develop, which are eliminated during the periods of higher wind speeds. Thus, local flows intermittently form and disappear. The second part of the night is characterized by low wind speeds, generally less than 2 m s^{-1} , and includes a large cooling trend with smaller and less organized small-scale variability of temperature.

The small-scale propagating motions and the motions induced by the gentle local topography interact in a way that remains poorly understood. We anticipate that these interactions are globally common. On nights with significant small-scale variations of temperature, even perfect forecasts of the nocturnal trend may fail to identify important short periods of frost or fog formation. The relation of such temperature variations to the wind vector, stratification, downward longwave radiation, and the general magnitude of the small-scale motions must be investigated in more detail, both in terms of cases studies and classification of nights (Pfister et al. 2019).

Acknowledgements We gratefully acknowledge the very helpful comments of the anonymous reviewers. This project received support from Grant AGS-1614345 from the National Science Foundation. The fiber-optic instrument was provided by the Center for Transformative Environmental Monitoring Programs (CTEMPs) funded by the National Science Foundation through award EAR 0930061. The measurements for the SCP and FLOSSII field programs were provided by the Integrated Surface Flux System of the Earth Observing Laboratory of the National Center for Atmospheric Research. The assistance of C. Sayde in the collection and processing the fiber optic DTS data is greatly appreciated.

Open Access This article is distributed under the terms of the Creative Commons Attribution 4.0 International License (<http://creativecommons.org/licenses/by/4.0/>), which permits unrestricted use, distribution, and reproduction in any medium, provided you give appropriate credit to the original author(s) and the source, provide a link to the Creative Commons license, and indicate if changes were made.

References

- Acevedo O, Costa F, Oliveira P, Puhales F, Degrazia G, Roberti D (2014) The influence of submeso processes on stable boundary layer similarity relationships. *J Atmos Sci* 71:207–225
- Ansorge C, Mellado J (2014) Global intermittency and collapsing turbulence in a stratified planetary boundary layer. *Boundary-Layer Meteorol* 153:89–116
- Burman PKD, Prabha TV, Morrison R, Karipot A (2018) A case study of turbulence in the nocturnal boundary layer during the Indian summer monsoon. *Boundary-Layer Meteorol* 169:115–138

- Cava D, Mortarini L, Anfossi D, Giostra U (2019a) Interaction of submeso motions in the Antarctic stable boundary layer. *Boundary-Layer Meteorol* 171:151–173
- Cava D, Mortarini L, Giostra U, Acevedo O, Katul G (2019b) Submeso motions and intermittent turbulence across a nocturnal low-level jet: a self-organized criticality analogy. *Boundary-Layer Meteorol* 172:17–43
- Grudzielanek AM, Cermak J (2018) Temporal patterns and vertical temperature gradients in micro-scale drainage flow observed using thermal imaging. *Atmosphere* 9:498–514
- Guerra VS, Acevedo OC, Medeiros LE, Oliveira PES, Santos DM (2018) Small-scale horizontal variability of mean and turbulent quantities in the nocturnal boundary layer. *Boundary-Layer Meteorol* 169:395–411
- Izett JG, van de Wiel BJH, Baas P, Bosveld FC (2018) Understanding and reducing false alarms in observational fog prediction. *Boundary-Layer Meteorol* 169:347–372
- Kang Y, Belušić D, Smith-Miles K (2015) Classes of structures in the stable atmospheric boundary layer. *Q J R Meteorol Soc* 141:2057–2069
- Lang F, Belušić D, Siems S (2018) Observations of wind direction variability in the nocturnal boundary layer. *Boundary-Layer Meteorol* 166:51–68
- Mahrt L (2017a) Heat flux in the strong-wind nocturnal boundary layer. *Boundary-Layer Meteorol* 163:161–177
- Mahrt L (2017b) The near-surface evening transition. *Q J R Meteorol Soc* 143:2940–2948
- Mahrt L (2017c) Stably stratified flow in a shallow valley. *Boundary-Layer Meteorol* 162:1–20
- Mahrt L, Thomas CK (2016) Surface stress with non-stationary weak winds and stable stratification. *Boundary-Layer Meteorol* 159:3–21
- Momen M, Bou-Zeid E (2017) Mean and turbulence dynamics in unsteady Ekman boundary layers. *J Fluid Mech* 816:209–242
- Monahan A, Rees T, He Y, McFarlane N (2015) Multiple regimes of wind, stratification, and turbulence in the stable boundary layer. *J Atmos Sci* 72:3178–3198
- Monti PF, Chan W, Princevac M, Kowalewski T, Pardyjak E (2002) Observations of flow and turbulence in the nocturnal boundary layer over a slope. *J Atmos Sci* 59:2513–2534
- Mortarini L, Stefanello M, Degrazia G, Roberti D, Castelli ST, Anfossi D (2016) Characterization of wind meandering in low-wind-speed conditions. *Boundary-Layer Meteorol* 161:165–182
- Mortarini L, Cava D, Giostra U, Acevedo O, Nogueira Martins LG, Soares de Oliveira PE, Anfossi D (2017) Observations of submeso motions and intermittent turbulent mixing across a low level jet with a 132-m tower. *Q J R Meteorol Soc* 144:172–183
- Nappo C (1991) Sporadic breakdown of stability in the PBL over simple and complex terrain. *Boundary-Layer Meteorol* 54:69–87
- Ohya Y, Nakamura R, Uchida T (2008) Intermittent bursting of turbulence in a stable boundary layer with low-level jet. *Boundary-Layer Meteorol* 126:249–263
- Petenko I, Argentini S, Casasanta G, Genthon C, Kallistratova M (2019) Stable surface-based turbulent layer during the polar winter at Dome C, Antarctica: Sodar and in situ observations. *Boundary-Layer Meteorol* 171:101–128
- Pfister L, Sigmund A, Olesch J, Thomas CK (2017) Nocturnal near-surface temperature but not flow dynamics, can be predicted by microtopography in a mid-range mountain valley. *Boundary-Layer Meteorol* 165:333–348
- Pfister L, Sayde Selker J, Mahrt L, Thomas CK (2019) Classifying the nocturnal boundary layer into temperature and flow regimes. *Q J R Meteorol Soc* 145:1515–1534
- Poulos G, Blumen W, Fritts D, Lundquist J, Sun J, Burns S, Nappo C, Banta R, Newsome R, Cuxart J, Terradellas E, Balsley B, Jensen M (2001) A comprehensive investigation of the stable nocturnal boundary layer. *Bull Am Meteorol Soc* 83:555–581
- Sun J, Burns S, Lenschow D, Banta R, Newsom R, Coulter R, Frasier S, Ince T, Nappo C, Cuxart J, Blumen W, Lee X, Hu XZ (2002) Intermittent turbulence associated with a density current passage in the stable boundary layer. *Boundary-Layer Meteorol* 105:199–219
- Sun J, Mahrt L, Banta RM, Pichugina YL (2012) Turbulence regimes and turbulence intermittency in the stable boundary layer during CASES-99. *J Atmos Sci* 69:338–351
- Sun J, Mahrt L, Nappo C, Lenschow D (2015a) Wind and temperature oscillations generated by wave-turbulence interactions in the stably stratified boundary layer. *J Atmos Sci* 71:1484–1503
- Sun J, Nappo CJ, Mahrt L, Belušić D, Grisogono B, Stauffer DR, Pulido M, Staquet C, Jiang Q, Pouquet A, Yagüe C, Galperin B, Smith RB, Finnigan JJ, Mayor SD, Svensson G, Grachev AA, Neff WD (2015b) Review of wave-turbulence interactions in the stable atmospheric boundary layer. *Rev Geophys*. <https://doi.org/10.1002/2015RG000487>
- Tampieri F, Yagüe C, Viana S (2015) The vertical structure of second-order turbulence moments in the stable boundary layer from SABLES98 observations. *Boundary-Layer Meteorol* 157:45–59

- Thomas CK, Kennedy A, Selker J, Moretti A, Schroth M, Smoot A, Tufillaro N (2012) High-resolution fibre-optic temperature sensing: a new tool to study the two-dimensional structure of atmospheric surface-layer flow. *Boundary-Layer Meteorol* 142:177–192
- Van de Wiel BJH, Ronda R, Moene A, de Bruin H (2002) Intermittent turbulence and oscillations in the stable boundary layer over land. Part I: a bulk model. *J Atmos Sci* 59:942–958
- Vercauteren N, Mahrt L, Klein R (2016) Investigation of interactions between scales of motion in the stable boundary layer. *Q J R Meteorol Soc* 142:2424–2433
- Vercauteren N, Boyko V, Kaiser A, Belušić D (2019) Statistical investigations of flow structures in different regimes of the stable boundary layer. *Boundary-Layer Meteorol*. <https://doi.org/10.1007/s10546-019-00464-1>
- Zeeman MJ, Selker JS, Thomas C (2015) Near-surface motion in the nocturnal, stable boundary layer observed with fibre-optic distributed temperature sensing. *Boundary-Layer Meteorol* 154:189–205

Publisher's Note Springer Nature remains neutral with regard to jurisdictional claims in published maps and institutional affiliations.

C Thermal Submeso-scale Motions in the Nocturnal Stable Boundary Layer - Part 1: Detection & Mean Statistics

Noname manuscript No.
(will be inserted by the editor)

1 Thermal Submeso-scale Motions in the Nocturnal 2 Stable Boundary Layer - Part 1: Detection & Mean 3 Statistics

4 **Lena Pfister · Karl Lapo · Larry**
5 **Mahrt · Christoph K. Thomas**

6
7 Received: DD Month YEAR / Accepted: DD Month YEAR

8 **Abstract** In the stable boundary layer submeso-scale motions were detected
9 during the Shallow Cold Pool experiment conducted in the Colorado plains,
10 CO, USA in 2012. The submeso-scale motion consisted of two air layers cre-
11 ating a very well defined front with a sharp temperature gradient, hereafter
12 referred to as thermal submeso-fronts (TSF). The semi-stationary TSFs and
13 their advective velocities were detected and determined by the fibre-optic dis-
14 tributed sensing (FODS) technique. An objective detection algorithm using
15 FODS was created to detect the TSF boundary which enabled a detailed in-
16 vestigation of its spatio-temporal statistics. The therefore needed key step in
17 data processing was to conditionally average any parameter depending on ei-
18 ther the occurrence of TSFs or the distance between the TSF boundary and

This project received support from awards AGS-1115011, AGS-1614345, and AGS-0955444 by the National Science Foundation and contracts W911NF-10-1-0361 and W911NF-09-1-0271 by the Army Research Office. We acknowledge the Earth Observing Laboratory of the National Center for Atmospheric Research for collecting the sonic anemometer measurements for the Shallow Cold Pool experiment. This project has received funding from the European Research Council (ERC) under the European Union's Horizon 2020 research and innovation programme under grant agreement No 724629, project DarkMix.

L. Pfister
University of Bayreuth - Micrometeorology, Bayreuth, Germany
E-mail: lena.pfister@uni-bayreuth.de

K. Lapo
University of Bayreuth - Micrometeorology and Bayreuth Center of Ecology and Environ-
mental Research (BayCEER), Bayreuth, Germany
E-mail: karl.lapo@uni-bayreuth.de

L. Mahrt
NorthWest Research Associates, Corvallis, Oregon, USA
E-mail: mahrt@nwra.com

C. K. Thomas
University of Bayreuth - Micrometeorology and Bayreuth Center of Ecology and Environ-
mental Research (BayCEER), Bayreuth, Germany
E-mail: christoph.thomas@uni-bayreuth.de

the measurement location. With this technique any measurement was set into the spatial context of TSFs and thus phenomena specifically at the boundary could be investigated. At the TSF boundary the air layers converge creating an updraft, strong static stability, and vigorous mixing. Further, the advective velocity of TSFs is an order of magnitude lower than the mean wind speed. The topography even though it was gentle plays an important role in forming TSFs. Details on generating mechanisms and implications of TSFs on the stable boundary layer are discussed in the second part.

Keywords Fibre optics · Stable boundary layer · Topography · Submeso motion

1 Introduction

Atmospheric processes cover a broad range of temporal and spatial scales as introduced by Orlanski (1975) to which the submeso scale was added later. They range from the macro-scale (cyclones), meso-scale (orographic effects, urban heat island, thunderstorms) to the micro-scale (convection, turbulence). This paper focuses on atmospheric processes on the submeso scale with a spatial scale of several hundred metres and temporal scales up to one hour – higher temporal and spatial scales than turbulence, but lower spatial scales than deep convection.

Understanding the formation of submeso-scale motions within the stable boundary layer (SBL) as well as their connection to turbulent fluxes is important as it affects near-surface transport processes and thus ecosystems and humans. Submeso-scale motions like cold-air drainage within the SBL may alleviate urban heat islands (Kuttler et al. 1996; Sachsen et al. 2014), and affect the formation of fog (Izett et al. 2019). The formation of cold-air layers can trap contaminants and other gases that cause health hazards (Silcox et al. 2012). Further, turbulent fluxes which are influenced by submeso-scale motions impact hydrological cycles by determining the timing of snow melt (Pohl et al. 2006; Mott et al. 2011; Burns et al. 2012), and sublimation of snow (MacKay et al. 2006; Reba et al. 2012).

Investigating submeso-scale motions was the objective of the Shallow Cold Pool (SCP) experiment in the Colorado plains, CO, USA in 2012. The SCP experiment used a very dense network of stations distributed across the valley in addition to acoustic remote sensing. Publications so far focused on investigating stably stratified flow (Mahrt et al. 2014b; Mahrt 2017c), the structure of the nocturnal boundary layer (Geiss and Mahrt 2015; Mahrt and Heald 2015; Mahrt 2017b), and the response of the boundary layer to shear (Mahrt et al. 2014a; Mahrt 2017a). Further, the relation between horizontal wind speed, turbulence characteristics, and stratification was investigated in detail (Mahrt and Thomas 2016). In some of these publications transitory modes or microfronts are mentioned which cause intermittently increased turbulence during cold-air drainage and pooling which raises further questions about their formation and interaction with the stable boundary layer. While Mahrt (2017b) investigated

this to some extent, these question were not answered satisfactorily.

The detailed investigation of nocturnal submeso-scale motions necessitates a measurement technique which offers high spatial resolution of temperature measurements such as the fibre-optic distributed sensing (FODS) technique. Every few centimetre along a fibre-optic cable spatially-distributed air temperature and wind speed can be measured up to a frequency of 1 Hz. FODS was applied in the atmospheric boundary layer (Keller et al. 2011; Thomas et al. 2012; Sayde et al. 2015; Sigmund et al. 2017) leading to unique results like the tomography of a cold-air current (Zeeman et al. 2015), the invalidation of Taylor’s hypothesis in the atmospheric surface layer (Cheng et al. 2017), and the determination of temperature and flow regimes (Pfister et al. 2017, 2019). FODS is a very useful technique especially for tracking transitory submeso-scale motions in time, however, it does not provide flux measurements like ultrasonic anemometer stations yet.

During SCP measurements with the FODS technique were conducted along a 240 m long cross-valley transect. FODS provided spatially continuous measurements of temperature and for the first time also wind speeds (Sayde et al. 2015) using the actively heated fibre-optic cable approach. Even though the sonic anemometer and thermohygrometer network during SCP is considered dense, it was unable to track nocturnal submeso-scale motions (Mahrt 2017b). In contrast, observations from FODS contained in the supplementary material of this study did show thermal submeso-scale motions. Here, the interaction between a warm-air and cold-air layer forming a thermal front was observed moving up and down the northern valley side wall. Here, we name these motions thermal submeso-fronts (TSF) similar to the study of Mahrt (2010).

In part 1 of our study we develop the detection algorithm for the TSF boundary and compute unique spatiotemporal statistics. The novelty of our study is being able to detect the presence and the precise location of the TSF boundary used for conditional averaging by setting point observations from ultrasonic anemometry into the spatial context of the near-surface temperature field from FODS. This approach utilized the strength of both measurement techniques. Mean statistics are given revealing the horizontal extent as well as vertical structure of the boundary layer during the occurrence of TSFs, their advective velocity, and characteristics of the two air layers forming TSFs.

2 Field Site and Methods

2.1 Shallow Cold Pool Experiment

The Shallow Cold Pool Experiment was designed to investigate shallow cold pools in gentle terrain. It was conducted in northeast Colorado, USA, over semiarid grassland at approximately 1660 m above mean sea level from 01 October to 01 December 2012 (https://www.eol.ucar.edu/field_projects/scp). Ancillary measurements with the FODS makes it a unique field study. FODS measurements were conducted between 16 November and 27 November.

This study analyzed the nine nights with FODS data without observational gaps from 1900 LT (local time = UTC – 7 h) until 0500 LT. A detailed description of the field site and all instrumentation can be found in Mahrt and Thomas (2016).

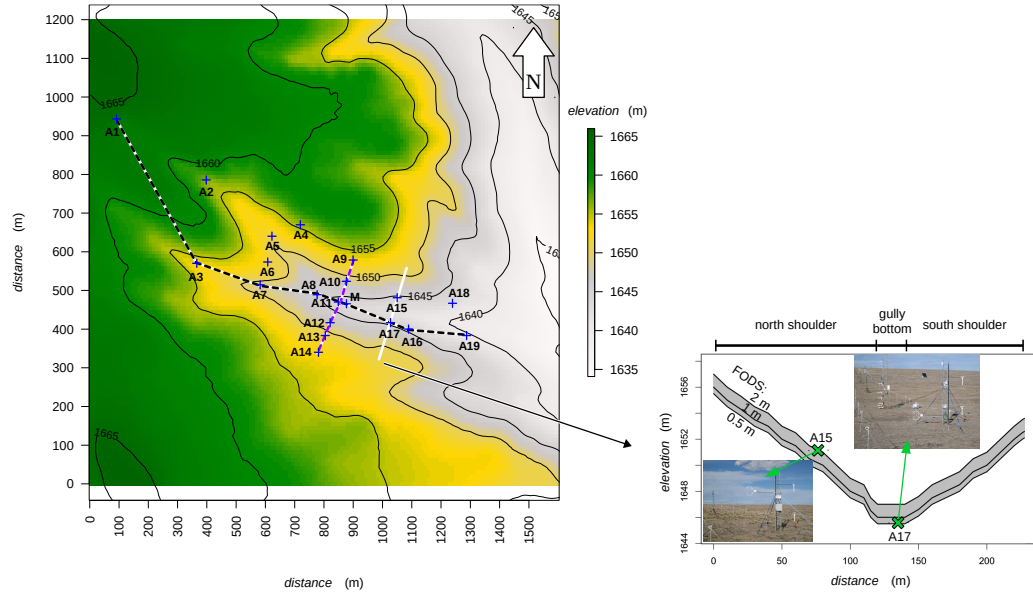


Fig. 1 Left: Topographical overview of field site with ultrasonic anemometer stations (A1–A19), the 20 m high main tower (M), and the fibre-optic distributed sensing (FODS) transect (white line). Chosen stations for down-valley transect (dashed black line) and cross-valley transect (dashed purple line) for Figure 4 (cf. Sect. 3.2). Right: Cross-valley view of the fiber-optic transect showing its length and elevation

The valley can be described as gentle terrain with a height difference of ≈ 27 m from north-west to south-east along a distance of ≈ 1.2 km resulting in a maximum inclination of 1.4° (https://www.eol.ucar.edu/system/files/files/field_project/SCP/SCP-RIC.kmz). On average, the valley slopes rise about 12 m over a horizontal distance of about 130 m. The width of the flat valley bottom averages about 5 m. The north side of the valley is characterized by a small plateau followed by a smooth hill into the valley with an inclination of $\approx 6.0^\circ$ (Fig. 1). Inclination and heights were determined with a hand-held GPS instruments.

A near-surface network of 19 ultrasonic anemometer (Model CSAT3, Campbell Scientific, Logan, UT, USA) stations (A1–A19) at 1 m above ground level (a.g.l.), except A15 at 2 m and A17 at 0.5 m a.g.l., and a 20-m tower with eight ultrasonic anemometer stations (0.5 m, 1–5 m, 10 m, 20 m a.g.l.) were set up. Data from the 3-m station had to be discarded due to errors. At the tower ventilated thermohygrometers operated by the National Center for Atmospheric Research (NCAR) (https://www.eol.ucar.edu/rtf/facilities/isff/sensors/ncar_trh.pdf) were installed at several heights of which the 0.5-m and 15-m measurements on the main tower (M) were used

to estimate static stability in this study.

The fiber-optic transect sampled by the FODS instrument (Ultima SR, Silixa, London, UK) was 240 m long and was constructed from a cable duplet: an unheated optical glass fibre cable with an outer diameter (OD) of 0.9 mm to measure air temperatures, and an actively heated stainless steel fibre-optic cable (1.3 mm OD) for measurements of the wind speed component orthogonal to the fibre-optic cable. Each fibre-optic cable duplet was installed at 0.5 m, 1 m and 2 m a.g.l. (cf. Fig. 1). The temporal and spatial resolution of the FODS measurements were 5 s and 0.25 m, respectively. Artifacts from the fibre holders causing additional heating or cooling of the fiber-optic cable were removed and filled using spatial linear interpolation for each time step. For further information on the FODS setup and the wind speed measurements refer to Sayde et al. (2015) and Pfister et al. (2019).

Ancillary to the 20-m tower a ground-based acoustic wind profiler (SODAR, PCS2000-24, Metek GmbH, Elmshorn, Germany) was installed at the valley bottom (1640 m mean sea level) between station A18 and A19. The wind profiler had an observational range of 10 m to 320 m a.g.l. measuring the horizontal wind speed as well wind direction every 10 m. Measurements were averaged to 5 min. For analysis we are using the cluster data output of the sodar which is quality-controlled by the internal data processing software.

2.2 Averaging Operators and Computed Fluxes

We applied Reynolds decomposition to determine temporal and spatial perturbations, in which an arbitrary variable ϕ is divided into a mean and a fluctuating part:

$$\phi = \bar{\phi} + \phi', \quad (1)$$

$$\phi = \langle \phi \rangle + \hat{\phi}, \quad (2)$$

with $\bar{\phi}$ representing the temporal and $\langle \phi \rangle$ the spatial mean, while ϕ' and $\hat{\phi}$, respectively, are the corresponding fluctuating parts. In our study an averaging time scale of 60 s was chosen. For this time scale the Fast Fourier Transform power- and cospectra of temperature and wind speed agreed well between an ultrasonic anemometer station and the nearest FODS measurement. A variety of spatial scales was used for computing $\langle \phi \rangle$ depending on the involved stations and which transect or area was investigated.

To determine turbulence characteristics the friction velocity, u_* , and sensible heat flux, Q_H , were computed from the measurements of each ultrasonic anemometer station as:

$$u_* = \left(\overline{u'_s w'_s}^2 + \overline{v'_s w'_s}^2 \right)^{0.25}, \quad (3)$$

$$Q_H = \rho c_p \overline{w'_s T'_s}, \quad (4)$$

with u_s , v_s and w_s being the west-, south- and vertical-component of the wind, T_s the temperature, ρ the air density and c_p is the specific heat at

constant pressure. The meteorologic sign convention is used with negative sign representing a net flux towards the surface, while positive sign indicates a flux away from the surface.

For conditional averaging a parameter ϕ was averaged over all samples fulfilling a specific condition and is marked by angular brackets $[\phi]$. Mean values and the standard deviation of wind direction was computed by the method of Yamartino (1984). The bulk Richardson number was computed from the FODS transect as

$$Ri_B = \frac{g}{\bar{\theta}} \frac{\Delta\theta\Delta z^{-1}}{(\Delta u\Delta z^{-1})^2}, \quad (5)$$

with $\bar{\theta}$ being the mean layer temperature and $\Delta\theta\Delta z^{-1}$ and $\Delta u\Delta z^{-1}$ being the vertical potential temperature and wind speed gradients at each measurement point within the FODS transect. $[Ri_B]$ was calculated by the conditionally averaged quantities of $[\bar{\theta}]$, $[\Delta\theta\Delta z^{-1}]$, and $[\Delta u\Delta z^{-1}]$.

2.3 Comparison of Fibre-Optic and Ultrasonic Anemometers Measurements

FODS and ultrasonic anemometers measurements were compared to assure high data quality and to test if both devices can be used interchangeably for conditional averaging. Scatter-plot of temperature revealed a high linear 1:1-correlation ($R^2 = 0.996$) between FODS and ultrasonic anemometer measurements at an offset of -0.4 K for A15 (2 m a.g.l.) at the Northern shoulder and -0.2 K for A17 (0.5 m a.g.l.) at the valley bottom (Fig. 9a & b). This offset of both ultrasonic anemometers was accounted for in the complete field campaign to match the FODS measurements, which reduced the disagreement between FODS and ultrasonic anemometer to 5–6%. Analysis of the spatial and temporal temperature perturbations demonstrated a close match between the devices (Fig. 9c & d). We therefore conclude that both devices represent the mean and turbulent temperature field equally well enabling their use for conditional averaging.

Evaluating the FODS wind speed measurements showed a dependence on the angle of attack to the fibre (Sayde et al. 2015; Pfister et al. 2019; van Ramshorst et al. 2019). As expected, wind speeds parallel to the fibre orientation are generally underestimated by FODS. FODS wind speed measurements were not adjusted for this angular dependence as there were not enough sonic anemometer next to the FODS transect to correct for it. Nonetheless, FODS can be used to determine the vertical wind speed gradient assuming wind directions within 2 m a.g.l. are constant with height given the topography.

2.4 Detection of Thermal Submeso-Fronts and Conditional Averaging

A detection algorithm was developed for the TSF boundary using the sharp horizontal temperature difference, $\Delta_x\theta$, between the warm air on the north

199 shoulder and adjacent cold air (cf Fig. 2b). The spatially continuous FODS
 200 data were used to determine the exact location of the non-stationary TSF
 boundary in a three-step process:.

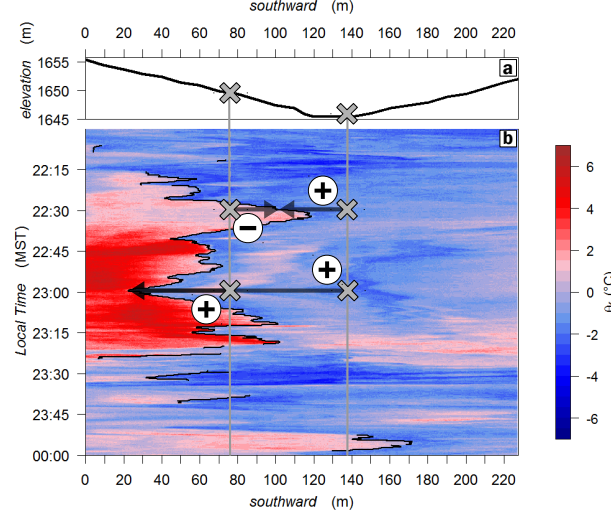


Fig. 2 (a) Length of fiber-optic transect and elevation in metres showing the cross-valley topography. (b) Potential fibre-optic temperatures θ_f (colour bar) within the valley in a space–time–diagram. Two examples are given how the distance to the thermal submeso-front was assigned for both ultrasonic anemometer stations (grey crosses and vertical lines) with the help of black arrows and \pm signs reflecting the sign for the distance

201 First, the optimal separation distance needed to be determined for comput-
 202 ing the spatial temperature difference $\Delta_x \theta$ between two measurement bins
 203 of FODS. We used a fixed separation distance between bins and then com-
 204 puted $\Delta_x \theta$ for all bin-pairs of the fibre-optic transect for each transect level.
 205 The physical location of $\Delta_x \theta$ was the center between the bins. For each time
 206 step, the location of the maximum $\Delta_x \theta$ should reveal the location of the TSF
 207 boundary. Different separation distances ranging from 0.5 m up to 16 m were
 208 tested and their results evaluated visually. A separation distance of 4 m was
 209 optimal as it provided large $\Delta_x \theta$ values while being considered precise enough
 210 to represent a TSF boundary.

212 Second, if temperatures are spatially homogeneous, $\Delta_x \theta$ should diminish to
 213 very small values and drop below a certain threshold. The threshold was de-
 214 fined as the uncertainty of temperature differences, δ_T , measured by FODS.
 215 This quantity is defined as $\delta_T = \sqrt{2\sigma_{FODS}^2}$ with σ_{FODS} being the root mean
 216 error of the temperature difference between a reference platinum-wire ther-
 217 mometer and the FODS cable in a thermally controlled calibration bath. We
 218 discarded any $\Delta_x \theta < 0.73$ K.

219 In a last step two further measures were applied: TSFs were required to persist
 220 for at least 40 s, and TSFs were discarded if their advective velocity within 5 s
 221 was higher than the maximum wind speed detected at 2 m a.g.l. for the ana-
 222 lyzed nights. We assumed that TSFs do not move faster than this maximum

223 wind speed at any time. The outcome of this detection algorithm is shown in
224 Figure 2b as solid black line.

225 The uniqueness of this study is the use of conditional averaging to set any
226 measurement location into the spatial context of the TSF boundary. There-
227 fore, a relative distance between the TSF boundary and the measurement
228 location of an arbitrary parameter, ϕ , was defined with the sign indicating the
229 air layer in which ϕ was measured. A negative sign indicated the warm-air
230 layer, while a positive sign indicated the cold-air layer (cf. Fig 2b). A rela-
231 tive distance could only be determined for the FODS measurements and two
232 ultrasonic anemometer stations, namely A15 and A17 of the sensor network
233 (Fig. 1 & Fig. 2a), as they were adjacent to the FODS transect. For all other
234 measurements including the SODAR measurements conditional averaging was
235 applied only depending on the occurrence of TSFs.

236 3 Results and Discussion

237 3.1 Mean Statistics and Conditions during the Occurrence of Thermal 238 Submeso-Fronts

239 The main characteristic of TSFs is the sharp horizontal temperature gradient,
240 $\max(\Delta_x \theta)$, between the warm and cold air with a mean value of 3.0 K ranging
241 up to 13.0 K (cf. Fig. 2b). It is formed by the interface created by warm air
242 entering the valley from the north and cold air being present primarily at the
243 valley bottom, but occasionally reaching up to the valley's sidewall. TSFs were
244 a consistent feature on the north shoulder of the valley moving up- and down.
245 Therefore, the TSFs in our study are semi-stationary. TSFs occurred 31% of
246 the time and during most nights of statically stable conditions with a duration
247 between 40 s up to 1 hour. Their spatial scales ranged from 200 m to 300 m
248 as determined from the complete ultrasonic anemometer network (Sect. 3.2).
249 Hence, we classify TSFs as submeso-scale motions following (Orlanski 1975)
250 which occur frequently in the SBL. The advective velocity of TSFs, defined
251 as the spatial change in TSF boundary location over time, was 0.2 ms^{-1} on
252 average with maximums reaching up to 5.5 ms^{-1} . TSFs are moving very slowly,
253 roughly an order of magnitude lower than the mean wind speed. This is in
254 concordance with Lang et al. (2018) which concluded that flow perturbations
255 of microfronts are not transported by the local flow.

256 The TSF boundary was detected at all three levels of the FODS transect
257 simultaneously, allowing for the derivation of the tilt of the TSF boundary
258 defined as the angle between the TSFs boundary and the surface (cf. Fig. 8).
259 The inter-quartile range of this tilt angle was $21^\circ - 37^\circ$ with the warm air
260 being aloft of the cold air and tilting towards the valley bottom. If the tilt is
261 close to the inclination of the valley shoulders, we would expect a full developed
262 cold-air pool with warmer air sliding on top. As the tilt is much higher than
263 6° , the tilt of the TSF boundary is created by the convergence of the warm-air
264 and cold-air layer.

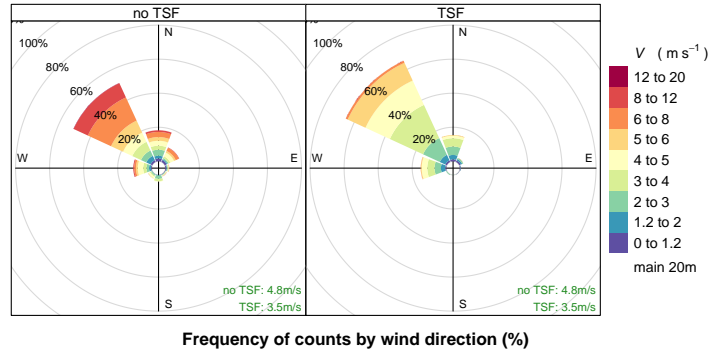


Fig. 3 Wind roses showing the frequency of wind speed and direction for the 20-m station on the main tower during the occurrence and absence of thermal submeso-fronts (cf. titles)

During SCP the main wind direction was from north-west and did not change during the occurrence of TSFs as shown by the 20-m measurement on the main tower (Fig. 3). TSFs preferably occurred in weaker winds (3.5 ms^{-1}) compared to slightly stronger winds at 20 m a.g.l. in their absence (4.8 ms^{-1}).

3.2 Spatial Extent of Thermal Submeso-Fronts at Field-Site Scale

Conditional averaging based on the occurrence of TSFs was applied to $\hat{\theta}$ and u_* for each ultrasonic anemometer network station shown as spatially interpolated contour plots. Figure 4 represents the average location of the TSF boundary as the conditional average computed over all incident TSFs without considering their actual location. Three views were chosen (cf. Fig. 1) for a quasi 3D—presentation of TSFs: overhead view, down-valley view (dashed black line), and cross-valley view (dashed purple line). In addition to near-surface stations the down-valley view incorporates all stations of the main tower, while the cross-valley view only includes the 20-m station.

For the computation of u_* height-independent fluxes are assumed being in equilibrium with the surface. Since one knows from FODS that cold- and warm-air layers were in contact with the surface, the use of u_* appears justified for all 1-m stations, while on the main tower it is only justified for the stations within the cold-air layer.

Two air layers can clearly be distinguished in Figure 4a. For the warm-air layer near-surface temperatures (Fig. 4a) as well as $[u_*]$ (Fig. 4d) were increased across the entire plateau edge on the North shoulder. While at the same time on the valley bottom $[\hat{\theta}]$ and $[u_*]$ were low for all near-surface stations as they were located within the cold-air layer. The air layers also had different flow directions as illustrated by arrows in Figure 4a & d. Stations within the warm-air layer had a strong flow from north-west which is aligned with the flow at 20 m on the main tower (Fig. 3), while stations within the cold-air layer had a weaker terrain-following flow corresponding to that of the

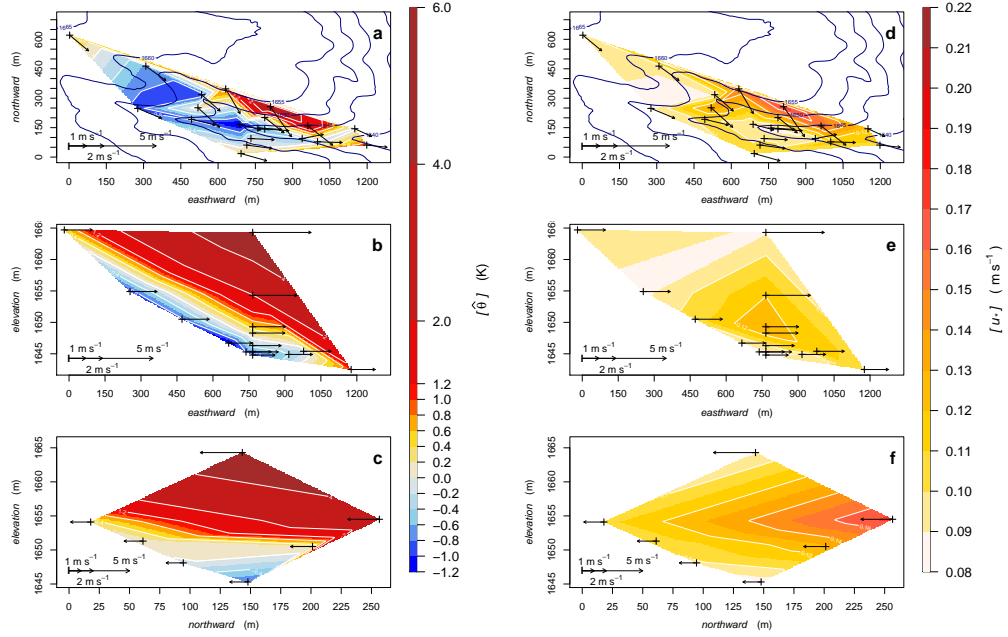


Fig. 4 Spatial temperature perturbations $[\hat{\theta}]$ (a–c) and friction velocity $[u_*]$ (d–f) during the occurrence of thermal submeso-fronts as overhead view of the field site (a & d), as down-valley view (b & e), and as a cross-valley view (c & f). Stations included for each view are shown in Figure 1. Black crosses: ultrasonic anemometer station. Blue contourlines: elevation in metre above mean sea level; Arrows: mean horizontal wind speed (legend bottomleft); Arrows of the overhead view (a & d) also show the flow direction

293 1-m station on the main tower (Fig. 10).

294 Here we discuss the role of topography to form both air layers. The flow enters
 295 the valley from north-west flowing over the small plateau. Due to the elevation
 296 change on the northern shoulder the flow detaches from the ground, creates a
 297 cavity region, and then reconnects with the surface where increased turbulence
 298 and mixing are observed, which are topographically induced. This interpreta-
 299 tion is supported by observations at the stations at the opposite side of the
 300 valley at identical elevation, which did not show similarly strong $[\hat{\theta}]$ (Fig. 4c)
 301 and $[u_*]$ (Fig. 4e) compared to those on the North shoulder. For the valley
 302 bottom, the topography provides shelter for cold-air drainage and pooling as
 303 indicated by the terrain-following flow of low temperatures. This interpreta-
 304 tion is supported by TSFs occurring and cold-air drainage persisting during
 305 topographically induced mixing and relatively high wind speeds. Hence, to-
 306 pography played a major role in forming TSFs even though this process is
 307 usually not anticipated for gentle terrain and stronger winds.

308 From the preceding section we recall that the mean horizontal extent of the
 309 warm-air and cold-air layer of TSFs was approximately 200–300m and thus
 310 TSF classify as submeso-scale motions. To determine their vertical extent, the
 311 profile of u_* was analyzed (Fig. 4e) as $\hat{\theta}$ only showed a stable boundary layer
 312 profile without revealing specific air layers further aloft (Fig. 4b). Friction ve-
 313 locity u_* was smallest in the lowest 2 m a.g.l., while at 4 m and 5 m a.g.l.

peak values were observed. We conclude that the cold-air layer characterized by low turbulence had a mean thickness ranging between 2 m and 3 m topped by warm air. The cross-valley view confirms this configuration (Fig. 4c & f). The vertical structure of TSFs and their impact for the SBL is discussed in detail in Part 2 of this study (Pfister et al. 2020).

When TSF were absent (not shown) u_* and $\hat{\theta}$ were spatially very homogeneous and wind direction was uniform across all stations as shown by the 1-m and 20-m station on the main tower (Fig. 10 & Fig. 3). We therefore conclude TSFs are eroded by the intense turbulent mixing in a coupled boundary layer with uniform flow direction even when topographic undulations are present.

3.3 Thermal Submeso-Front Characteristics from Spatially Distributed Sensing

A more detailed view of the TSF boundary was derived from conditionally averaging the FODS data using the relative distance to the TSF boundary. The mean temperature drop from warm to cold air was 3.4 K over a horizontal distance of approximately 20 m (Fig. 5a). When defining the transition

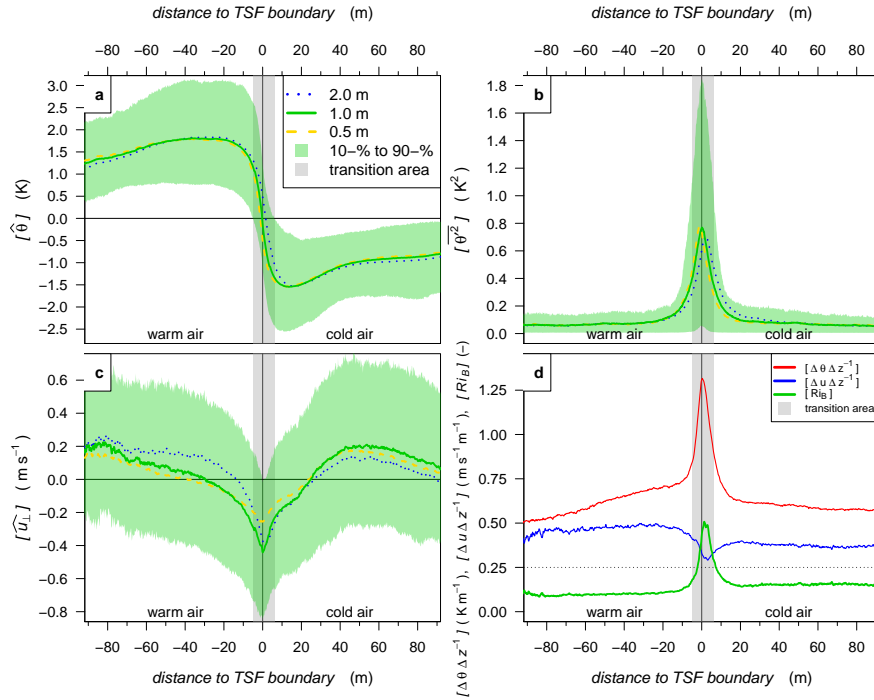


Fig. 5 Conditional averaging of fiber-optic data depending on the distance to the thermal submeso front: (a) spatial temperature perturbation $[\hat{\theta}]$, (b) temporal temperature perturbation $[\hat{\theta}^2]$, (c) spatial wind speed perturbation $[\hat{u}]$, and (d) bulk Richardson number $[Ri_B]$

area from warm to cold air at the TSF boundary as the location of the sign change between the 10-% and 90-% percentiles of $[\hat{\theta}]$, its width results to 11 m (cf. Fig. 5). The transition area may appear very narrow, but substantially impacts temporal temperature perturbations (Fig. 5b), the wind field (Fig. 5c), as well as static stability and wind speed shear (Fig. 5d). Peak values in the transition area were 0.8 K^2 for $[\overline{\theta'^2}]$, winds speeds dropped by 0.5 ms^{-1} , static stability was maximum at 1.3 Km^{-1} , and $[\Delta u \Delta z^{-1}]$ dropped by $0.2 \text{ ms}^{-1} \text{ m}^{-1}$ (Fig. 5d). In the transition area, warm air pushes against and slides over the cold air creating strong static stability as well as the peak in $[\overline{\theta'^2}]$. Considering the size of the transition area and the advective velocity of TSFs determined earlier, the observing the transition from cold to the warm air took on average 55 s at a fixed location. This finding confirmed our earlier choice of an averaging time scale of 60 s. The drop in wind speed shear is caused by the convergence of the air layers creating similar velocities in the lowest 2 m a.g.l.. Therefore, peak values in Ri_B were detected at the transition area due to the peak in $[\Delta \theta \Delta z^{-1}]$ and drop in $[\Delta u \Delta z^{-1}]$. When the warm air slides over the cold-air layer, it can create a ripple-like structure of the interfacial boundary. This modulation was not further investigated but can be seen e.g. in Figure 2b and thus were added to the conceptual summary given in Figure 8.

3.4 Flow and Turbulence Characteristics of Thermal Submeso-Fronts from Single-point Measurements

The contrasting flow characteristics of the two competing air-layers of the TSF are investigated in detail by conditional averaging the observations from the two ultrasonic anemometer stations A15 and A17 next to the FODS measurements. Here, we present statistics on the horizontal wind speed, V , the wind along the FODS transect, v_s , vertical wind, w_s , wind direction, φ , friction velocity, u_* , and sensible heat flux, Q_H .

Wind speeds in the warm-air layer were higher by almost 2.0 ms^{-1} compared to those in the cold air (Fig. 6a). v_s changed sign within the transition area with strong negative values within the warm-air layer and small positive values within the cold-air layer (Fig. 6b), which highlights the opposite flow direction of the air layers and their convergence at the interfacial boundary. The warm air was entering the valley from north-north-west while the cold air was following the terrain with winds from west-south-west (Fig. 6d) creating a mean wind directional shear of 90° between the air layers.

In the transition area, an upward motion was observed with w_s changing sign from negative to positive (Fig. 6c). This change in sign was already detected a few meters in advance of the station on the north shoulder while at the valley bottom w_s was also positive, but rather weak. The dense cold air acts as a barrier for the warm air, hence, instead of eroding the cold-air layer it slides on top and is forced upwards. This effect is weaker at the valley bottom because the warm-air layer only reaches the valley bottom during stronger winds and

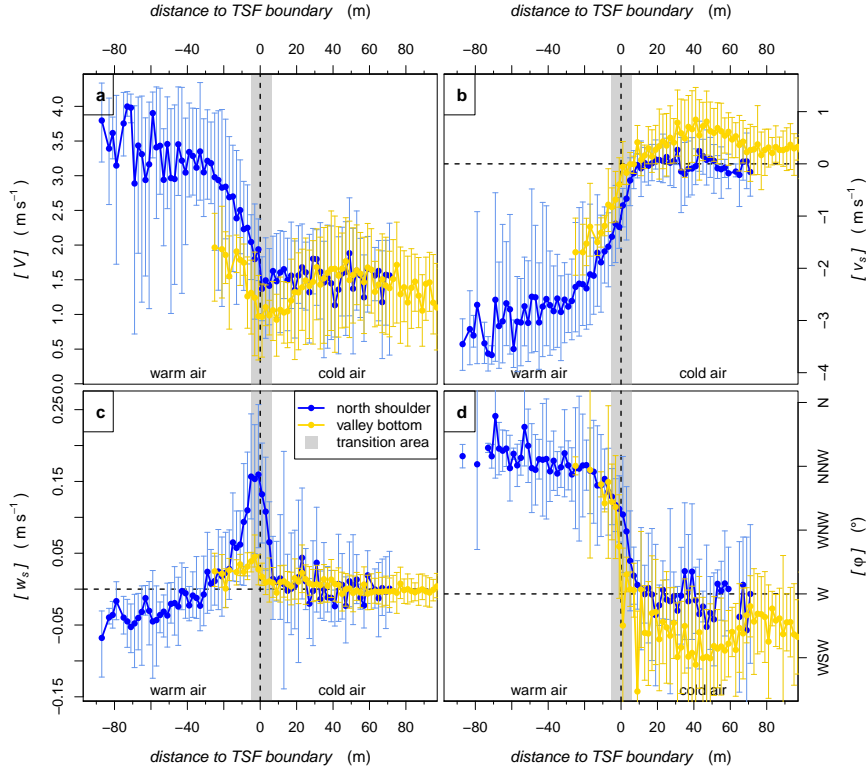


Fig. 6 Conditional averaging of ultrasonic anemometer data depending on the distance to the thermal submeso-front boundary: (a) horizontal wind speed $[V]$, (b) North–south–component of the wind $[v_s]$, (c) vertical wind speed $[w_s]$, and (d) mean wind direction $[\varphi]$. Bars: 10%- and 90%-percentile; Colours: location of ultrasonic anemometer station; Grey area: transition area

corresponding strong turbulence which most likely erodes the cold air, hence, the upward motion of the warm air is weaker or negligible.

Note that $[\hat{u}]$ computed from FODS (Fig. 5d) does not show the same results as $[V]$ from the ultrasonic anemometer stations. This difference is likely caused by the flow direction deviating from being perpendicular to the optical fibre orientation in the warm-air compared to that in the cold-air layer (cf. Fig. 6d). This systematic directional leads to an underestimation of the wind speed from actively-heated FODS (Pfister et al. 2019). We were unable to compensate for this observational artifact due to the lack of a sufficient number of reference stations next to the FODS transect which would have allowed for applying an angularly dependent correction.

Turbulence characteristics strongly differed for the contrasting air layers of the TSF. In the warm air, u_* as well as Q_H were elevated (Fig. 7) as can be expected from high wind speeds and topographically induced turbulent mixing. In contrast, u_* and Q_H were very low in the cold air as can be expected for cold-air drainage and pooling with reduced vertical turbulent exchange. In summary, TSFs caused a rapid change in u_* and Q_H of 0.1 ms^{-1} and -30 Wm^{-2} , respectively during passage.

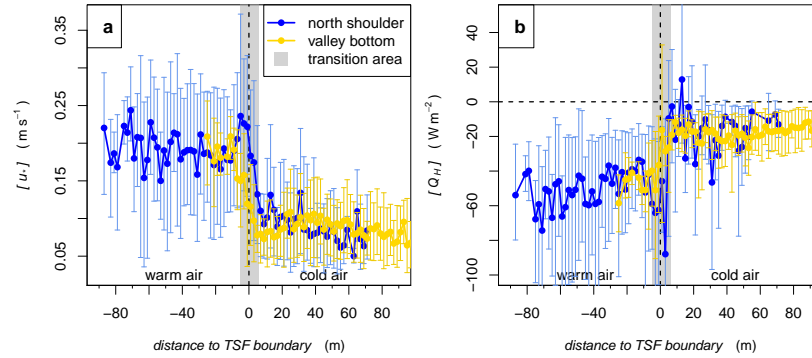


Fig. 7 Conditional averaging of ultrasonic anemometer data depending on the distance to the thermal submeso-front: (a) friction velocity $[u_*]$, and (b) sensible heat flux $[Q_H]$. Bars and colours like in Figure 6

4 Conclusion

The SCP experiment is a unique study combining the observational strengths of the FODS technique with a near-surface network of ultrasonic anemometer stations to investigate thermal submeso fronts (TSF) within the nocturnal boundary layer in gentle terrain.

TSFs occurred frequently in the stable boundary layer and were generated by the gentle topography creating two air layers with distinctly different characteristics: The warm-air layer is mechanically generated by topographically induced turbulence consistently elevating near-surface temperatures at the plateau-edge, while the cold-air layer is thermodynamically driven by topographically induced cold-air drainage and pooling with low near-surface temperatures in the valley bottom caused by radiative cooling. A key feature of this study was the conditional averaging revealing the vertical and horizontal structure of TSFs as well as processes at the TSF boundary.

The main findings of our study are best summarized in a conceptual cross-section of a TSF (Fig. 8)

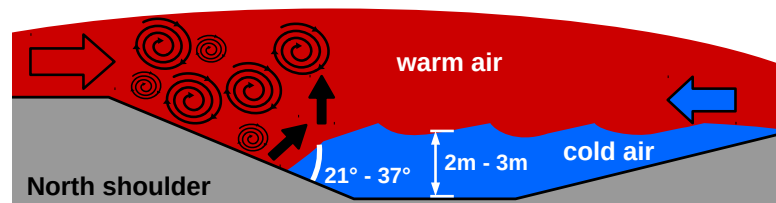


Fig. 8 Conceptual drawing of a thermal submeso-front (not to scale) within the valley (grey areas) consisting of a warm-air layer (red) and a cold-air layer (blue). Coloured arrows indicate the different flow direction of the air layers, while black swirls indicate the topographically induced mixing. At the transition area, where the air layers merge, the warm-air layer is pushed upwards (black arrow) as the cold-air layer is like a barrier

Implications of TSFs for the stable boundary layer are discussed in part 2.

References

- Burns SP, Horst TW, Jacobsen L, Blanken PD, Monson RK (2012) Using sonic anemometer temperature to measure sensible heat flux in strong winds. *Atmos Meas Tech* 5(9):2095–2111, DOI 10.5194/amt-5-2095-2012
- Cheng Y, Sayde C, Li Q, Basara J, Selker J, Tanner E, Gentine P (2017) Failure of Taylor’s hypothesis in the atmospheric surface layer and its correction for eddy-covariance measurements. *Geophys Res Lett* 44(9):4287–4295, DOI 10.1002/2017GL073499
- Geiss A, Mahrt L (2015) Decomposition of Spatial Structure of Nocturnal Flow over Gentle Terrain. *Boundary-Layer Meteorol* 156(3):337–347, DOI 10.1007/s10546-015-0043-7
- Izett JG, Schilperoort B, Coenders-Gerrits M, Baas P, Bosveld FC, van de Wiel BJH (2019) Missed Fog? *Boundary-Layer Meteorol* DOI 10.1007/s10546-019-00462-3
- Keller CA, Huwald H, Vollmer MK, Wenger A, Hill M, Parlange MB, Reimann S (2011) Fiber optic distributed temperature sensing for the determination of the nocturnal atmospheric boundary layer height. *Atmos Meas Tech* 4(2):143–149, DOI 10.5194/amt-4-143-2011
- Kuttler W, Barlag AB, Roßmann F (1996) Study of the thermal structure of a town in a narrow valley. *Atmos Environ* 30(3):365–378
- Lang F, Belušić D, Siems S (2018) Observations of Wind-Direction Variability in the Nocturnal Boundary Layer. *Boundary-Layer Meteorol* 166(1):51–68, DOI 10.1007/s10546-017-0296-4
- MacKay MD, Bartlett PA, Chan E, Derksen C, Guo S, Leighton H (2006) On the simulation of regional scale sublimation over boreal and agricultural landscapes in a climate model. *Atmos - Ocean* 44(3):289–304, DOI 10.3137/ao.440306
- Mahrt L (2010) Common microfronts and other solitary events in the nocturnal boundary layer. *Q J R Meteorol Soc* 136(652):1712–1722, DOI 10.1002/qj.694
- Mahrt L (2017a) Directional Shear in the Nocturnal Atmospheric Surface Layer. *Boundary-Layer Meteorol* 165(1):1–7, DOI 10.1007/s10546-017-0270-1
- Mahrt L (2017b) Lee Mixing and Nocturnal Structure over Gentle Topography. *J Atmos Sci* 74(6):1989–1999, DOI 10.1175/JAS-D-16-0338.1
- Mahrt L (2017c) Stably Stratified Flow in a Shallow Valley. *Boundary-Layer Meteorol* 162(1):1–20, DOI 10.1007/s10546-016-0191-4
- Mahrt L, Heald R (2015) Common Marginal Cold Pools. *J Appl Meteorol Climatol* 54(2):339–351, DOI 10.1175/JAMC-D-14-0204.1
- Mahrt L, Thomas CK (2016) Surface Stress with Non-stationary Weak Winds and Stable Stratification. *Boundary-Layer Meteorol* 159(1):3–21, DOI 10.1007/s10546-015-0111-z
- Mahrt L, Richardson S, Stauffer D, Seaman N (2014a) Nocturnal wind-directional shear in complex terrain. *Q J R Meteorol Soc* 140(685):2393–2400, DOI 10.1002/qj.2369

- Mahrt L, Sun J, Oncley SP, Horst TW (2014b) Transient Cold Air Drainage down a Shallow Valley. *J Atmos Sci* 71(7):2534–2544, DOI 10.1175/JAS-D-14-0010.1
- Mott R, Egli L, Grünewald T, Dawes N, Manes C, Bavay M, Lehning M (2011) Micrometeorological processes driving snow ablation in an Alpine catchment. *Cryosph* 5(4):1083–1098, DOI 10.5194/tc-5-1083-2011
- Orlanski I (1975) A rational subdivision of scales for atmospheric processes. *Bull Am Meteorol Soc* 56(5):527–530
- Pfister L, Sigmund A, Olesch J, Thomas CK (2017) Nocturnal Near-Surface Temperature, but not Flow Dynamics, can be Predicted by Microtopography in a Mid-Range Mountain Valley. *Boundary-Layer Meteorol* 165(2):333–348, DOI 10.1007/s10546-017-0281-y
- Pfister L, Lapo K, Sayde C, Selker J, Mahrt L, Thomas CK (2019) Classifying the nocturnal atmospheric boundary layer into temperature and flow regimes. *Q J R Meteorol Soc* 145(721):1515–1534, DOI 10.1002/qj.3508
- Pfister L, Lapo K, Mahrt L, Thomas CK (2020) Thermal submeso-scale motions in the nocturnal stable boundary layer - Part 2: Generating mechanisms & implications. *Boundary-Layer Meteorol*
- Pohl S, Marsh P, Pietroniro A (2006) Spatialtemporal variability in solar radiation during spring snowmelt. *Hydrol Res* 37(1):1–19, DOI 10.2166/nh.2006.0001
- van Ramshorst JGV, Coenders-Gerrits M, Schilperoort B, van de Wiel BJH, Izett JG, Selker JS, Higgins CW, Savenije HHG, van de Giesen NC (2019) Wind speed measurements using distributed fiber optics: a windtunnel study. *Atmos Meas Tech Discuss* (March):1–21, DOI 10.5194/amt-2019-63
- Reba ML, Pomeroy J, Marks D, Link TE (2012) Estimating surface sublimation losses from snowpacks in a mountain catchment using eddy covariance and turbulent transfer calculations. *Hydrol Process* 26(24):3699–3711, DOI 10.1002/hyp.8372
- Sachsen T, Ketzler G, Schneider C (2014) Past and future evolution of nighttime urban cooling by suburban cold air drainage in Aachen. *J Geogr Soc Berlin* 144(3):274–289, DOI 10.12854/erde-144-19
- Sayde C, Thomas CK, Wagner J, Selker J (2015) High-resolution wind speed measurements using actively heated fiber optics. *Geophys Res Lett* 42(22):10,064–10,073, DOI 10.1002/2015GL066729
- Sigmund A, Pfister L, Sayde C, Thomas CK (2017) Quantitative analysis of the radiation error for aerial coiled-fiber-optic distributed temperature sensing deployments using reinforcing fabric as support structure. *Atmos Meas Tech* 10(6):2149–2162, DOI 10.5194/amt-10-2149-2017
- Silcox GD, Kelly KE, Crosman ET, Whiteman CD, Allen BL (2012) Wintertime PM_{2.5} concentrations during persistent, multi-day cold-air pools in a mountain valley. *Atmos Environ* 46:17–24, DOI 10.1016/j.atmosenv.2011.10.041
- Thomas CK, Kennedy AM, Selker JS, Moretti A, Schroth MH, Smoot AR, Tufillaro NB, Zeeman MJ (2012) High-Resolution Fibre-Optic Temperature Sensing: A New Tool to Study the Two-Dimensional Structure of At-

- 499 atmospheric Surface-Layer Flow. Boundary-Layer Meteorol 142(2):177–192,
 500 DOI 10.1007/s10546-011-9672-7
- 501 Yamartino RJ (1984) A Comparison of Several Single-Pass Estimators of the
 502 Standard Deviation of Wind Direction. J Clim Appl Meteorol 23(9):1362–
 503 1366, DOI 10.1175/1520-0450(1984)023<1362:ACOSPE>2.0.CO;2
- 504 Zeeman MJ, Selker JS, Thomas CK (2015) Near-Surface Motion in the Noc-
 505 turnal, Stable Boundary Layer Observed with Fibre-Optic Distributed Tem-
 506 perature Sensing. Boundary-Layer Meteorol 154(2):189–205, DOI 10.1007/
 507 s10546-014-9972-9

508 Appendix

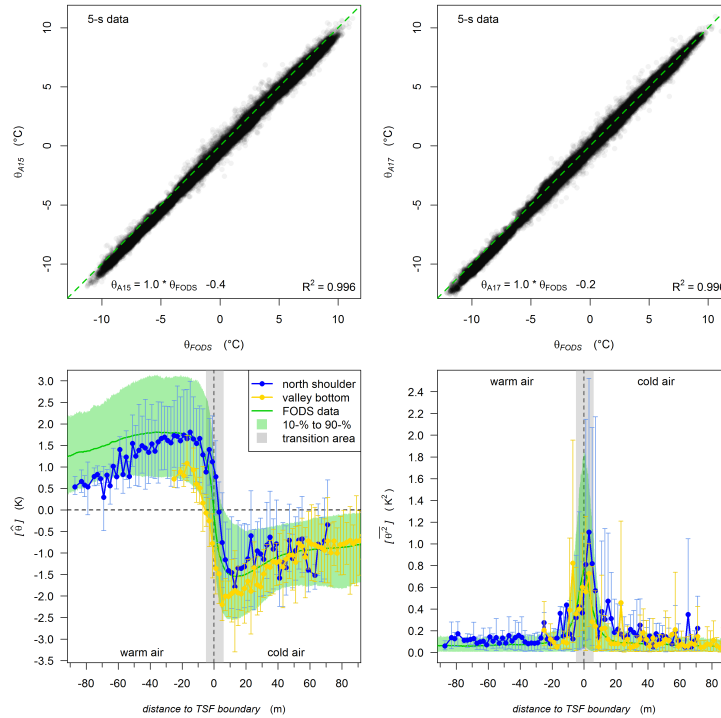


Fig. 9 Comparison of fiber-optic and ultrasonic anemometer temperature measurements (a) at 2 m a.g.l. on the North shoulder and (b) at 0.5 m a.g.l. at the valley bottom revealing the offset between measurements. The offset was adjusted for the ultrasonic anemometer measurements. After the correction the spatial (c) and temporal temperature perturbation (d) show the match between all measurement devices

D Thermal Submeso-scale Motions in the Nocturnal Stable Boundary Layer - Part 2: Generating Mechanisms & Implications

Noname manuscript No. (will be inserted by the editor)
--

1 **Thermal submeso motions in the nocturnal stable**
2 **boundary layer - Part 2: Generating mechanisms &**
3 **implications**

4 **Lena Pfister · Karl Lapo · Larry**
5 **Mahrt · Christoph K. Thomas**

6
7 Received: DD Month YEAR / Accepted: DD Month YEAR

8 **Abstract** Within the stable boundary layer thermal submeso fronts (TSF)
9 were detected during the Shallow Cold Pool experiment, conducted in the Col-
10 orado plains, CO, USA in 2012. The topography induced TSFs by forming two
11 different air layers being stacked vertically above the valley bottom but also
12 converging on the valley side wall. The warm-air layer is mechanically gener-
13 ated by lee turbulence consistently elevating near-surface temperatures, while
14 the cold-air layer is thermo-dynamically driven by cold-air drainage decreas-
15 ing near-surface temperatures. The semi-stationary TSFs can only be tracked
16 and investigated in detail when using fiber-optic distributed sensing as point
17 observations miss TSFs most of the time.
18 TSFs were not determined by a specific wind speed and even the air layers of

This project received support from awards AGS-1115011, AGS-1614345, and AGS-0955444 by the National Science Foundation and contracts W911NF-10-1-0361 and W911NF-09-1-0271 by the Army Research Office. We acknowledge the Earth Observing Laboratory of the National Center for Atmospheric Research for collecting the sonic anemometer measurements for the Shallow Cold Pool experiment. This project has received funding from the European Research Council (ERC) under the European Union's Horizon 2020 research and innovation programme under grant agreement No 724629, project DarkMix.

L. Pfister
University of Bayreuth - Micrometeorology, Bayreuth, Germany
E-mail: lena.pfister@uni-bayreuth.de

K. Lapo
University of Bayreuth - Micrometeorology and Bayreuth Center of Ecology and Environ-
mental Research, Bayreuth, Germany
E-mail: karl.lapo@uni-bayreuth.de

L. Mahrt
NorthWest Research Associates, Corvallis, Oregon, USA
E-mail: mahrt@nwra.com

C. K. Thomas
University of Bayreuth - Micrometeorology and Bayreuth Center of Ecology and Environ-
mental Research, Bayreuth, Germany
E-mail: christoph.thomas@uni-bayreuth.de

TSFs were not confined to one specific wind or thermal regime. Nevertheless, each air layer had a specific relation between the horizontal wind and the friction velocity. Accordingly, a single threshold separating different flow regimes within the boundary layer is an oversimplification especially during TSFs. No local forcings or thresholds could determine the occurrence of TSFs except that they were less likely to occur during stronger near-surface or synoptic winds. Classical conceptualizations and techniques of the boundary layer fail to describe TSFs, however, when using spatial continuous data new insights can be given. As a result, future studies need to incorporate spatially continuous data horizontally as well as vertically in addition to a sensor network to be able to fully characterize and describe boundary layers.

Keywords Fiber optics · Stable boundary layer · Topography

1 Introduction

Submeso scale motions (submeso motions) are described by their typical temporal (and spatial) scale within the classification of Orlanski (1975). By this definition a range of motions fall into this category like meandering, solitary waves, gravity waves, wave-like motion, or microfronts. Detection of submeso motions was usually done on tower data by analyzing case studies with corresponding meandering (Cava et al. 2019a), using the Haar-wavelet (Mahrt 2019), by analyzing spectra and thus their temporal scale (Stiperski and Calaf 2018), identifying meandering by autocorrelation functions (Anfossi et al. 2005) or by using autocorrelation functions to determine oscillations within several parameter like horizontal and vertical wind speed, temperature and scalars (Kang et al. 2014, 2015; Mortarini et al. 2018; Stefanello et al. 2020).

Submeso motions usually occur during a weak large-scale flow and as described by for example Mortarini et al. (2019) are a distinctive feature of the stable boundary layer (SBL). The turbulence structure and vertical exchange of SBLs are altered during the occurrence of submeso motion, hence, investigating those motions is very important. Stiperski and Calaf (2018) found out that most likely due to submeso motions the isotropy of turbulence is significantly altered and thus require different scaling methods within the SBL. Further, in a follow-up study Vercauteren et al. (2019) related this anisotropy to the activity of submeso motions. Meandering within the SBL has an impact on horizontal and vertical exchange processes (Cava et al. 2019a), impact scalar dispersion, flux patterns, and the surface energy balance (Stefanello et al. 2020). Usually the short-term variability of the temperature during submeso motions significantly exceeds the nocturnal trend (Mahrt et al. 2020). Submeso motions can also be related to low level jets (LLJ) and corresponding turbulent down-bursts (Mortarini et al. 2018; Cava et al. 2019b).

As described in part 1 of this manuscript (Pfister et al. 2020), we were able to detect and track the propagation of a specific submeso motion which we called thermal submeso front (TSF). The presented study focuses on vertical

exchange processes during TSFs as especially within the SBL vertical exchange processes are important for determining when z-less scaling cannot be applied. Most studies use tower or vertical data to investigate submeso motions, hence, by the focus on the vertical we tried to set the occurrence of TSFs into the context of most studies. Further, the implications of TSFs on SBLs are investigated as well as their relation to commonly used approaches to classify the boundary layer like wind regimes defined by the relation of horizontal wind speed to a turbulence statistic (Sun et al. 2012) or thermal regimes defined by the relation of the Obukhov length to the sensible heat flux (Mahrt 1998). With the fiber-optic distributed temperature sensing (FODS) technique we were able to detect and track the propagation of TSF (cf. Sect. 2). TSFs consist of two contrasting air layers as shown in a conceptual drawing in Figure 1. A small summary of part 1 of this manuscript is given in Section 3. As FODS was a essential tool for detecting and tracking TSFs, we compare the spatial continuous FODS with point observations (Sect. 4.1). At the vertical tower, the layered structure of TSFs is further investigated with regard to vertical exchange processes (Sect. 4.2). For clarifying the forcings of TSFs, which created the two different air layers, parameters like topography, the near-surface and synoptic wind field, static stability, and radiative forcing were investigated (Sect. 4.3). The manuscript is rounded up with a discussion on the implications of TSFs for SBLs (Sect. 4.4), recommendations for further studies (Sect. 4.5), and the conclusion (Sect. 5).

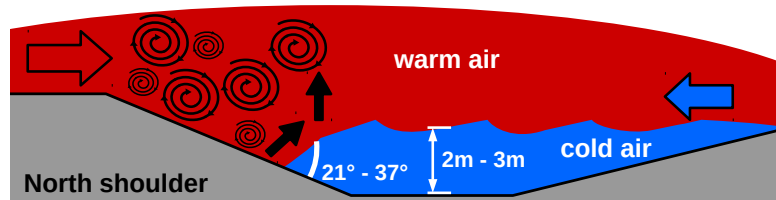


Fig. 1 Conceptual drawing of a thermal submeso front within the valley (not to scale).

2 Field Site & Methods

The data of the Shallow Cold Pool Experiment (SCP) was used for this analysis. A full introduction is given in Pfister et al. (2020). SCP was conducted in northeast Colorado, USA, over semiarid grassland at approximately 1660 m above mean sea level from 01 October to 01 December 2012 (https://www.eol.ucar.edu/field_projects/scp). Measurements with FODS makes it a unique study in addition to a network of 19 ultrasonic anemometer, a 20-m tower with 8 ultrasonic anemometer, and a wind profiler. FODS measurements were only conducted from 16 November until 27 November. This study analyzed the nine nights with FODS data without observational gaps from 1900 LT (local time = UTC - 7 h) until 0500 LT. An topographical overview

with the instrumentation is shown in Figure 12.

We applied Reynolds decomposition to determine temporal and spatial perturbations with an averaging time scale of 60 s (Pfister et al. 2020). To determine turbulence characteristics the friction velocity, $u_* = \left(\overline{u'_s w'_s}^2 + \overline{v'_s w'_s}^2 \right)^{0.25}$, and sensible heat flux, $Q_H = \rho c_p \overline{w'_s T'}$, were computed from the measurements of the ultrasonic anemometer stations with u_s , v_s and w_s being the west-, south- and vertical-component of the wind, T the temperature as measured by each ultrasonic anemometer station, ρ the air density and c_p is the specific heat at constant pressure. The meteorologic sign convention is used with negative sign representing a flux towards the surface, while positive sign indicates a flux away from the surface. The Obukhov length, L , is defined as $L = -u_*^3 \left(\kappa \overline{w'_s T'} g T^{-1} \right)^{-1}$.

The third order moment (*TOM*) of the vertical wind, $\overline{w'^3}$, and the sensible heat flux, $\overline{w' T' w'}$, were computed with the same perturbation time scale and compared with their second order moment (*SOM*) to determine the direction of turbulent transport. The unrotated values of w_s were used for *TOM* and *SOM* to assure height consistency and being able to compare all heights on the main tower.

Mean values and the standard deviation of wind direction, φ , was computed by the method of Yamartino (1984).

For conditional averaging any parameter ϕ was averaged over all samples fulfilling a specific condition and is marked by angular brackets $[\phi]$.

The bulk Richardson number, $Ri_B = \frac{g}{\theta} \frac{\Delta\theta \Delta z^{-1}}{(\Delta u \Delta z^{-1})^2}$, was computed for the FODS transect with $\bar{\theta}$ being the mean layer temperature and $\Delta\theta \Delta z^{-1}$ and $\Delta u \Delta z^{-1}$ being the vertical potential temperature and wind speed gradients at each measurement point within the FODS transect. $[Ri_B]$ was calculated by the conditionally averaged quantities of $[\bar{\theta}]$, $[\Delta\theta \Delta z^{-1}]$, and $[\Delta u \Delta z^{-1}]$.

To analyze topographical effects on the flow, the Froude number, $F_L = v_{20m} N^{-1} L^{-1}$, was computed by using the Brunt-Väisälä frequency $N = \sqrt{g \theta_0^{-1} \Delta\theta (\Delta z)^{-1}}$ with v_{20m} being the North-South-component of the wind speed at 20 m agl, which is assumed to be the advective wind speed for winds flowing over the North shoulder, L a characteristic length scale of the topography, here the distance between the valley shoulder and the main tower in the valley, g the acceleration by gravitation, θ_0 the layer mean temperature, and $\Delta\theta (\Delta z)^{-1}$ the vertical temperature gradient. F_L decreases during conditions with a higher impact of the topography on the flow.

3 Summary of Thermal Submeso Fronts from Part 1

TSFs were detected using the spatial continuous FODS technique (cf. Pfister et al. (2020) & Sect. 4.1). The main characteristic of TSFs are the two air masses with contrasting characteristics (Fig. 1 & Fig. 13a). We refer to those air masses as layers as they are vertically stacked layers above the val-

ley bottom, hence, were be detected as such by the main tower, while on the North shoulder of the valley both are in contact with the ground and converge (Fig. 1). As the spatial scale of TSFs was 200–300 m (Fig. 13) and lasted between 40 s up to 1 hour they classify as submeso-scale motions. TSFs had a mean advective velocity of 0.2 ms^{-1} . The mean temperature drop from the cold to the warm air was 3.4 K (Fig. 2a). The cold-air layer most likely originates from non-local cold-air advection and has enough momentum to move uphill the Northern shoulder of the valley. At this location the warm-air layer is formed by topographically induced mixing elevating turbulence and mixing and thus increasing near-surface temperatures. Consequently, the topography played a major role in forming TSFs (Sect. 4.3.1). At the TSF boundary, the warm air is pushed upwards as the cold-air layer with high density is like a barrier. TSFs mostly occur during weak flows at 20 m a.g.l. and are absent during a strong and spatial homogeneous near-surface flow during which the cold-air layer is presumably eroded. The mean statistics presented can not give insight into the actual time evolution of TSFs, hence, when we refer to vanishing TSFs it means actually that they vanished or did not occur in the first place.

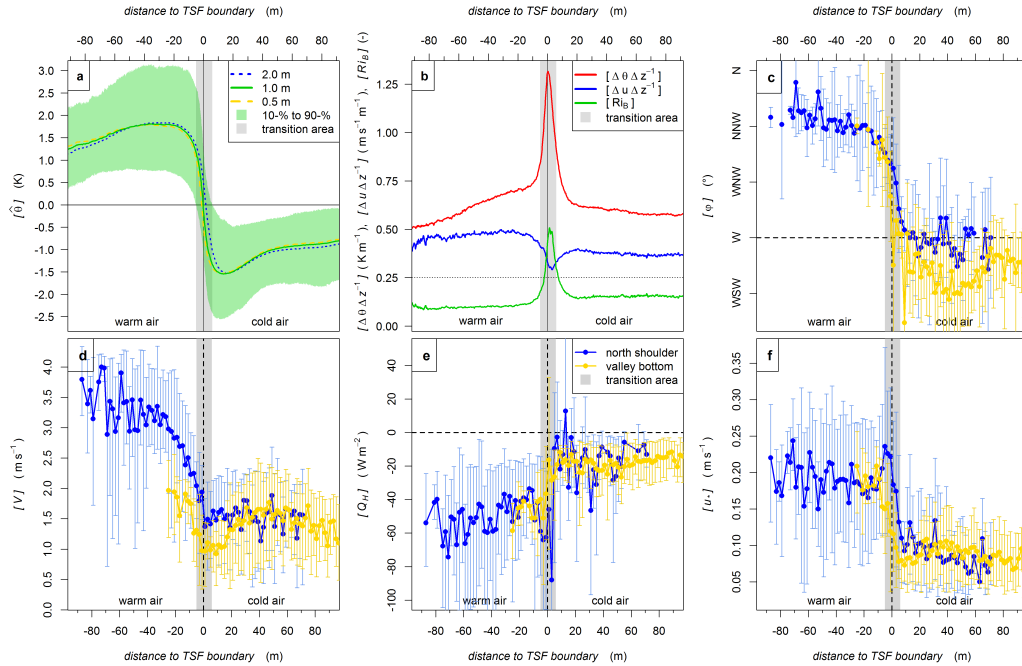


Fig. 2 Most important parameter describing thermal submeso fronts (1-min averages) which were conditionally averaged depending on their distance to the boundary of the fronts: fiber-optic measurements of (a) spatial temperature perturbation, $[\theta]$, and (b) the bulk Richardson number, $[Ri_B]$, derived from the ratio of buoyancy, $[\Delta\theta \Delta z^{-1}]$, to shear, $[\Delta u \Delta z^{-1}]$, as well as ultrasonic anemometer measurements showing (c) the mean wind direction, $[\varphi]$, (d) mean wind speed, $[V]$, (e) sensible heat flux, $[Q_H]$, and (f) friction velocity $[u_*]$.

154 The main feature of part 1 was the conditional averaging of different parameter
 155 depending on the distance of the measurement location to the TSF boundary.
 156 In Figure 2 we present the most important conditionally averaged parameter
 157 which led to the description of TSFs as summarized above and will be used in
 158 the discussion.

159 4 Results and Discussion

160 4.1 Detection of Thermal Submeso Fronts

161 As TSFs are formed by two competing air layers (Sect. 3), a passing TSF
 162 abruptly changed parameter like temperature, wind speed and direction as
 163 well as turbulence characteristics (Fig. 2). Accordingly, TSFs have a big im-
 164 pact on near-surface parameter and need to be detected accurately.

165 A frequently passing TSF can cause meandering which was observed in the
 166 time series two case studies (Fig. 15). For example Eulerian auto-correlation
 167 functions could be used for determining the occurrence of TSFs as they use
 168 wind directional change in combination with scalars like temperature or gases
 169 to detect meandering (Mortarini et al. 2019; Stefanello et al. 2020). Even
 170 though near-surface meandering was connected to TSFs, meandering at higher
 171 levels or within other field campaigns can also be caused by other types of motions
 172 like gravity waves. Another option for detecting TSFs could be a clustering
 173 method like presented by Vercauteren and Klein (2015) as the slow moving
 174 TSF enhances $\overline{w'w'}$ (not shown). There are also studies like Lang et al. (2018)
 175 which investigate the propagation of structure between towers by a cross-
 176 correlation function method, however, on rather long time scales (in this case
 177 20-min sampling windows).

178 Nevertheless, even if the described methods are successful, the location of
 179 observations within the topography is important. For example for the SCP
 180 experiment all observations on the South shoulder as well as stations near the
 181 valley bottom and on the 20-m tower missed TSFs completely or most of the
 182 time as the TSF did not pass them. The station A15 and A17 together were
 183 within the transition area of TSFs for 16.1% of all occurrences with TSFs.
 184 As only a passing TSF will be detected by a station the actual detection of
 185 TSFs by each point observation is even lower. Accordingly, even though the
 186 SCP experiment was a field campaign with a dense network, TSFs were mostly
 187 invisible even when using all point observations. Further, tracking the prop-
 188 agation and movement of TSFs between the stations was not possible as the
 189 stations were at least 40 m apart and thus the TSF could unknowingly remain
 190 between stations.

191 Consequently, only spatial continuous data like FODS can detect TSFs con-
 192 tinuously as even a dense network of ultrasonic anemometer miss the slow
 193 moving TSFs most of the time and thus can not determine their propagation
 194 and advective velocity.

195 4.2 Vertical Structure of Thermal Submeso Fronts

196 TSFs occurred during lower wind speeds, hence, during less turbulent trans-
 197 port as was also observed at all heights during TSFs as shown by the *SOM*
 198 and *TOM* of the vertical wind and the sensible heat flux (Fig. 3, green). Us-
 199 ing *SOM* and *TOM* the vertical extent of the cold-air layer during TSFs as
 200 estimated in part 1 could be confirmed. The lowest two levels showed very low
 201 $\overline{w'^3}$ (Fig. 3a) as well as $\overline{w'w'}$ (Fig. 3b), hence, there was little exchange with
 202 the layers above indicating a decoupled layer. At 2–5 m a.g.l. the turbulence
 203 strength of *SOM* increased with height, while *TOM* and thus the downward
 204 transport of them decreased. We conclude that those levels were affected by
 205 down-mixing of warm air eroding the cold-air layer. Accordingly, the cold-air
 206 layer has a vertical extent of 1–3 m depending on forcing conditions and is
 decoupled from the layers above inhibiting exchange processes.

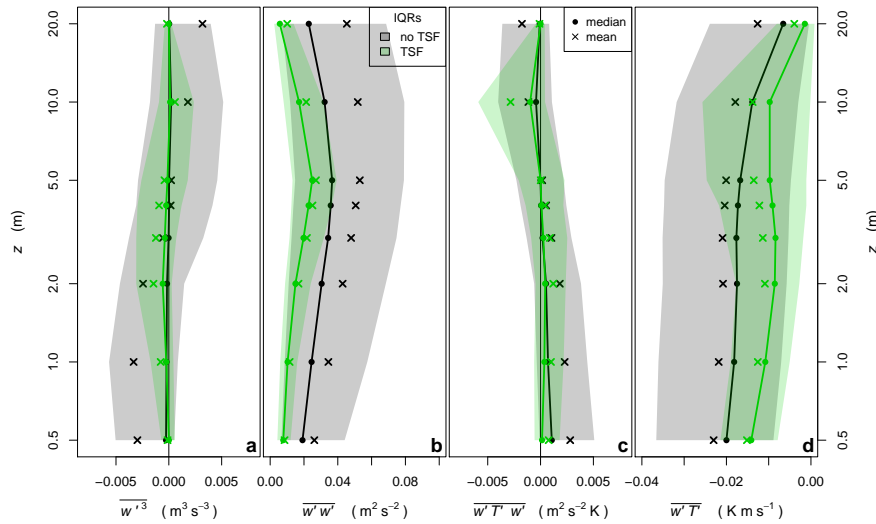


Fig. 3 Profiles of the third order moment of the (a) vertical wind speed, $\overline{w'^3}$, and (c) sensible heat flux, $\overline{w'T'w'}$, on the main tower and the corresponding profiles of the second order moments (b) $\overline{w'w'}$ and (d) $\overline{w'T'}$ during the occurrence and absence of TSFs (cf. legend).

207 The 10-m and 20-m levels on the main tower showed no preferential trans-
 208 port direction for $\overline{w'w'}$, but for $\overline{w'T'w'}$ (Fig. 3c) the 10-m station had a peak
 209 value in combination with strong $\overline{w'T'}$ (Fig. 3d), while the 20-m station had
 210 vanishing $\overline{w'T'w'}$ and $\overline{w'T'}$. Accordingly, the sensible heat flux was strongly
 211 transported upwards at 10 m to account for the strong decrease of $\overline{w'T'}$ to-
 212 wards 20 m. So we think that the 20-m station was in equilibrium with the
 213 regional flow while the 10-m station was adjusting to it. Given this interpreta-
 214 tion the warm-air layer is located between roughly 2 and 20 m a.g.l. depending
 215 on forcing conditions.

217 TSFs vanish during a strong and spatial homogeneous near-surface flow during
 218 which the cold-air layer is presumably eroded (Sect. 3). This can be confirmed

by *TOM* and *SOM* (Fig. 3, black). The turbulent transport $\overline{w'^3}$ and $\overline{w'T'w'}$ had a s-shaped profile with $z \approx 4\text{m}$ being the turning point. Above $z = 4\text{m}$ the transport of *SOM* was upward for continuity as the absolute values of $\overline{w'w'}$ and $\overline{w'T'}$ decreased dramatically from 10 m to 20 m. The strong negative value of $\overline{w'^3}$, especially near the ground, showed the efficient downward transport of turbulence. As $\overline{w'T'}$ near the surface was high and negative, the positive values of $\overline{w'T'w'}$ also indicated an efficient downward transport of the sensible heat flux. Consequently, during the absence of TSFs, cold-air layers are eroded and the boundary layer is well connected with the ground surface.

4.3 Thermal Submeso Front Forcings

4.3.1 Topography

Other studies confirm that the topography can induce mixing and thus enhance near-surface temperatures (Turnipseed et al. 2004), but the topography also plays an important role especially for cold-air drainage and pooling (Soler et al. 2002; Vosper and Brown 2008). During TSFs the warm-air layer is formed mechanically by topographically induced turbulent mixing on the North shoulder, while the cold-air layer is formed thermo-dynamically by cold-air drainage within the valley (Sect. 3). This was confirmed by the mean location of TSFs within the network (Fig. 13a) as well as by the elevated turbulence statistics at the plateau edge on the North shoulder (Fig. 13b). The air layers moved in different directions (Fig. 2c) as the cold air was following the topography while the warm-air layer was aligned with the regional flow (Fig. 13). The role of topography on near-surface flows was also numerically estimated by the Froude number, F_L . During TSFs, F_L were lower with a mean of 0.2 ± 0.1 and during their absence F_L were higher (0.7 ± 1.4). Similarly, the median of F_L was only half as high during TSFs than during their absence. As lower F_L are expected during an impact of the topography, we conclude that during TSFs the topographical effects on the flow are higher and that even gentle terrain has a significant impact on near-surface temperatures and the flow.

In summary, even in gentle terrain topographical effects should not be underestimated. Any field site with a similar geometry, hence, a valley being deep enough to provide some shelter and with a relatively sharp elevation change at the shoulder can potentially form TSFs. As an example, Mahrt (2019) describe submeso motions at three different field sites including TSFs within the SCP experiment.

4.3.2 Near-Surface Wind Speed

A minimum needed wind speed was expected for the topographically induced turbulent mixing forming the warm-air layer as well as for the erosion of TSFs. However, no minimum wind speed for the generation of the warm-air layer could be detected. Nevertheless, the maximum wind speed for which TSFs

persisted was $3.4 \pm 0.3 \text{ ms}^{-1}$ as determined by all 1-m stations except A9. Station A9 was located on the North shoulder and thus had higher wind speeds as it did experience less sheltering compared to stations within the valley. Below 3.4 ms^{-1} the wind speed distribution during the occurrence and absence of TSFs was similar (not shown). Accordingly, the occurrence of TSFs is related to but not determined by the wind speed strength.

TSFs do not move with the mean wind speed as the advective velocity of TSFs is an order of magnitude lower (cf. Sect. 3). But TSFs barely protruded into the valley during low wind speeds at A9, while they protruded far into the valley during high wind speed at A9 (Fig. 14). Consequently, the location of the TSF boundary was influenced by the wind speed strength. We assume that the horizontal extent of the warm-air layer and thus the TSFs movement is influenced by the near-surface wind pushing the TSF boundary down the Norther shoulder during increasing wind speeds. For testing this hypothesis, the correlation between the fluctuation of the North-South-component, $v_s - \overline{v_s}$, and the change in the TSF location, $x_{TSF} - \overline{x_{TSF}}$, was tested during each TSF event (Fig. 4a & b). The bar in this case means temporal average over the TSF duration. v_s was chosen for this analysis as it was aligned with the FODS transect and represented the TSF dislocation better than the mean wind speed. The stations A9 and A15 were chosen as both were located on the North shoulder. A change in v_s was correlated to a change in x_{TMF} for both stations with a high correlation. Therefore, the TSF dislocation was closely correlated to a change in v_s . A15 had the highest R^2 and lowest slope while A9 had a bit lower R^2 and a higher slope. The correlation is lower for A9 as this station was further away from the FODS transect where TSFs were detected and thus could not represent the TSF movement as well as A15. From this we conclude TSFs do not move with the wind, but TSFs respond to a change in wind speed which is aligned with the observations of Lang et al. (2018).

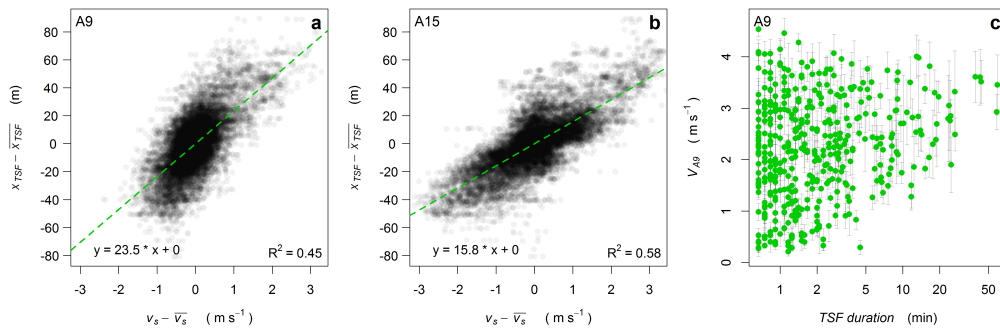


Fig. 4 Variation of the North-South-component of the wind, $v_s - \overline{v_s}$, plotted against the variation of the TSF boundary location, $x_{TSF} - \overline{x_{TSF}}$, determined during each TSF event for (a) station A9 on North shoulder and (b) station A15 half-way uphill on the North shoulder. (c) Duration of TSF even plotted against the mean wind speed at A9

Due to this correlation we also checked if the duration of TSFs was related

to the mean wind speed (Fig. 4c). For the longest duration of TSFs the wind speed was higher, but for short lasting TSFs high as well as low wind speeds were observed (same results for A15, not shown). Accordingly, at least TSF with a longer duration required rather high wind speeds, but there was no clear relation between wind speed and TSF duration.

As discussed above high wind speeds cause topographically induced mixing and thus generate the warm-air layer and push the TSF boundary further down the shoulder. So we conclude that especially for the warm-air layer the wind speed plays an important role as the TSF boundary location as well as the duration is related to the near-surface wind speed.

4.3.3 Synoptic Wind Speed and Direction

Larger-scale forcings for the formation of TSFs were analyzed with a wind profiler (SODAR) and the 20 m high main tower. During TSFs maximum wind speeds in the lowest levels from 0.5 m to 100 m ranged from 2.4 ms^{-1} up to 12.4 ms^{-1} . TSFs vanished for wind speeds higher than 12.4 ms^{-1} in the lowest 100 m. But there was no clear wind speed threshold for TSFs at any level as the inter-quartile ranges of V during the occurrence and absence of TSFs overlapped (Fig. 5a). No specific flow regime, like low level jets, were connected to the occurrence of TSFs as no near-surface peak being higher than 10 ms^{-1} in the lowest 100 m could be identified as for example defined by Banta et al. (2004).

Even though the SODAR data showed no wind speed threshold, differences in the wind speed shear, wind profile and synoptic wind direction were detected, hence, we think that the synoptic wind may play a role for the formation of TSFs.

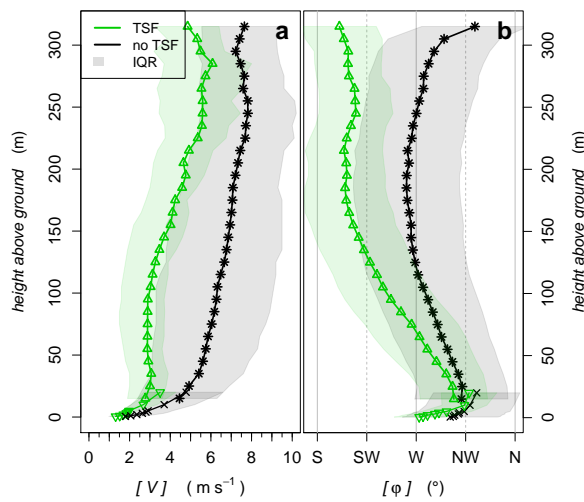


Fig. 5 Conditional averaging of (a) horizontal wind speed $[V]$ and (b) wind direction $[\varphi]$ during the occurrence (green) and absence of TSFs (black). down-pointing triangles & crosses: 20-m tower; up-pointing triangles & stars: wind profiler; shaded areas: inter-quartile range of $[V]$ and standard deviation of $[\varphi]$.

During the absence of TSFs the wind speed profile indicated a coupled boundary layer. The wind profile followed an exponential function and the main tower and SODAR data matched (Fig. 5a, black line) even though they were 100 m apart, suggesting that horizontally wind speed and direction were spatially homogeneous. Besides, the larger-scale flow changed the wind direction from West to North-West near the surface. The change in wind direction was probably caused by the regional topography being oriented North-West and thus forcing near-surface winds into this direction.

Usually a exponential wind speed profile can be assumed, however, during TSFs wind speed from 50 m to 100 m a.g.l. was constant and only gradually increased for higher levels (Fig. 5a, green line). Further, the mean wind speed at all levels was lower during the occurrence than during the absence of TSFs. Significant wind directional shear was evident, as the wind direction turned from South-West at levels higher than 155 m to North-West at 20 m and then to West near the surface (Fig. 5b). Further, wind speed and direction were spatially inhomogeneous as the tower and SODAR data did not match.

From these findings and Section 4.2, we derive four layers during TSFs. The near-surface layer below ≈ 2 m is influenced by the cold-air layer following the topography, between 2 m and 10 m the warm-air layer is detected with wind directions from North-West following the regional topography, a transition layer is established between 10 m and 150 m where the wind direction shifts from North-West to South-West with spatially homogeneous wind speed, and for heights > 150 m the synoptically forced layer is found with wind direction South-West.

4.3.4 Radiation and Static Stability

The radiation balance during TSFs was investigated assuming the formation of a cold-air layer during low incoming longwave radiation, $L\downarrow$, or high net radiation, ΔL . But again no clear threshold for the formation of TSFs could be determined. For the same $L\downarrow$ or ΔL , instances with and without TSFs could be identified (Fig. 6a). Nevertheless, TSFs most likely occurred for $L\downarrow$ around -250 Wm^{-2} , and TSFs mostly vanished for $L\downarrow < -280 \text{ Wm}^{-2}$ (Fig. 6a). For ΔL , TSFs mostly occurred around 58 Wm^{-2} and for values higher 76 Wm^{-2} no TSFs could be identified (Fig. 6b).

Static stability, $\Delta_z\theta$, was derived from the temperature difference between 15 m and 0.5 m at the main tower. $\Delta_z\theta$ is rather a response of the boundary layer than a forcing, but $\Delta_z\theta$ could be used as a diagnostic for TSFs. $\Delta_z\theta$ were elevated during TSFs due to their vertical structure with the cold-air layer at the bottom and warm-air layer on top. We would have assumed a correlation between radiative forcing and static stability with increasing stability during less $L\downarrow$ or strong ΔL , however, neither is the case regardless of the occurrence or absence of TSFs. Accordingly, we conclude that the source of cold air within the valley is non-local. Cold air could be advected from outside the valley also transporting enough momentum pushing cold air uphill against the buoyancy force. Similar observations were made by Mahrt (2010) during FLOSSII and

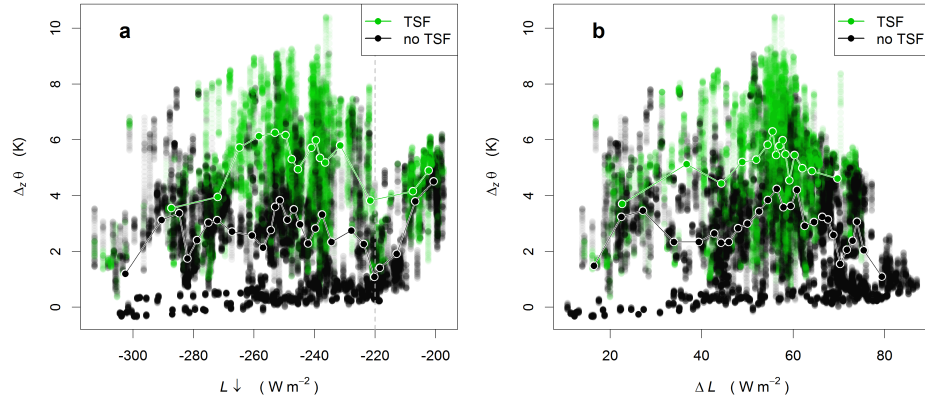


Fig. 6 Incoming longwave radiation, L_{\downarrow} , (a) and net longwave radiation, ΔL , (b) plotted against static stability, $\Delta_z\theta$, as derived from the temperature difference between 15 m and 0.5 m at the main tower. Equally sized bin averages were added for the occurrence and absence of TSFs (cf. legend).

described in detail for a case study during SCP (Mahrt et al. 2020). This would also explain why the TSF boundary was mainly found halfway uphill on the north shoulder and the coldest air was found right next to the TSF boundary. The source of cold air could not be clarified, however, nearby terrain featuring a tall and broad hill could provide enough cold-air formation and corresponding drainage.

4.4 Implications for the Stable Boundary Layer

4.4.1 Static Stability and Near-surface Sensible Heat Flux

The stable boundary layer is usually classified by the inversion strength, which can be described by $\Delta_z\theta$. To this analysis we also added wind regimes as introduced by Sun et al. (2012) being determined by the relation of the horizontal wind speed, V , and friction velocity, u_* , for night time data at the corresponding location. During SCP, $\Delta_z\theta$ showed distinct differences during the occurrence and absence of TSFs in contrast to near-surface wind regime (Fig. 7a) or radiation (Fig. 6) or their combination (Fig. 16). $\Delta_z\theta$ within each wind regime was barely different (Fig. 7a), however, when adding the knowledge about TSFs, subsets even within each wind regime were created with higher $\Delta_z\theta$ during TSFs. The high $\Delta_z\theta$, especially within the strong-wind regime but also within the weak-wind regime, was most likely caused by the vertical structure of TSFs with the cold-air layer at the valley bottom and the warm-air layer on top (Fig. 1 & Sect. 4.2). This is contra intuitive as the high correlation between horizontal wind speed and turbulence during the strong-wind regime usually suggests a well coupled boundary layer, however, it is actually the opposite during TSFs with the decoupled cold-air layer. Consequently, a near-surface strong-wind regime does not necessarily reflect a well-coupled boundary layer.

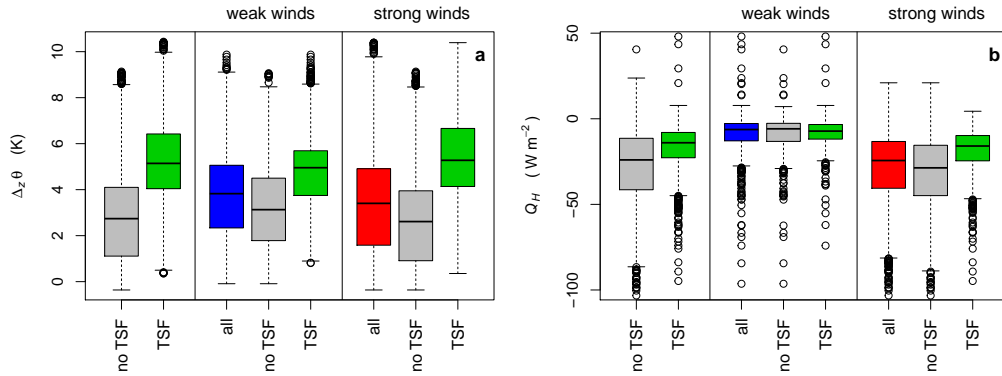


Fig. 7 Boxplots of (a) static stability, $\Delta_z\theta$, and (b) sensible heat flux, Q_H , for the 1-m station on the main tower. The boxplots are subset by the occurrence of TSFs as well as wind regimes as introduced by Sun et al. (2012) (cf. x-axis).

Choosing the levels over which to calculate bulk parameters like $\Delta_z\theta$ is critical when describing the boundary layer. Especially when determining the static stability over several meter. In our study the strong static stability did not indicate a strong cold-air pool, it indicated the occurrence of TSFs as we accidentally chose the two levels for $\Delta_z\theta$ which were within the two air layer with opposing characteristics. In other field studies there could be more vertical layers, especially when having a more complex geometry of the topography, making the right choice for $\Delta_z\theta$ even more important.

Near-surface static stability changed depending within which air layer of the TSFs the station was located and even showed peak values when a TSF was passing (Fig. 2b). Accordingly, TSFs impacted near-surface static stability, but mainly on the North shoulder. We conclude that besides choosing the right levels for computing meaningful $\Delta_z\theta$ also the station location is important. Parameters like dynamic stability as derived by Ri_B do not offer an alternative for $\Delta_z\theta$ due to the impact of TSFs on near-surface static stability. TSFs altered Ri_B (Fig. 2b) and its relationship to Q_H (Fig. 8). The relationship between dynamic stability and Q_H is commonly used for turbulent exchange in land models (Lapo et al. 2019) or also other studies (Brotzge and Crawford 2000). However, within the transition area of TSFs the relation between Ri_B and Q_H was different. The air layers converged and created strong static stability as well as a low wind speed shear within the transition area leading to high Ri_B , hence, a strong dynamic stability (Fig. 2b). High Ri_B usually indicate low Q_H due to the strong dynamic stability restricting vertical turbulent exchange and would adjust Q_H accordingly in land models or when adjusting Q_H by stability functions. But the measured data showed peak values in u_* and Q_H (Fig. 2e & f). Consequently, the concept of dynamic stability misleads interpretation of the flux when a TSF is passing.

The slow moving TSFs altered the near-surface sensible heat flux within a few minutes and led to a mean drop of 30 W m^{-2} when passing (Fig. 2e). As TSFs were semi-stationary moving up- and downhill the valley shoulder they

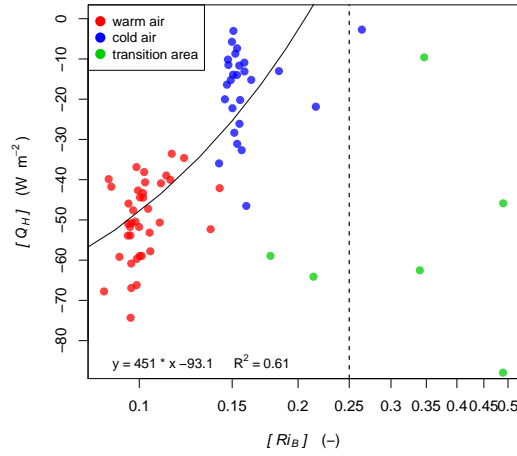


Fig. 8 Bulk Richardson number, Ri_B , plotted against the sensible heat flux, Q_H , conditionally averaged with regard to the distance to the thermal submeso front (TSF) boundary. Colors highlight the different air layers of the TSFs (cf. legend).

enhanced or reduced the sensible heat flux intermittently. Consequently, TSFs dictate the behaviour of near-surface fluxes, highlighting their importance for the SBL. But when using only the information about the occurrence or absence of TSFs, the sensible heat flux at 1m a.g.l. on the main tower did not show a distinctive difference (Fig. 7b). The boxplots did not differ depending on TSF presence as Q_H ranges from low values within the cold-air layer up to high values within the warm-air layer and even peak values within the transition area. Consequently, especially for the near-surface Q_H , it is important to not only know whether TSFs occurred but to also know their location, which requires spatially continuous data.

In summary, it is not sufficient for models to prescribe surface temperature as suggested by others (e.g., Basu et al. (2008)) especially for sites where TSFs occur. TSFs and their effect on turbulent exchange are not distinctly described by for example $\Delta_z \theta$ or Ri_B . Models struggle to represent intermittent turbulence as generated by TSFs and thus further investigations of submeso motions using spatially continuous data are needed.

4.4.2 Boundary Layer Regimes during Thermal Submeso Fronts

As shown above, TSFs could not be tied to a single local or non-local forcing. Nevertheless, we tried if TSFs occur during specific boundary layer regimes.

The approach of Pfister et al. (2019) was tested which combined radiative forcing, wind regime, and static stability. Unfortunately, as TSFs were not influenced by radiative forcing nor by the wind regime (see discussion below), even the above mentioned combination of parameter could not determine a specific boundary layer regime during which TSFs occurred. TSFs occurred throughout all boundary layer regimes with statically stable conditions (not shown). We summarize four possible reasons why this approach failed. Firstly, during TSFs the formation of the air layers are mostly independent from each other.

Topographically induced turbulence is generated irrespective of radiative forcing, while vice versa the cold-air layer can form within the valley independent of the wind speed strength as long as it is not eroding the cold-air layer. Secondly, the warm-air layer can persist for an unknown amount of time during periods with weak winds. Similarly, the cold-air layer can persist even into periods with less radiative cooling, especially when being advected. Thirdly, as explained earlier, one observational point can not reveal a threshold for the occurrence of TSFs as they consist of two distinct air layers. Depending on the location of a measurement, a station was either within the warm-air or cold-air layer showing one of the properties. Due to this there is a mismatch between the bulk and point measure. This shows when looking at static stability and the wind regime. The static stability is a bulk measure between two levels. In our case, like in many other field studies, it was taken at the main tower at the valley bottom in the center of the network. At the same time the wind regime is determined locally for a specific height and location, hence, is a point measure. As TSFs move through the network, the relation between V and u_* and thus the wind regime can change suddenly at a point measure depending on in which air layer of the TSFs the station was located and not depending on how strong the bulk static stability was which was strong throughout the occurrence of TSFs. Fourthly, another point of consideration, which was not further investigated in this study, is the adjustment time scale between the change in bulk forcing to a change in turbulence (Mahrt and Thomas 2016). Maybe a more clear relation between for example synoptic flow and the occurrence of TSFs emerge when accounting for an adjustment time scale.

An established and commonly used method to characterize the boundary layer are near-surface wind regimes as introduced by the work of Sun et al. (2012). But due to the rather broad wind speed range during which TSFs occurred (Sect. 4.3.2), TSFs were not related to a specific wind regime. Nevertheless, we wanted to set the air layers of TSFs into the context of wind regimes. For instance, it is possible that the warm-air layer with strong V and u_* (Fig. 2d & f) could be confined to the strong-wind regime, while the cold-air layer with cold-air drainage could be confined to the weak-wind regime. If this is true, also the spatial extent of each TSF layer within the network could be determined. Besides, also the transition area was investigated if it falls into a specific regime.

Following Sun et al. (2012), a threshold value of 1.6 ms^{-1} was determined for the night time 1-min data of the station A15 (2 m a.g.l.) irrespective of TSFs as described in detail in (Pfister et al. 2019). The warm-air layer had a wind speed range from 0.5 ms^{-1} up to 4.4 ms^{-1} , while the cold-air layer ranged from 0.3 ms^{-1} up to 2.5 ms^{-1} (Fig. 9), hence, the layers were not confined to one wind regime. For the warm-air layer 91% of the data was within the strong-wind regime, while for the cold-air layer 47% within the same regime, which is higher than expected. Due to this overlap, we conclude that a simple threshold can not separate the air layers from each other.

Further, the warm- and cold-air layer each showed a specific relation between

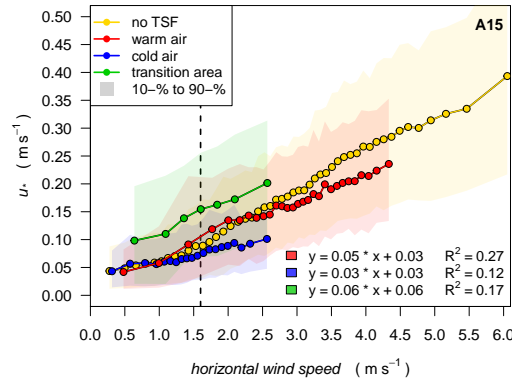


Fig. 9 Relation of horizontal wind speed to friction velocity, u_* , for each air layer and the transition area of TSFs (cf. legend). vertical line: threshold value separating weak-wind and strong-wind regime following the work of Sun et al. (2012); points: equally sized bin-averages.

484 V and u_* with a higher slope for the warm-air layer than for the cold-air
 485 layer. We speculate that within the cold-air layer thermo-dynamics supersede
 486 the mechanical generation of turbulence and thus u_* only slowly increased with
 487 V , while for the well mixed warm-air layer the strong correlation between V
 488 and u_* persisted even during rather weak winds. So especially the cold-air layer
 489 occurring during wind speeds way beyond the wind speed threshold show that
 490 the air layers cannot be separated by a simple wind speed threshold.

491 The transition area of TSFs revealed a similar slope as the warm-air layer,
 492 but with a higher offset as can be expected from the peak values in u_* found
 493 within the transition area (Fig. 2f). Within the transition area u_* was also in-
 494 termittently enhanced during a passing TSF as observed within the time series
 495 of two case studies (Fig. 17). Comparing the conditions within the transition
 496 area of TSFs with the wind regimes of Sun et al. (2012) the transition area
 497 qualifies as regime 3, however, it spans both wind regimes equally not only
 498 the weak-wind regime. The intermittent turbulence within the transition area
 499 was caused by the convergence of both air layers and as a result we argue that
 500 the turbulence within the transition area is a bottom-up process and not an
 501 intermittent down-mixing of turbulence by larger-scale eddies.

502 The above described wind regime does not incorporate a specific thermal
 503 regime for determining the wind regime. Some studies report a change in min-
 504 imum needed wind speed to sustain turbulence near the surface (Van de Wiel
 505 et al. 2017; Maroneze et al. 2019) or more specifically a change in wind speed
 506 threshold separating the weak-wind from the strong-wind regime depending
 507 on thermal regime (Sun et al. 2020). As elevated static stability was observed
 508 during TSFs (Fig. 7a & Fig. 6) we separated the data set into stronger static
 509 stability during the occurrence of TSFs and weaker static stability during the
 510 absence of TSFs and determined the wind speed threshold.

511 However, even when choosing a specific thermal regime as it occurred during
 512 TSFs, the wind speed threshold did not change (Fig. 10). This supports our
 513 earlier discussion that the relation of a bulk measure like static stability and

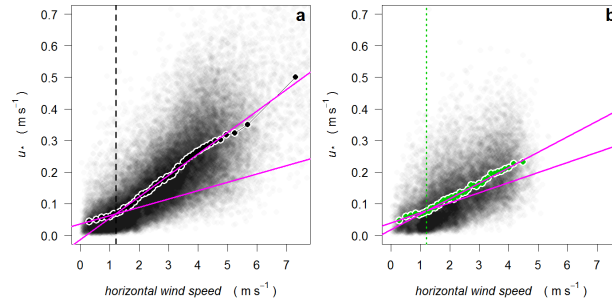


Fig. 10 Scatter-plot of horizontal wind speed, V , and friction velocity, u_* , for determining the wind speed threshold separating the weak- and strong-wind regime. This was done for (a) weak static stability during the absence of TSFs (black) and for (b) elevated static stability during the occurrence of TSFs (green). Equally sized bin-averages were added (dotted line) as well as the linear correlation lines below (magenta lines) and above the wind speed threshold (vertical lines).

a point measure like the wind regime is weak during TSFs. So even when considering static stability for the determination of wind regimes, we could not determine a specific wind regime for TSFs.

One could argue that the used static stability was biased by the choice of using the occurrence of TSFs. So we also used the thermal regimes as defined by Mahrt (1998) separating the SBL into weakly and very stable. We assumed that the cold-air layer with a weak relation between V and u_* should represent the very stable regime, while the warm-air layer with a stronger relationship should represent the weakly stable regime. If the air layer mostly fall within one thermal regime and thus change the wind speed threshold, the separation of the two distinct air layers should be possible.

The air layers of TSFs were not confined to one thermal regime, but they showed different correlations between z/L and $\overline{w'T'}$ (Fig. 11). Substantial scatter around the bin averages were observed which was most likely caused by differences in radiative or non-local forcings like the regional flow or varying and unknown adjustment time scales to that. We acknowledge that the cold-air layer had more points within the very stable regime while the warm-air layer was mostly within the transition regime, but the air layers were not characteristic for just one regime. Even though the cold-air layer showed a constant low slope between V and u_* , the cold-air layer did not represent the very stable regime. Vice versa this applied to the warm-air layer and weakly stable regime. Out of curiosity, we also investigated the relation between z/L and $\overline{w'T'}$ depending the occurrence of TSFs and depending on wind regime. The relation changes during the occurrence of TSFs and the weakly stable regime would have a broader range (Fig. 18a). For the strong-wind regime most points were detected within the weakly stable and transition, while the weak-wind regimes had most points within the transition and very stable regime (Fig. 18b), but there was no clear pattern. From this we conclude that at least at the SCP site the wind regime change does not co-occur with a change from the weakly stable to the very stable regime. Further, we think that even if the thermal

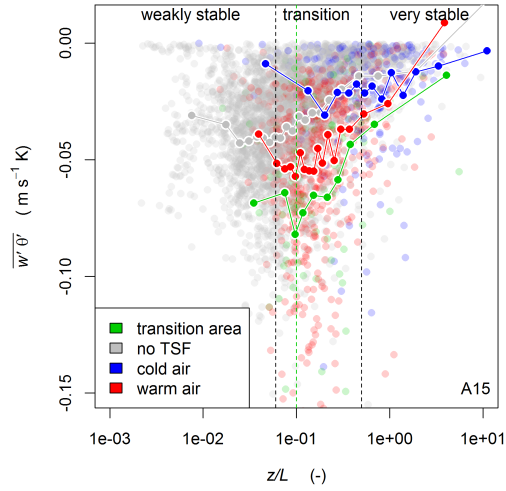


Fig. 11 Thermal regimes as defined by Mahrt (1998) separating the boundary layer into the weakly and very stable regime by using the Obukhov length, z/L , and kinematic sensible heat flux, $\overline{w'\theta'}$. Equally-sized bin averages (dotted lines) were computed for the different air layers of thermal submeso fronts (cf. legend). Vertical lines and text indicate the regime change from weak to very stable.

regimes change the wind speed threshold, this cannot be represented by a regime change determined by z/L or bulk static stability as many confounding and interdependent factors are at work creating substantial scatter around mean values.

In summary, due to the specific and antagonistic characteristics of the air layers of TSFs causing strong spatial perturbations it is unlikely that even a combination of thermal and wind regimes is able to determine a regime which is characteristic for TSFs. Near-surface features measured by a point observation will reflect the corresponding air layer it is located in or the change from one layer to the other when applying time series analysis. But depending on the physical location within the valley a point observation will spend most of the time in either one layer or has a few occasions when the TSFs will pass, but as shown in the manuscript, most of the time the location of the front is unknown unless spatial continuous data is used. TSFs impact the SBL characteristics significantly, hence, need to be considered when characterizing the boundary layer. Unless spatial perturbation can be added to the surface-layer condition or non-local forcing like cold-air advection added to the regime definition, we conclude there is no point-based regime which can determine the occurrence of TSFs.

4.5 Recommendations and Thoughts for further Studies

For this analysis, we were missing observation from outside the valley to for example determine the source for cold-air advection, while at the same time

not all stations within the valley would have been necessary. Accordingly, for future deployments we would recommend the following:

- Nested networks observing the boundary layer in the best possible three-dimensional way by for example combining a wind profiler with tower data (as high as possible), gradient of instrument density with the highest density along main topographical features (cross-valley, down-valley, vertical), and decreasing density outside the valley.
- Small studies prior to the field campaign to determine the topographical features which influence the boundary layer. If TSFs were modified locally or advected could not be answered by the presented study due to the lack of spatial continuous data outside the valley. If adding more stations or spatial continuous data outside the valley, an investigation of the evolution of TSFs should be possible. Another study focusing on the evolution of TSFs should be beneficial for experimentalists and modellers.
- If possible spatial continuous data should be applied horizontally and vertically and combined with sonic anemometer measurements as done in Pfister et al. (2020).
- Spatial continuous data like FODS is also limited in its application. Even a three-dimensional setup like for example Zeeman et al. (2015) can track cold-air motions, however, does not show the origin of the cold air. Further, FODS is limited in its spatial application (maximum length of fiber-optic cable is 5–10 km per device). This needs to be kept in mind when trying to use FODS to its full potential.
- For modelling the stable boundary layer we recommend to focus on incorporating topographical effects like mixing at edges and local as well as non-local cold-air drainage.

5 Conclusion

TSFs were detected during the SCP experiment, being a unique study with a near-surface network of 27 ultrasonic anemometer stations, a wind profiler, and fiber-optic distributed temperature sensing. TSFs were frequently occurring within the stable boundary layer and were generated by the gentle topography creating two contrasting air layers. The warm-air layer is mechanically generated by topographically induced mixing consistently elevating near-surface temperatures at the plateau-edge, while the cold-air layer is thermodynamically driven by topographically induced cold-air drainage decreasing near-surface temperatures in the valley. Accordingly, even in this gentle terrain, the impact of topography is bigger than usually anticipated. Further, TSFs can be expected at any field site with a similar geometry.

We could not find a single local forcing or combination of them determining the occurrence of TSFs nor was a clear connection between synoptic flow and TSFs found. Regardless, TSFs impact the stable boundary layer significantly:

- the advective velocity of TSFs was an order of magnitude lower than the mean wind which renders ergodicity assumptions invalid

- TSFs can cause mean drops of 30 Wm^{-2} in Q_H within a minute or less when passing a station and thus cause intermittent turbulence
- the vertical structure of TSFs increase static stability beyond the capability of radiative forcing
- the decoupled boundary layer during TSFs renders the use of flux-gradient similarity theory invalid within the valley where the warm-air layer lays on top of the cold-air layer as well as within the transition area of TSFs
- no distinct relation to wind or thermal regimes exists for TSFs

The boundary layer community so far usually classifies the stable boundary layer by flow conditions (e.g. LLJ or geostrophic winds), thermal regimes, radiative forcing, or a combination of these. In these approaches, the boundary layer is assumed to be a bottom-up or top-down controlled column. However, the vertical properties of TSFs and the connection between the distinct horizontal layers invalidates this vertical conceptualization. As a result, point observations need to be put into the spatial context of their surroundings as well as corresponding submeso motions. The use of a network of point observations is insufficient as they miss submeso motions most of the time as discussed above. We recommend the use of spatially continuous data in the horizontal as well as vertical in combination with a nested network of station within and outside the investigated valley. Future studies need to consider the shortcomings of point observations without the benefits of spatially continuous data.

References

- Anfossi D, Oetl D, Degrazia G, Goulart A (2005) An Analysis Of Sonic Anemometer Observations In Low Wind Speed Conditions. *Boundary-Layer Meteorol* 114(1):179–203, DOI 10.1007/s10546-004-1984-4
- Banta RM, Darby LS, Fast JD, Pinto JO, Whiteman CD, Shaw WJ, Orr BW (2004) Nocturnal low-level jet in a mountain basin complex. Part I: Evolution and effects on local flows. *J Appl Meteorol* 43(10):1348–1365, DOI 10.1175/JAM2142.1
- Basu S, Holtslag AA, Wiel BJ, Moene AF, Steeneveld GJ (2008) An inconvenient "truth" about using sensible heat flux as a surface boundary condition in models under stably stratified regimes. *Acta Geophys* 56(1):88–99, DOI 10.2478/s11600-007-0038-y
- Brotzge JA, Crawford KC (2000) Estimating Sensible Heat Flux from the Oklahoma Mesonet. *J Appl Meteorol* 39(1):102–116, DOI 10.1175/1520-0450(2000)039<0102:ESHFFT>2.0.CO;2
- Cava D, Mortarini L, Anfossi D, Giostra U (2019a) Interaction of Submeso Motions in the Antarctic Stable Boundary Layer. *Boundary-Layer Meteorol* 171(2):151–173, DOI 10.1007/s10546-019-00426-7
- Cava D, Mortarini L, Giostra U, Acevedo O, Katul G (2019b) Submeso Motions and Intermittent Turbulence Across a Nocturnal Low-Level Jet: A

- Self-Organized Criticality Analogy. *Boundary-Layer Meteorol* 172(1):17–43, DOI 10.1007/s10546-019-00441-8
- Kang Y, Belušić D, Smith-Miles K (2014) Detecting and Classifying Events in Noisy Time Series. *J Atmos Sci* 71(3):1090–1104, DOI 10.1175/JAS-D-13-0182.1
- Kang Y, Belušić D, Smith-Miles K (2015) Classes of structures in the stable atmospheric boundary layer. *Q J R Meteorol Soc* 141(691):2057–2069, DOI 10.1002/qj.2501
- Lang F, Belušić D, Siems S (2018) Observations of Wind-Direction Variability in the Nocturnal Boundary Layer. *Boundary-Layer Meteorol* 166(1):51–68, DOI 10.1007/s10546-017-0296-4
- Lapo K, Nijssen B, Lundquist JD (2019) Evaluation of Turbulence Stability Schemes of Land Models for Stable Conditions. *J Geophys Res Atmos* 124(6):3072–3089, DOI 10.1029/2018JD028970
- Mahrt L (1998) Nocturnal Boundary-Layer Regimes. *Boundary-Layer Meteorol* 88(2):255–278, DOI 10.1023/A:1001171313493
- Mahrt L (2010) Common microfronts and other solitary events in the nocturnal boundary layer. *Q J R Meteorol Soc* 136(652):1712–1722, DOI 10.1002/qj.694
- Mahrt L (2019) Microfronts in the nocturnal boundary layer. *Q J R Meteorol Soc* 145(719):546–562, DOI 10.1002/qj.3451
- Mahrt L, Thomas CK (2016) Surface Stress with Non-stationary Weak Winds and Stable Stratification. *Boundary-Layer Meteorol* 159(1):3–21, DOI 10.1007/s10546-015-0111-z
- Mahrt L, Pfister L, Thomas CK (2020) Small-Scale Variability in the Nocturnal Boundary Layer. *Boundary-Layer Meteorol* 174(1):81–98, DOI 10.1007/s10546-019-00476-x
- Maroneze R, Acevedo OC, Costa FD, Puhales FS, Demarco G, Mortarini L (2019) The nocturnal boundary layer transition from weakly to very stable. Part II: Numerical simulation with a secondorder model. *Q J R Meteorol Soc* 145(725):3593–3608, DOI 10.1002/qj.3643
- Mortarini L, Cava D, Giostra U, Acevedo O, Nogueira Martins LG, Soares de Oliveira PE, Anfossi D (2018) Observations of submeso motions and intermittent turbulent mixing across a low level jet with a 132m tower. *Q J R Meteorol Soc* 144(710):172–183
- Mortarini L, Cava D, Giostra U, Costa FD, Degrazia G, Anfossi D, Acevedo O (2019) Horizontal Meandering as a Distinctive Feature of the Stable Boundary Layer. *J Atmos Sci* 76(10):3029–3046, DOI 10.1175/JAS-D-18-0280.1
- Orlanski I (1975) A rational subdivision of scales for atmospheric processes. *Bull Am Meteorol Soc* 56(5):527–530
- Pfister L, Lapo K, Sayde C, Selker J, Mahrt L, Thomas CK (2019) Classifying the nocturnal atmospheric boundary layer into temperature and flow regimes. *Q J R Meteorol Soc* 145(721):1515–1534, DOI 10.1002/qj.3508
- Pfister L, Lapo K, Mahrt L, Thomas CK (2020) Thermal submeso motions in the nocturnal stable boundary layer - Part 1: Detection & mean statistics. *Boundary-Layer Meteorol* X(X):X

- Soler M, Infante C, Buenestado P, Mahrt L (2002) Observations of nocturnal drainage flow in a shallow gully. *Boundary-Layer Meteorol* 105(2):253–273, DOI 10.1023/A:1019910622806
- Stefanello M, Cava D, Giostra U, Acevedo O, Degrazia G, Anfossi D, Mortarini L (2020) Influence of submeso motions on scalar oscillations and surface energy balance. *Q J R Meteorol Soc* 146(727):889–903, DOI 10.1002/qj.3714
- Stiperski I, Calaf M (2018) Dependence of near-surface similarity scaling on the anisotropy of atmospheric turbulence. *Q J R Meteorol Soc* 144(712):641–657, DOI 10.1002/qj.3224
- Sun J, Mahrt L, Banta RM, Pichugina YL (2012) Turbulence Regimes and Turbulence Intermittency in the Stable Boundary Layer during CASES-99. *J Atmos Sci* 69(1):338–351, DOI 10.1175/JAS-D-11-082.1
- Sun J, Takle ES, Acevedo OC (2020) Understanding Physical Processes Represented by the MoninObukhov Bulk Formula for Momentum Transfer. *Boundary-Layer Meteorol* 177(1):69–95, DOI 10.1007/s10546-020-00546-5
- Turnipseed AA, Anderson DE, Burns S, Blanken PD, Monson RK (2004) Airflows and turbulent flux measurements in mountainous terrain. *Agric For Meteorol* 125(3-4):187–205, DOI 10.1016/j.agrformet.2004.04.007
- Van de Wiel BJH, Vignon E, Baas P, van Hooijdonk IGS, van der Linden SJA, Antoon van Hooft J, Bosveld FC, de Roode SR, Moene AF, Genthon C (2017) Regime Transitions in Near-Surface Temperature Inversions: A Conceptual Model. *J Atmos Sci* 74(4):1057–1073, DOI 10.1175/JAS-D-16-0180.1
- Vercauteren N, Klein R (2015) A Clustering Method to Characterize Intermittent Bursts of Turbulence and Interaction with Submesomotions in the Stable Boundary Layer. *J Atmos Sci* 72(4):1504–1517, DOI 10.1175/JAS-D-14-0115.1
- Vercauteren N, Boyko V, Faranda D, Stiperski I (2019) Scale interactions and anisotropy in stable boundary layers. *Q J R Meteorol Soc* 145(722):1799–1813, DOI 10.1002/qj.3524
- Vosper SB, Brown aR (2008) Numerical simulations of sheltering in Valleys: The formation of nighttime cold-air pools. *Boundary-Layer Meteorol* 127(3):429–448, DOI 10.1007/s10546-008-9272-3
- Yamartino RJ (1984) A Comparison of Several Single-Pass Estimators of the Standard Deviation of Wind Direction. *J Clim Appl Meteorol* 23(9):1362–1366, DOI 10.1175/1520-0450(1984)023<1362:ACOSPE>2.0.CO;2
- Zeeman MJ, Selker JS, Thomas CK (2015) Near-Surface Motion in the Nocturnal, Stable Boundary Layer Observed with Fibre-Optic Distributed Temperature Sensing. *Boundary-Layer Meteorol* 154(2):189–205, DOI 10.1007/s10546-014-9972-9

Appendix

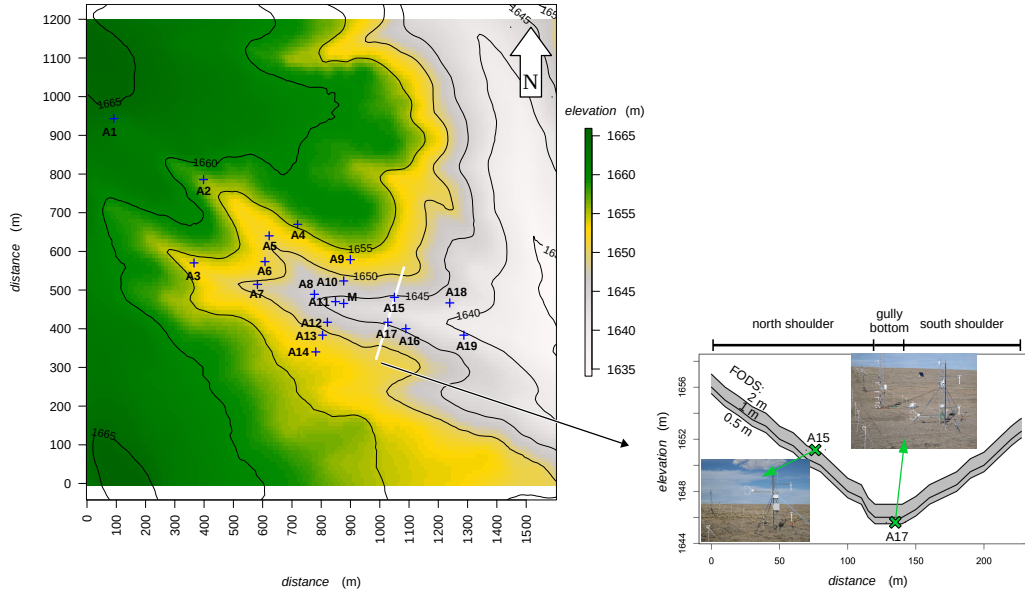


Fig. 12 Left: Topographical overview of field site with all ultrasonic anemometer stations (A1–A19), the 20 m high main tower (M), and the fibre-optic distributed sensing transect (white line). Right: Cross-valley view of the fiber-optic transect showing its length and elevation.

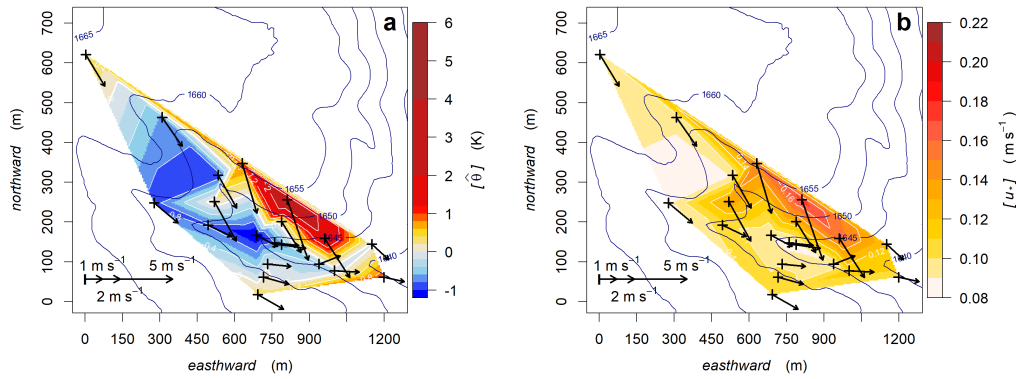


Fig. 13 Overview of field site with elevation shown by contour lines (dark blue). (a) The mean spatial temperature perturbation, $[\hat{\theta}]$, and (b) the mean friction velocity, $[u_*]$, during the occurrence of TSFs is added by filled contour lines (cf. legend).

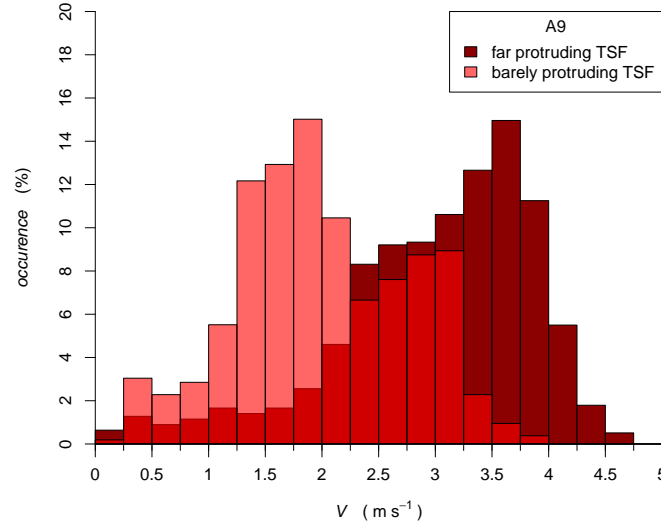


Fig. 14 Histogram of mean wind speed, V , for station A9 on the North shoulder plotted for a far (red) and a barely (pink) protruding thermal submeso front (TSF). Colors are opaque to show the overlapping histograms simultaneously. A TSF is defined as barely protruding if A15 (half way uphill the North shoulder) was within the cold-air layer while a TSF is far protruding if A15 was within the warm-air layer.

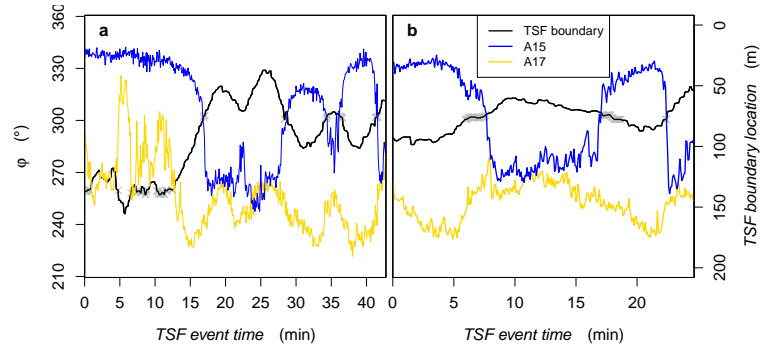


Fig. 15 Time series of wind direction, φ , of both ultrasonic anemometer stations. A thermal submeso front can potentially cause wind directional meandering when it is passing a station frequently. Grey crosses: A15 or A17 within transition area of thermal submeso fronts; black line: location of thermal submeso front.

Eidesstattliche Erklärung

(§ 8 Satz 2 Nr. 3 PromO Fakultät)

Hiermit versichere ich eidesstattlich, dass ich die Arbeit selbstständig verfasst und keine anderen als die von mir angegebenen Quellen und Hilfsmittel benutzt habe (vgl. Art. 64 Abs. 1 Satz 6 BayHSchG).

(§ 8 Satz 2 Nr. 3 PromO Fakultät)

Hiermit erkläre ich, dass ich die Dissertation nicht bereits zur Erlangung eines akademischen Grades eingereicht habe und dass ich nicht bereits diese oder eine gleichartige Doktorprüfung endgültig nicht bestanden habe.

(§ 8 Satz 2 Nr. 4 PromO Fakultät)

Hiermit erkläre ich, dass ich Hilfe von gewerblichen Promotionsberatern bzw. –vermittlern oder ähnlichen Dienstleistern weder bisher in Anspruch genommen habe noch künftig in Anspruch nehmen werde.

(§ 8 Satz 2 Nr. 7 PromO Fakultät)

Hiermit erkläre ich mein Einverständnis, dass die elektronische Fassung der Dissertation unter Wahrung meiner Urheberrechte und des Datenschutzes einer gesonderten Überprüfung unterzogen werden kann.

(§ 8 Satz 2 Nr. 8 PromO Fakultät)

Hiermit erkläre ich mein Einverständnis, dass bei Verdacht wissenschaftlichen Fehlverhaltens Ermittlungen durch universitätsinterne Organe der wissenschaftlichen Selbstkontrolle stattfinden können.

Ort, Datum, Unterschrift:
